POLITECNICO DI TORINO

Master's Degree in Energy and Nuclear Engineering

Master’s Thesis

Development of a LabVIEW-Based ICE Test Bench Automation System to Support Next-Generation Engine Technologies



Supervisor:
Prof. Luciano ROLANDO

Co-Supervisors:
Prof. Andrés SEBASTIÁN HERRERA
Prof. Rubén ABBAS CÁMARA

Candidate:
Vittorio CENTOFANTI

September 2026

Abstract

The need to develop innovative internal combustion engines to reduce fuel consumption and emissions, mitigating environmental impact, makes advanced engine study and experimental evaluation of new technologies essential. In this context, the development and full automation of engine test benches represent a fundamental requirement for conducting reliable energy balance analyses and evaluating core performance indicators.

This thesis work focuses on the automation process of an internal combustion engine test bench to enable performance characterization, engine calibration optimization, and detailed energy balance evaluation. The activity was divided into two main areas: a hardware phase, involving the selection, installation, wiring, and calibration of data acquisition systems and sensors within the test bench; and a software phase developed in the LabVIEW environment, implementing signal acquisition functions, PID loops for engine speed and load control, calculation of thermodynamic and mechanical parameters, and a dedicated dashboard for real-time data visualization.

The proper functioning and capabilities of the measurement and control systems were assessed by testing a spark-ignition engine. During steady-state tests and transient maneuvers between target speeds and load points, the system achieved satisfactory response times and relatively low fluctuations around the setpoints in most test conditions. The acquired data were used to determine the engine full-load torque curve, which shows that the torque output exhibits minimal variation around its peak over a broad speed range. Experimental tests allowed for the mapping of key performance parameters. Specifically, energy balance and efficiency evaluations demonstrated that optimal performance, marked by maximum overall efficiency and minimum BSFC, is achieved around 75% of maximum engine load.

These experimental results provide a reliable basis for future bench upgrades, including the integration of an in-cylinder pressure sensor for indicated cycle analysis, and for the calibration of 1D virtual engine models.

Acknowledgments

I would like to deeply thank my supervisor, Prof. Luciano Rolando, for being an excellent and inspiring teacher and for having been able to transmit to me, during the lectures, the passion and the knowledge he has in the field of engines. I am profoundly grateful to him for giving me the chance to develop my Master's thesis under his guidance and for having supported me throughout the process.

Quiero agradecer enormemente a mis tutores de la Universidad Politécnica de Madrid, Andrés Sebastián y Rubén Abbas, por todo: por la posibilidad que me dieron de vivir una experiencia increíble en Madrid, por su apoyo durante el desarrollo de este trabajo y por haberme hecho sentir como parte de su familia. Por último, pero no por ello menos importante, quiero también agradecer a Pedro por la paciencia y la gran ayuda que me dio en la Celda, así como a todo el personal, profesores, doctorandos y compañeros del Laboratorio de Motores Térmicos por haberme integrado desde el primer momento y por haberme hecho sentir como en casa.

Devo ringraziare la mia famiglia: Mamma e Papà per avermi consentito di studiare e per avermi spronato in tutti questi anni a raggiungere questo obiettivo. Sono loro grato per avermi permesso di vivere tutte le esperienze fatte finora e per avermi supportato in ogni momento. Ringrazio mia sorella Elena per aver sempre creduto nelle mie capacità e mio nonno Tommaso per avermi trasmesso le sue passioni e la sua manualità.

Voglio ringraziare tutti i miei amici più cari per tutte le risate e i momenti spensierati condivisi e per quelli che passeremo insieme, oltre che per avermi aiutato, ognuno a modo suo, ad arrivare fin qui e a diventare la persona che sono. Li considero dei punti fermi e fra i tasselli più importanti della mia vita.

Sono grato per tutte le più care amicizie strette a Torino: mi hanno permesso di vivere questa nuova esperienza fra risate e divertimento e mi hanno aiutato a superare al meglio tutti i timori e gli ostacoli. Anche se sono tra i legami più recenti che ho, li sento come se facessero parte della mia vita da sempre.

Table of contents

Abstract ii

Acknowledgments iii

List of Figures vi

List of Tables ix

1 Introduction 1

1.1 Motivation 1

1.2 Research objectives 3

1.2.1 Primary Functional Goals (System Level) 3

1.2.2 Foundational Engineering Milestones (Execution Level) 4

1.3 Structure of the Manuscript 4

2 Description of the Engine and Test Cell 6

2.1 Test Cell Infrastructure 6

2.2 Engine Specifications 10

2.3 Dynamometer Brake Specifications and Operating Principle 13

2.4 Previous Work 16

3 Test Bench Design 19

3.1 Hardware Architecture and Instrumentation 19

3.1.1 Data Acquisition Modules 19

3.1.2 OBD-II Vehicle Communication Interface 22

3.1.3 Temperature Measurements 23

3.1.4 Air Pressure Measurements 23

3.1.5 High-Pressure Fuel Rail Sensor 25

3.1.6 Throttle Position Sensor Signal 26

3.1.7 Exhaust Gas Pressure Measurement 27

3.1.8 Fuel Flow Measurement 29

3.1.9 Coolant Flow Measurement 30

3.1.10 Air Mass Flow Measurement 32
3.1.11 Grounding Architecture and Star-Point Configuration 34
3.1.12 Engine Cooling System Optimization 35
3.2 Software Environment and Performance Analytics 39
3.2.1 Data Acquisition Architecture and Signal Processing 40
3.2.2 Sensor Calibration and Signal Conversion 48
3.2.3 Test Bench Control 55
3.2.4 Real-Time Data Visualization and Thermodynamic Performance Computation 60
4 Tests and Results 69
4.1 Dynamometer Brake Control Tests 69
4.1.1 Engine Speed Step Response Tests 69
4.1.2 Load Disturbance Rejection Tests 72
4.2 Charge Control Tests 76
4.3 Engine Performance Map 79
4.4 Energy Balance Evaluation 81
4.5 Volumetric Efficiency Analysis 83
4.6 Brake Specific Fuel Consumption (BSFC) and Global Efficiency Analysis 88
5 Conclusion 91
5.1 Summary of Key Findings 91
5.2 Future Work and Test Bench Upgrades 92
6 References 94

List of Figures

Figure 1.1.1-Global CO2 Emissions from Fuel Combustion by Sector with Electricity and Heat Reallocated [1] 1
Figure 1.1.2-CO2 Emissions from Transport, 2015-2024 [2] 2
Figure 2.1.1-Test Cell Main Compartment 8
Figure 2.1.2-DAQ System Rack 9
Figure 2.1.3-Test Bench Control Room 10
Figure 2.2.1-Renault H5Ft Engine 11
Figure 2.2.2-Fuel Injection System 12
Figure 2.2.3-Turbocharging System 13
Figure 2.3.1-Schenck W260 Brake 14
Figure 2.3.2-Magnetic Field Generated within the Dynamometer [5] 15
Figure 2.4.1-VISA Control Loop for the Brake Power Supply 17
Figure 3.1.1-NI cDAQ-9178 Chassis 20
Figure 3.1.2-NI-9205 Module 20
Figure 3.1.3-NI-9263 Module 21
Figure 3.1.4-NI-9213 Module 21
Figure 3.1.5-OBD Software Tool 22
Figure 3.1.6-Bosch Air Pressure Sensor installed on Intercooler Outlet Pipe 24
Figure 3.1.7-Fuel Pressure Sensor 25
Figure 3.1.8-H5Ft OEM Throttle Valve 27
Figure 3.1.9-TC-Direct Pressure Sensor 28
Figure 3.1.10-Bürkert 8071 Flow Meter 29
Figure 3.1.11-Bürkert 8071 Display 29
Figure 3.1.12-Fuel Flow Meter Calibration Procedure 30
Figure 3.1.13-Autosen AS010 Flow Meter 32
Figure 3.1.14-Bosch HFM 5 MAF Sensor 32
Figure 3.1.15-Function Diagram of the HFM 5 Sensor 33
Figure 3.1.16-Danfoss AVTA Thermostatic Valve 37
Figure 3.1.17-Thermostatic Water Control Assembly with Danfoss AVTA Valve and Ball Valve Bypass 38
Figure 3.2.1-Temperature While Cycle 41

Figure 3.2.2-Temperature DAQ Assistant Configuration 41
Figure 3.2.3-Input DAQ Assistant Block 42
Figure 3.2.4-LabVIEW Block Diagram Detail Illustrating the Master Cluster Definition and Signal Aggregation 44
Figure 3.2.5-TDMS Open Block 45
Figure 3.2.6-TDMS Write Block 45
Figure 3.2.7-Elapsed Time Calculation Logic for Test Data Recording 46
Figure 3.2.8-DAQmx Task Loop 47
Figure 3.2.9-Air Pressure Calibration Curves 49
Figure 3.2.10-Fuel Pressure Sensor Calibration Curve 50
Figure 3.2.11-Throttle Valve Position Signal Calibration Curve 50
Figure 3.2.12-Air Mass Flow Meter Calibration Curve 51
Figure 3.2.13-Exhaust Pressure Sensor Calibration Curve 52
Figure 3.2.14-Coolant Flow Meter Calibration Curve 53
Figure 3.2.15-Fuel Flow Meter Fine Calibration 54
Figure 3.2.16-Fuel Flow Meter Calibration Curve 54
Figure 3.2.17-PID Speed Control Loop 57
Figure 3.2.18-PID Charge Control Loop 59
Figure 3.2.19-Safety Implementation in the Test Bench Control System 60
Figure 3.2.20-Main System Overview Tab 61
Figure 3.2.21-Energy Balance Tab 62
Figure 3.2.22-Performance Parameters Tab 63
Figure 3.2.23-Global Data Tab 63
Figure 3.2.24-PID Control Tab 64
Figure 4.1.1-Engine Speed Step Response: Transition from 2600 to 3400 RPM at 20% Throttle (Longest Settling Time) 71
Figure 4.1.2-Engine Speed Step Response: Transition from 2600 to 3400 RPM at 60% Throttle (Shortest Settling Time) 71
Figure 4.1.3-Engine Speed Step Responses at 40% Throttle: Acceleration from 1800 to 2600 RPM (Left) and Deceleration from 3400 to 2600 RPM (Right) 72
Figure 4.1.4-Load Disturbance Response: Throttle Step from 20% to 40% at 1800 RPM (Longest Settling Time) 74
Figure 4.1.5-Load Disturbance Response: Throttle Step from 40% to 60% at 3400 RPM (Fastest Settling Time) 74

Figure 4.1.6-Load Disturbance Response: Throttle Step from 40% to 60% at 1800 RPM Exhibiting Dual-Peak Transient Behavior 75
Figure 4.1.7-Load Disturbance Response: Throttle Step from 40% to 60% at 2600 RPM Showing Convergence Oscillations 76
Figure 4.2.1-Charge Control Transient Responses: Target Torque Step Tracking at 1500 RPM 77
Figure 4.2.2-Charge Control Transient Responses: Target Torque Step Tracking at 2500 RPM 78
Figure 4.2.3-Charge Control Transient Responses: Target Torque Step Tracking at 3500 RPM 78
Figure 4.3.1-Full Load Engine Performance Map (Torque vs. Engine Speed) 80
Figure 4.3.2-Full Load Engine Power Profile 81
Figure 4.4.1-Experimental Engine Energy Balance across varying speeds and loads 82
Figure 4.5.1-Pre-throttle Volumetric Efficiency 84
Figure 4.5.2-Manifold Volumetric Efficiency 86
Figure 4.6.1-Experimental BSFC Map correlating Specific Fuel Consumption with Engine Speed and Torque 88
Figure 4.6.2-Experimental Global Efficiency Map correlating Engine Efficiency with Engine Speed and Torque 89

List of Tables

Table 2.1-Engine Specifications [4] 13
Table 2.2-Brake Specifications 16
Table 4.1-Measured Settling Times across Dynamic Engine Speed Transitions at Various Throttle Positions 70
Table 4.2-Measured Settling Times for Throttle Step Changes 73

1 Introduction

1.1 Motivation

The automotive landscape is currently undergoing a profound technological shift, driven by increasingly stringent global emission regulations and the urgent need to mitigate the environmental impact of transportation. According to empirical data from global energy and emissions tracking (IEA Greenhouse Gas Emissions), the transportation sector alone accounted for approximately 8.81 billion metric tons of CO2 in 2024 (Figure 1.1.1). This staggering volume represents roughly a quarter of direct global emissions from fuel combustion, making transportation one of the single largest drivers of anthropogenic climate impact worldwide [1].

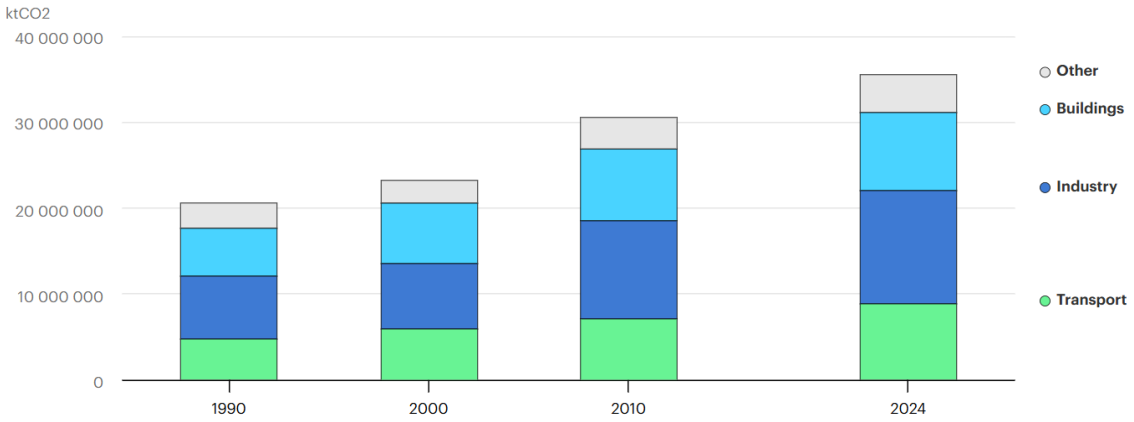


Figure 1.1.1-Global CO2 Emissions from Fuel Combustion by Sector with Electricity and Heat Reallocated [1]

As shown in Figure 1.1.2, within this macro-sector, road transport is by far the most dominant contributor; recent historical data highlight that road vehicles alone are responsible for over 6 Gt of the sector's total CO2 emissions [2]. As global energy demand continues its upward trajectory, fueled by demographic growth and industrial expansion, the mandate to drastically contain both fossil fuel consumption and carbon output has become a critical global priority.

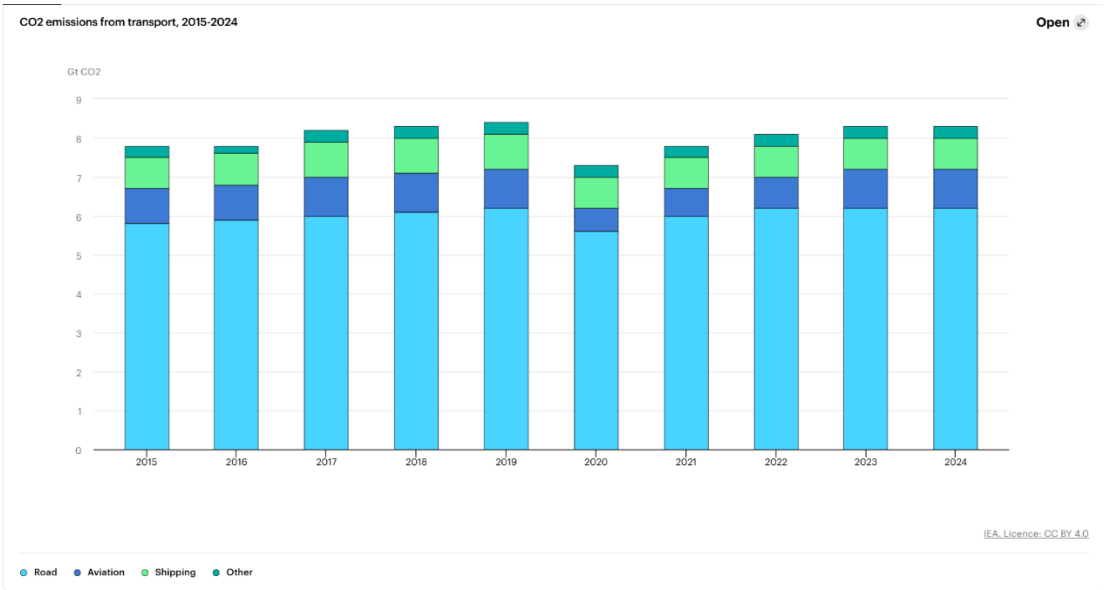


Figure 1.1.2-CO2 Emissions from Transport, 2015-2024 [2]

In response to this environmental imperative, regulatory bodies worldwide have enacted rigorous legislative frameworks. In the European Union, the evolution of emission standards, culminating in the highly restrictive Euro 7 framework, represents a paradigm shift. These standards not only impose drastic reductions in fleet-wide greenhouse gas emissions to align with climate neutrality goals, but they also enforce exceptionally tight thresholds for criteria pollutants such as nitrogen oxides (NOx), unburned hydrocarbons (HC), and particulate matter (PM). Furthermore, modern regulations require powertrain compliance under broad and unpredictable Real Driving Emissions (RDE) conditions, pushing engineering boundaries further than ever before [3].

Within this context, the continued study, optimization, and development of innovative internal combustion engines (ICEs) remain crucial. Even amid the ongoing transition toward electrification, highly optimized ICEs are destined to play a pivotal role for decades to come, particularly as the core components of advanced hybrid architectures and within sectors where full electrification remains technologically or economically unfeasible.

Beyond pure industrial research, engine test cells located within academic institutions serve multiple vital roles. They are foundational for educational and teaching purposes, providing future engineers with invaluable hands-on experience in dealing with real-world mechanical and control complexities. Specifically, the Thermal Engines Laboratory at the Universidad Politécnica de Madrid hosts regular practical sessions for engineering students throughout the academic year. Having a fully operational and modern test bench is essential for these teaching activities, as it allows students to transition from theoretical classroom lectures to active experimentation, live data acquisition, and real-time engine management.

Furthermore, a modernized testing facility acts as a catalyst for research and institutional collaborations, bridging the gap between academic studies and applied industrial engineering. The university frequently partners with external automotive companies, OEMs, and technology suppliers for joint research projects. An advanced, automated test cell not only attracts these high-value industrial partnerships but also provides a highly reliable platform to validate prototype components and develop advanced engine calibration strategies directly alongside industry stakeholders.

1.2 Research objectives

This thesis focuses on upgrading a raw mechanical testing cell into a fully functional, highly precise research and development (R&D) platform, then using it to conduct a comprehensive study and performance characterization of a 1.2 Renault H5Ft engine.

To fulfill this aim, a two-level development strategy was adopted, establishing primary functional goals alongside foundational execution tasks.

1.2.1 Primary Functional Goals (System Level)

The overarching ambition of this work focuses on the final capabilities of the R&D platform and the subsequent analysis of the engine:

- Test Bench Automation: Transforming a manually operated setup into an autonomous closed-loop facility capable of managing both steady-state operating points and dynamic load transients.
- Critical Evaluation of Instrumentation Limits: Validating the experimental data by identifying the test bench's measurement thresholds, specifically isolating sensor artifacts and recording inaccuracies that arise during tests.
- Powertrain Characterization and Boundary Identification: Mapping the engine's performance in terms of torque and power delivery across the speed range, while explicitly identifying its physical and thermal operational limits.
- Thermodynamic Assessment: Conducting an in-depth energy balance and a thorough evaluation of the engine's core performance indicators, including Brake Mean Effective Pressure (BMEP), volumetric and overall efficiencies, and Brake Specific Fuel Consumption (BSFC).

1.2.2 Foundational Engineering Milestones (Execution Level)

Achieving the primary goals was directly predicated on executing several preparatory technical and methodological tasks:

- Hardware and Sensor Integration: The physical installation and calibration of a dedicated sensor network and DAQ systems to accurately monitor pressures, temperatures, and mass flows.
- Dual-Loop Control Architecture: The development and tuning of the control logic orchestrating the eddy-current dynamometer brake (for speed regulation) and the virtual accelerator (for charge control).
- Data Recording and Processing Framework: Establishing a robust architecture for the continuous recording and storage of test data. This unified framework ties the hardware and control layers together, enabling real-time signal conditioning and the continuous calculation of fundamental powertrain metrics (fluid dynamic breathing, thermodynamic efficiencies, and energy distribution).

1.3 Structure of the Manuscript

This manuscript is organized to provide a clear and logical progression of the work carried out to upgrade, automate, and evaluate the engine test bench.

The following chapter provides a comprehensive overview of the experimental facility. It introduces the test cell layout and outlines the technical specifications of both the installed engine and the dynamometer. It concludes with a critical analysis of the previous work, which provided the foundation for the current project.

Chapter 3 represents the core of the research, exhaustively describing the test bench design and its improvements. The first part focuses on the hardware architecture, detailing the selection and installation of data acquisition modules and sensors, alongside physical enhancements to the cell. The second part covers software development. It explains the signal acquisition and calibration processes, the data logging system, and the implementation of PID control loops for regulating engine speed and load. The third part illustrates the design of the LabVIEW graphical user interface and the real-time computation of key engine performance parameters.

Chapter 4 presents and discusses the experimental test results. It first evaluates the effectiveness and stability of the newly implemented brake and load control systems. Subsequently, it provides an analysis of the engine performance maps, followed by an in-depth

evaluation of the energy balance, volumetric efficiency, and BSFC across different operating conditions.

Finally, Chapter 5 summarizes the primary conclusions derived from this project, assesses the achieved milestones, and proposes future recommendations for further development of the test bench.

2 Description of the Engine and Test Cell

This chapter provides a comprehensive and detailed overview of the experimental test bench layout, alongside the technical specifications of the engine under investigation. The following sections initially characterize the physical architecture of the laboratory environment, highlighting the functional separation between the control room and the main test cell. Subsequently, the document provides an in-depth presentation of the technical specifications of the Renault H5Ft spark-ignition internal combustion engine, which serves as the primary device under test. Finally, the chapter addresses the working principles and operational integration of the Schenck W 260 eddy current dynamometer, emphasizing its role in absorbing mechanical power and applying precise and controlled loads throughout the experimental testing phases.

2.1 Test Cell Infrastructure

The development of this thesis project was carried out in the “Laboratorio de Motores Térmicos” (Thermal Engines Laboratory) of the Escuela Técnica Superior de Ingenieros Industriales (ETSII) at the Universidad Politécnica de Madrid (UPM). This laboratory includes different rooms dedicated to a multitude of experimental studies, tests, and processes. The specific infrastructure utilized for this research is designated as "Celda 3" (Test Cell 3). To protect operators from noise, high temperatures, and mechanical hazards, Celda 3 is physically subdivided into two distinct compartments sealed from each other and accessible directly from the main laboratory hallway: the control room and the main test cell. A double-glazed observation window set into the dividing acoustic wall provides visual monitoring during engine operation. Electrical connection and signal transfer between the control room and the test cell are achieved exclusively through a dedicated cable transit port built into the wall. To ensure signal integrity and maintain a highly organized layout, all electrical wires and data cables routed through this transit port are grouped by function and enclosed in protective sheaths, supported by a dedicated cable tray structure.

The Test Cell (Main Compartment): This sealed compartment, illustrated in Figure 2.1.1, hosts the internal combustion engine together with all the electrical apparatus that power it, including the engine control computer (ECU), the electrical low-pressure fuel pump, and the 12 V battery. Moreover, the room houses the dynamometer engine brake and all the heavy

mechanical equipment supporting the bench. The physical and mechanical infrastructure of the cell is detailed as follows:

- Support Structure and Alignment: The engine and brake are mounted on a highly stable, solid base specifically engineered to absorb the forces and vibrations generated during engine operation. This structure incorporates adjustable mechanisms to guarantee the precise mechanical alignment of the engine and the dynamometer through the transmission shaft.
- Ventilation and Exhaust Systems: To ensure optimal combustion efficiency, the room employs a simultaneous air impulse and extraction system located on opposite sides of the cell, which constantly renews the air volume and aids in ambient cooling. Engine exhaust gases are routed safely outside the building through a system equipped with a catalytic converter and a muffler.
- Thermal Management: The dynamometer is directly cooled by the facility's water supply. Furthermore, because the engine's standard automotive radiator was removed, its internal coolant circuit is routed through a relatively large liquid-to-liquid heat exchanger measuring approximately 1.7 meters in height and 10 cm in diameter. This allows the engine to be cooled by the same facility water without the two liquids mixing. Additionally, a dedicated fan is mounted to the turbocharger's air-to-air intercooler to replicate the convective airflow a moving vehicle would naturally experience.



Figure 2.1.1-Test Cell Main Compartment

The Control Room: The control room serves as the centralized management hub for the test bench, enabling safe operation, real-time control, and data monitoring. It houses the host workstation (PC) running the supervisory software, alongside a dedicated instrumentation rack containing the data acquisition (DAQ) chassis (illustrated in Figure 2.1.2) and the signal conditioning boards. From this rack, all command, sensor, and power cables are routed directly toward the test cell.

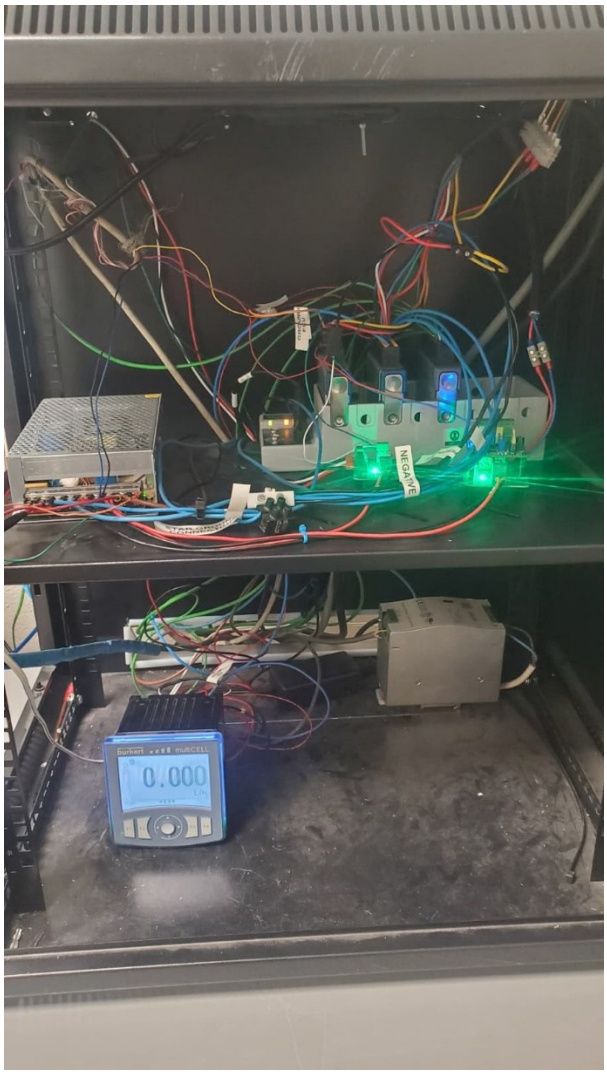


Figure 2.1.2-DAQ System Rack

Another primary component of this room is the custom Control Panel, which safely redirects the 230 V, 50 Hz AC mains power to several dedicated DC power supplies that provide the 12 V required by the electronic systems. The Control Panel, shown in the right corner of the desk in Figure 2.1.3, features several specific physical switches to operate the bench:

- GENERAL Switch: Activates the primary power supply dedicated to the data acquisition systems.
- BATERÍA (Battery) Switch: A mushroom-style emergency button that connects the 12 V battery, fulfilling the same role as turning a key to the ignition contact position in a conventional vehicle.
- BOMBA DE GASOLINA (Fuel Pump) Switch: Powers the low-pressure fuel delivery pump.
- INTERCOOLER Switch: Activates the intercooler's forced-air fan.

- ARRANQUE (Start) Button: A pushbutton that is used to crank the engine. Once started, the engine's original Electronic Control Unit (ECU) autonomously maintains the idle speed.
- PARE (Stop) Button: An emergency stop push button utilized to shut down the engine.

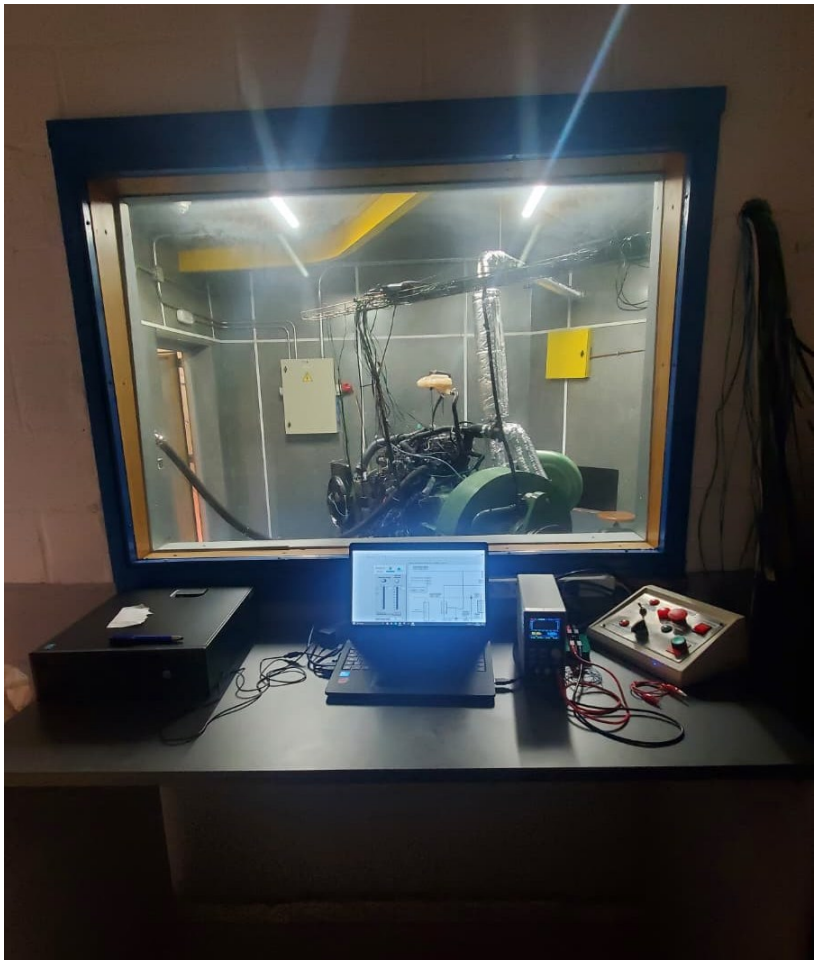


Figure 2.1.3-Test Bench Control Room

2.2 Engine Specifications

The engine under study, installed within the test cell, is a Renault H5Ft internal combustion engine. Originally manufactured for the Renault-Nissan-Mitsubishi alliance, this specific unit was utilized in a fourth-generation Renault Clio. It is a four-stroke, spark-ignition gasoline engine operating on the theoretical Otto cycle.



Figure 2.2.1-Renault H5Ft Engine

Engine Architecture and Valvetrain: The H5Ft features an inline four-cylinder configuration with a total volumetric displacement of 1197 cm^3. To reduce overall weight and improve thermal dissipation, both the engine block and cylinder head are made entirely of aluminum. The gas exchange process is governed by a Dual Overhead Camshaft (DOHC) valvetrain driven by a robust timing chain, actuating four valves per cylinder. The engine's internal geometry comprises a 72.2 mm cylinder bore and a 73.1 mm piston stroke, resulting in a static compression ratio of 10:1 [4].

Direct Injection System: A distinguishing feature of this powertrain is its electronic direct fuel injection system (Figure 2.2.2). Unlike traditional indirect injection architectures where the air-fuel mixture is prepared in the intake manifold, the H5Ft injects gasoline directly into the combustion chamber. This advanced fueling strategy allows the Electronic Control Unit (ECU) to precisely control the injected fuel mass, optimizing combustion efficiency, improving transient response, and reducing overall fuel consumption.

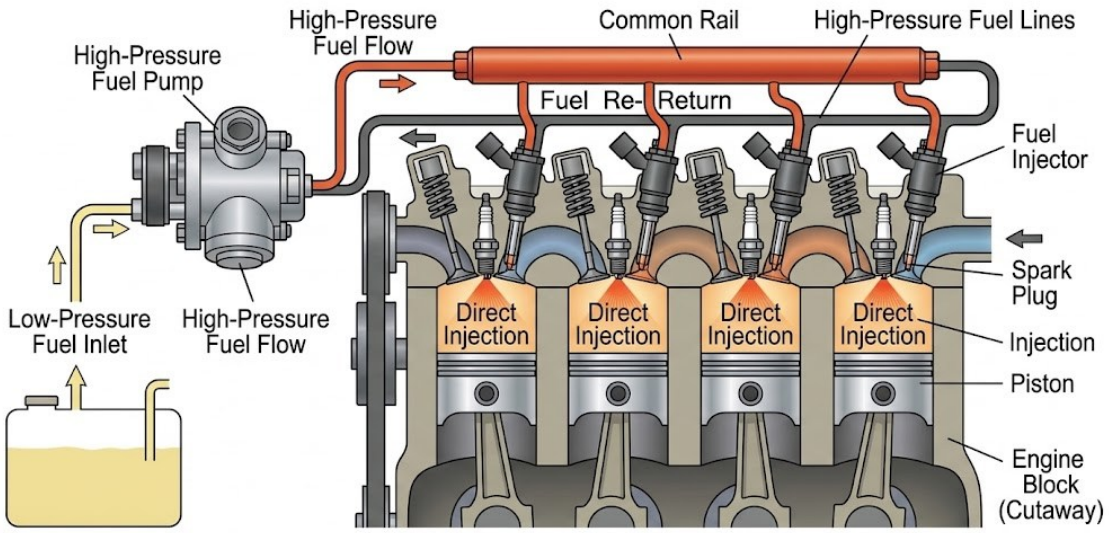


Figure 2.2.2-Fuel Injection System

Turbocharging and Intercooling: Air induction is managed by a forced induction system utilizing an exhaust-driven turbocharger Figure 2.2.3). The turbocharger recovers kinetic and thermal energy from the exhaust gas stream to drive a centrifugal compressor, which significantly increases intake-air pressure. This forced induction maximizes the oxygen mass trapped in the cylinders during the intake stroke, allowing for a proportionally larger mass of fuel to be combusted, which dramatically increases the engine's specific power output. However, the fluid-dynamic compression of the intake air inevitably raises its temperature, a phenomenon that negatively impacts air density and increases the risk of abnormal combustion events such as engine knocking (detonation). To mitigate these effects and prevent thermal damage to internal components, the compressed air charge is routed through an air-to-air heat exchanger, commonly known as an intercooler, before entering the intake manifold. The intercooler dissipates the excess heat, maximizing charge density and ensuring optimal thermodynamic efficiency during the expansion stroke.

Engine specifications are summarized in Table 2.1.

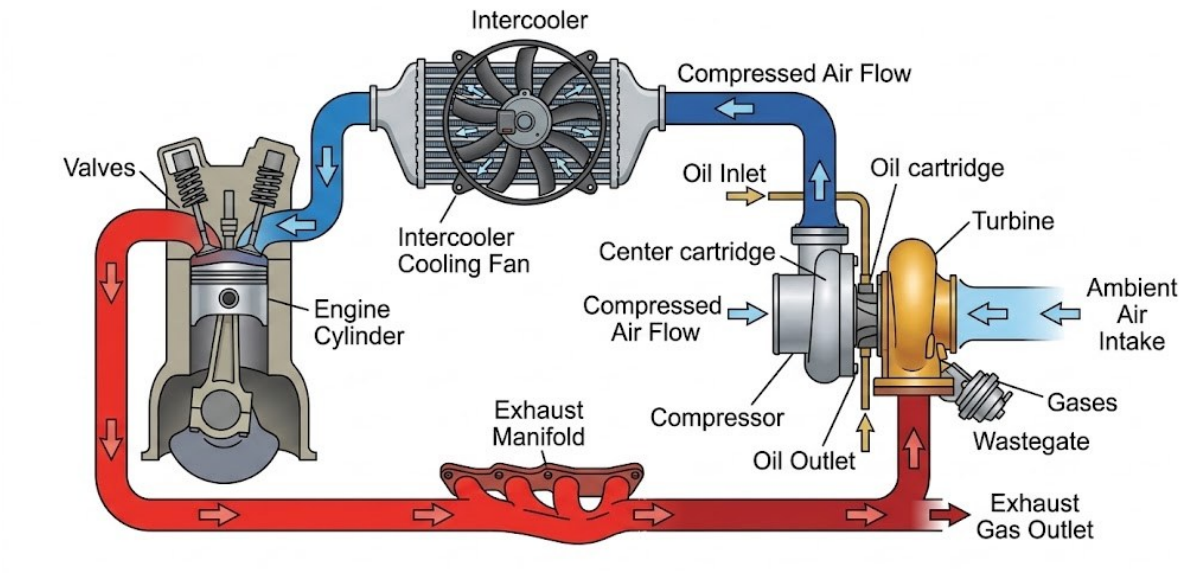


Figure 2.2.3-Turbocharging System

Parameter:	**Specification:**
Engine Model	Renault H5Ft
Fuel Type	Gasoline
Engine Layout	Inline 4-cylinder
Displacement	1197 cm³
Bore x Stroke	72.2 mm x 73.1 mm
Compression Ratio	10:1
Valvetrain Architecture	Dual Overhead Camshaft (DOHC), 4 valves per cylinder
Timing Mechanism	Timing Chain
Fuel Delivery System	Electronic Direct Injection
Aspiration	Turbocharger with Intercooler
Maximum Power	88 kW (120 hp) @ 4900 rpm
Maximum Torque	190 N·m @ 2000 rpm

Table 2.1-Engine Specifications [4]

2.3 Dynamometer Brake Specifications and Operating Principle

To apply a precise and controllable mechanical load to the internal combustion engine, the test bench is equipped with a Schenck W 260 eddy current dynamometer brake (Figure 2.3.1). This specific testing equipment relies on electromagnetic induction to generate frictionless braking torque.



Figure 2.3.1-Schenck W260 Brake

The fundamental operation of the dynamometer is governed by Faraday's and Lenz's laws of electromagnetism. Under these principles, when a moving magnetic field intersects a conductor, or a moving conductor intersects a magnetic field, electrical currents are induced (known as eddy currents or Foucault currents) [5]. These currents generate a secondary magnetic field that opposes the original motion.

The internal structure of the Schenck W 260 consists of two primary components:

- **The Stator:** The stationary component contains electromagnetic coils. When a controlled direct current (DC) flows through these coils, they act as an electromagnet, generating a magnetomotive force (m.m.f). This primary magnetic field is proportional to the current and the number of turns in the solenoid, as defined by Equation 2.1 [5].

$$m.m.f = I \cdot N \tag{2.1}$$

Where "N" is the number of turns and "I" is the amount of current flowing through the coil. The braking force is directly controlled by regulating this current.

- **The Rotor:** Driven by the engine's output shaft, the rotor is designed as a star-shaped polar wheel. The axial surfaces of this star-shaped rotor face the inner rings of the stator's internal cooling chambers, separated only by a narrow air gap. The magnitude of the magnetic flux density B across this gap is a vector quantity given by Equation 2.2 [5].

$$B = \frac{\Phi}{A} \tag{2.2}$$

Where "Φ" is the magnetic flux and "A" is the area. Because of the rotor's star shape, the flux lines are squashed into a smaller area at the pole tips, creating high local magnetic flux density as illustrated in Figure 2.3.2.

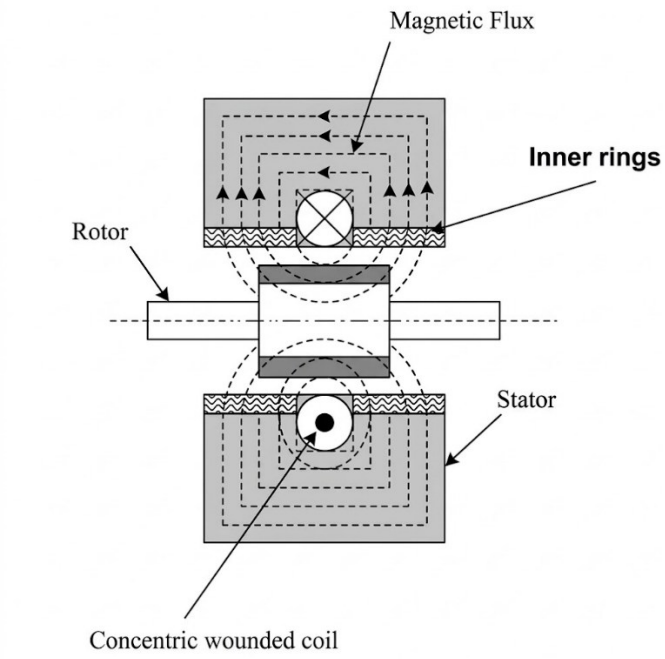


Figure 2.3.2-Magnetic Field Generated within the Dynamometer [5]

As the engine spins the rotor, the stator's inner rings are subjected to a varying magnetic field caused by the passage of the rotor's pole tips. According to Faraday's law, this relative motion induces an electromotive force (emf) proportional to the rate of change of the magnetic flux:

$$emf = -N\frac{\Delta\Phi}{\Delta t} \tag{2.3}$$

Where "$\frac{\Delta\Phi}{\Delta t}$" is the change in flux with respect to time, and the negative sign reflects Lenz's law, indicating that the induced current opposes the change in the magnetic field. Due to the resistive nature of the stator metal, these electromotive forces generate strong eddy currents. The magnetic fields created by these eddy currents attempt to cancel the original magnetic

field, creating a counter-restraining force that effectively absorbs the engine's mechanical power [5].

The mechanical energy absorbed by the dynamometer is entirely transformed into thermal energy due to the Joule effect. A significant design advantage of this architecture is that the eddy currents (and consequently the heat) are generated within the stationary stator rather than the moving rotor. This allows the heat to be efficiently evacuated by a direct, continuous flow of facility water through the internal cooling chambers of the stator.

The electromagnetic braking action naturally creates a reaction force that attempts to drag the outer housing of the brake in the same rotational direction as the engine shaft. To accurately measure the applied load, the dynamometer's housing is cradle-mounted (allowing it to swivel) and is linked to a dynamometric load cell via a lever arm with a strictly defined length of 0.6 meters. By measuring the restraining force at this known distance, the data acquisition system can precisely calculate the real-time braking torque.

The operational limits of the Schenck W 260 dynamometer are summarized in Table 2.2.

Parameter:	**Specification:**
Brake Model	Schenck W 260
Braking Principle	Eddy Current (Foucault)
Cooling System	Direct Water Cooling
Torque Measurement Lever Arm	0.6 m
Maximum Rotational Speed	7500 rpm
Maximum Torque Capacity	700 N·m
Maximum Power Absorption	220 kW (295 hp)

Table 2.2-Brake Specifications

2.4 Previous Work

The preliminary development of the test bench, carried out by Alberto Navas García as part of his bachelor's thesis [6], focused on establishing manual control of the actuators and conditioning the primary measurement signals. This earlier work, which provided the foundation for the current project, focused on both physically acquiring engine speed and torque and manually controlling accelerator demand and braking excitation.

- **Manual Throttle Control:** The physical accelerator pedal was removed and replaced by software-generated commands generated via a National Instruments NI-9263 analog output module. To mimic the vehicle's dual-potentiometer pedal sensor and prevent the engine control unit (ECU) from entering a “safety mode”, two linear

voltage signals (0–5 V and 0–2.5 V) preserving an exact 2:1 ratio were synthesized and fed directly to the engine management system.

- **Manual Dynamometer Control:** Brake regulation was achieved using a programmable "Owon SPE6103" DC power supply connected to the host computer via USB. The braking torque generated by the dynamometer is governed by the excitation current circulating through its stator coils. Because the brake exhibits a predictable electrical impedance, drawing approximately 1 A for every 10 V applied, full braking demand across the 0 to 50 V range corresponds to an operating current of 0 to 5 A. Under these conditions, the Owon SPE6103 programmable power supply provides an ideal match for the system, as its rating of up to 60 V and 10 A (with a 300 W total power envelope) fully covers the 50 V and 5 A maximum excitation requirements without risking hardware saturation. Consequently, commanding the power supply output voltage allows simple and effective regulation of the excitation current through the coils. LabVIEW's VISA architecture, shown in Figure 2.4.1, handles communication by initializing the serial port at 115200 baud with a line-feed termination character. Within the software control loop, the user-defined numerical voltage is formatted into a standard SCPI string command (e.g., VOLT X). To optimize data transmission and prevent serial port saturation, a conditional case structure ensures the write function executes only when the operator actively alters the voltage setpoint. Finally, to protect the power unit against reverse currents and inductive back-EMF spikes from the brake windings, an intermediate protection circuit (PSB Bridge) with a series diode and a flyback freewheeling diode was placed between the power supply and the dynamometer.

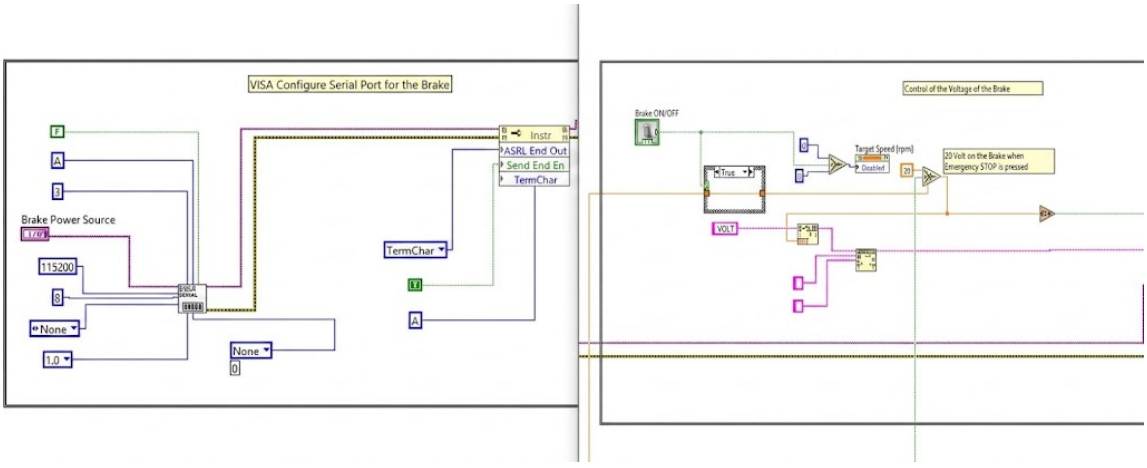


Figure 2.4.1-VISA Control Loop for the Brake Power Supply

- **Engine Speed Acquisition:** Rotational speed was retrieved from the engine's onboard 60-tooth inductive sensor, whose square-wave frequency directly corresponds to engine RPM. To adapt this frequency into a readable 0–10 V signal for the acquisition card, a frequency-to-voltage converter was implemented. A dedicated voltage-follower circuit using an operational amplifier with high input impedance was added to prevent current drain from attenuating the sensor waveform, eliminating spurious error codes within the ECU.
- **Torque Acquisition:** The braking torque was sensed using an “Epelsa TSF” load cell positioned at a 0.6 m lever arm, which produces a minute differential millivolt-level signal proportional to the compressive reaction force. An instrumentation amplifier circuit based on the AD8422 was developed to amplify this differential output into the 0–10 V range readable by the DAQ board while ensuring minimal signal distortion.

3 Test Bench Design

A full experimental characterization of the internal combustion engine requires precise physical monitoring across multiple measurement stations distributed along the test bench. To achieve this, the testing infrastructure was developed through a coordinated integration of dedicated physical instrumentation and real-time computational routines.

This chapter outlines the complete test bench design by detailing both its hardware and software implementations. First, the physical architecture is described, focusing on sensor integration, signal conditioning strategies, and diagnostic communication via the OBD-II interface. Subsequently, the software architecture implemented in LabVIEW is presented, detailing the data acquisition and recording loops, real-time thermodynamic and energy balance calculations, and the supervisory control logic governing bench operations.

3.1 Hardware Architecture and Instrumentation

To fully characterize the H5Ft engine, a multitude of sensors were distributed across different measurement stations along the test bench. The physical architecture detailed in this section comprises the sensing instrumentation, signal conditioning circuitry, electrical grounding network, and diagnostic communication hardware. Together, these subsystems enable the acquisition of raw electrical signals and their conditioning for subsequent conversion into physical engineering units. The following subsections detail the selection, integration, and wiring of each component.

3.1.1 Data Acquisition Modules

To link the physical sensors of the test bench with the LabVIEW software environment, a robust, high-speed Data Acquisition (DAQ) architecture was implemented using National Instruments (NI) Compact DAQ hardware. The system was designed to ensure high resolution, modular expandability, and low-latency I/O for real-time control loops.

NI cDAQ-9178 Chassis

The acquisition system's backbone is the NI cDAQ-9178, an 8-slot USB chassis. This chassis, shown in Figure 3.1.1, was selected for its plug-and-play USB connectivity and its capacity to house multiple hot-swappable C-Series modules. Specifically, the cDAQ-9178 supports multiple hardware timing engines, allowing the system to run different acquisition loops at distinct sampling rates simultaneously; for instance, running thermocouple polling

at a lower frequency while acquiring at high speed for the PID controllers without timing conflicts.



Figure 3.1.1-NI cDAQ-9178 Chassis

Analog Inputs: The Upgrade from NI-9201 to NI-9205

The test bench requires continuous monitoring of various analog voltage signals (typically $0-5$ V or $0-10$ V).

Initially, the system relied on a standard 8-channel analog input module, the NI-9201, which the previous thesis student integrated only to handle the engine speed and torque signals. However, as the bench grew more complex and the sensor count increased to support more comprehensive thermodynamic analysis, the 8-channel limit became a severe bottleneck. To resolve this, the hardware was upgraded to the NI-9205 module shown in Figure 3.1.2. This unit provides 32 single-ended (or 16 differential) analog input channels with a maximum sampling rate of 250 kS/s. This significant upgrade not only accommodated all current fluid-dynamic and mechanical sensors but also guaranteed ample I/O headroom for future instrumentation.



Figure 3.1.2-NI-9205 Module

Analog Outputs and System Actuation: NI-9263

To control the test bench, the software must send continuous analog command signals to the Engine Control Unit (ECU). This task is handled by the NI-9263, a 4-channel, 16-bit analog output module capable of generating precise ±10 V signals (Figure 3.1.3).



Figure 3.1.3-NI-9263 Module

As detailed in the previous chapter regarding the initial state of the bench, the eddy current dynamometer brake is controlled via a dedicated Owon programmable power supply implemented during the previous thesis work. Consequently, the NI-9263 analog output module is utilized within the LabVIEW architecture exclusively to deliver high-resolution control signals to the ECU to simulate the accelerator pedal voltage inputs.

Thermal Monitoring: NI-9213

Given the extensive thermal mapping required across the engine, the NI-9213 unit (Figure 3.1.4) was selected specifically for temperature measurements. This high-density, 16-channel thermocouple module features 24-bit resolution. The primary motivation for choosing the NI-9213 is its built-in Cold-Junction Compensation (CJC) and integrated signal conditioning, which natively converts microvolt thermocouple signals into accurate, calibrated temperature readings without external amplification circuits.



Figure 3.1.4-NI-9213 Module

3.1.2 OBD-II Vehicle Communication Interface

To access the internal operating parameters computed by the Engine Control Unit (ECU), a commercial multi-brand Vehicle Communication Interface (VCI) was integrated into the test bench setup. This hardware module acts as a digital bridge between the automotive onboard network and the external laboratory workstation.

The VCI connects physically to the ECU network via a standard 16-pin OBD-II diagnostic connector. Internally, the hardware features a microcontroller coupled with a multiplexer relay board, allowing it to automatically route and translate various automotive communication protocols. For the specific application on the Renault H5Ft engine, the interface communicates with the ECU over the high-speed CAN bus network.

To ensure continuous and reliable data transmission, the VCI is connected to the main data acquisition PC via a wired USB connection, avoiding potential latency or signal drops associated with wireless Bluetooth links.

From a functional point of view, the interface operates in combination with a dedicated PC diagnostic suite illustrated in Figure 3.1.5. By transmitting standardized diagnostic requests across the CAN bus, the tool polls the ECU for real-time digitized variables. These decoded data streams provided the reference baseline needed to construct the voltage-to-engineering-unit transfer functions subsequently embedded in the LabVIEW DAQ Assistant Block.

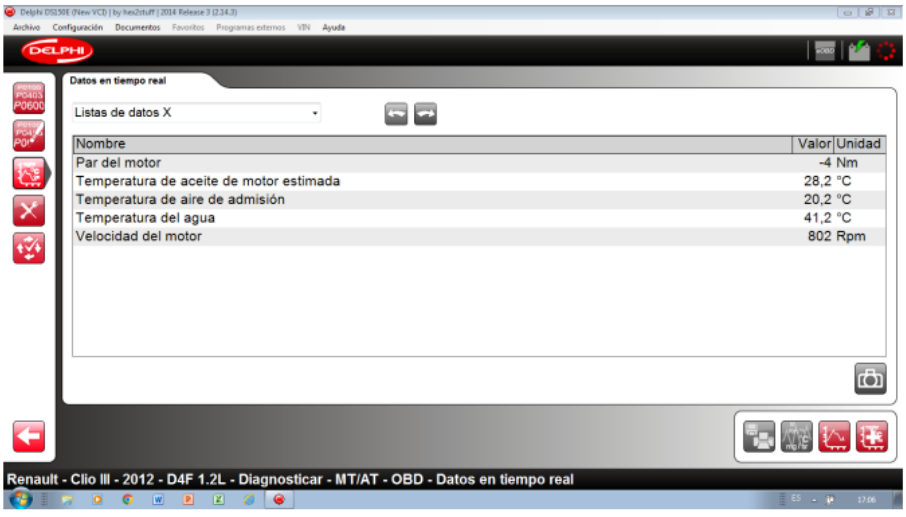


Figure 3.1.5-OBD Software Tool

3.1.3 Temperature Measurements

For the measurement of the temperatures, 9 type K thermocouples were installed; the motivation behind the use of these devices relies on their standardization and their simple integration with National Instruments and the LabVIEW environment.

A thermocouple is constituted by two wires made out of two different metals and jointed together at the point where the measurement has to be taken (hot joint): the difference in electronegativity between the two metals will generate a potential difference at the other extremities of the wires (cold joint) [7], which are connected to the NI-9213 DAQ board. The DAQ board directly measures this voltage, depending on the temperature reached at the hot joint, and converts it into the actual temperature value.

The multitude of types of thermocouples differs mainly in their constituent materials, which will affect their maximum temperature at the hot joint. Type K thermocouples are made out of Chromel (Ni-Cr) for the positive wire and Alumel (Ni-Al) for the negative one and the maximum reading temperature is 1260 °C [7], which is enough for every kind of measurement needed for this study.

The nine thermocouples are distributed across the test bench as follows:

- Two measuring the coolant temperature: one at the engine outlet, and the other at the engine inlet, immediately upstream of the thermostatic valve.
- Three monitoring the intake air temperature at crucial points: at the main air intake (specifically at the MAF sensor inlet), at the compressor outlet, and at the intercooler outlet.
- Three measuring the exhaust gas temperatures: one directly at the exhaust manifold, one at the turbine outlet, and the last one at the catalytic converter outlet.
- One installed along the oil dipstick tube to monitor the engine oil temperature.

3.1.4 Air Pressure Measurements

The signals from the original engine sensors were intercepted to measure the values of pressure at the compressor outlet pipe and at the intake manifold (downstream of the throttle valve). These devices are normally installed on the engine to communicate the parameters to the ECU; they are constituted by:

- A thin and flexible silicon membrane which lies on a small sealed chamber evacuated to an absolute vacuum, which serves as a benchmark for the measurement.
- Four piezo resistors which are embedded directly onto the surface of the silicon membrane and connected to each other in a Wheatstone bridge configuration.

- An integrated electronic component that amplifies the electrical signal before transmitting it to the Engine Control Unit (ECU) [8].

Engine airflow enters the sensor nozzle and exerts pressure on the silicon membrane. The pressure differential between the engine air and the vacuum of the reference chamber causes the membrane to bend; this deflection causes the four overlying piezo resistors to change their electrical resistance. Consequently, the current flow within the integrated circuit, supplied by a constant reference voltage from the ECU, changes. Finally, the internal electronics convert this variation into a linear voltage signal proportional to the detected pressure.

The considered sensors, shown in Figure 3.1.6, are manufactured by Bosch and have three electrical connections: the first one gives the voltage signal in the range between 0,5–4,5 volt with respect to ECU ground, the second one provides the 5 volt power supply for the electronics of the sensor, and the last one is directly connected to ground to give the reference to the device. The measured pressure is directly proportional to the potential difference between the first and third connector. To capture the voltage signal, a dedicated wire was routed from the sensor's signal terminal (Pin 1) directly to the analog input channel of the NI-9205 module. Regarding the negative reference, the circuit relies on the single common ground cable connecting the ECU ground directly to the “COM” port of the NI-9205 board.



Figure 3.1.6-Bosch Air Pressure Sensor installed on Intercooler Outlet Pipe

3.1.5 High-Pressure Fuel Rail Sensor

The OEM high-pressure fuel sensor (Figure 3.1.7, Renault Part No. 166392053R, manufactured by Continental for the H5Ft engine) monitors fuel pressure within the direct-injection rail. This component is a piezoresistive pressure transducer threaded directly into the fuel rail, providing continuous, real-time feedback to the engine management system.



Figure 3.1.7-Fuel Pressure Sensor

Like the air pressure sensors described in the previous paragraph, this sensor operates on the piezoresistive effect. High-pressure fuel enters the sensor tip and exerts force on an internal flexible metallic diaphragm. Microscopic strain gauges bonded to this diaphragm deform in response to the applied pressure, causing a proportional change in their electrical resistance. An internal specific integrated circuit conditions this micro-signal, amplifying and converting it into a standardized analog output.

The transducer features a standard 3-pin connector:

- Power Supply (5 V): Receives a regulated 5 V reference voltage.
- Ground: Connected to the common sensor ground network.
- Signal Output: Delivers a linear analog voltage ranging from 0 to 5 V, strictly proportional to the absolute fuel pressure inside the rail.

To actively monitor the fuel injection system during testing, the 0–5 V analog signal generated by the fuel rail pressure sensor was acquired through pin 3 using the NI-9205 analog input module.

3.1.6 Throttle Position Sensor Signal

Airflow regulation for the H5Ft engine is managed by the OEM Electronic Throttle Body (Renault Part No. 161204451R). This "Drive-by-Wire" unit, shown in Figure 3.1.8, eliminates any mechanical linkage between the accelerator and the butterfly valve, relying entirely on an internal DC motor and a redundant Throttle Position Sensor (TPS) to ensure precise and safe load control.

To integrate the throttle body into the test bench architecture while maintaining the original engine management safety logic, the 6-pin electrical connector was mapped as follows:

- **Position Sensing Circuit (TPS):** For safety and diagnostic purposes, the internal position sensor features a dual-potentiometer configuration. The mechanism relies on two independent resistive tracks with mechanical wipers directly linked to the throttle valve's rotational shaft. As the butterfly valve opens, the first potentiometer wiper slides closer to the 5 V reference terminal, generating a proportionally increasing voltage. Conversely, the wiper of the second potentiometer moves towards the ground terminal, producing a decreasing voltage. This inverse mechanical-to-electrical translation generates two distinct signals to verify the exact angular position of the throttle plate:
    1. Pin 1 (TPS Signal 1 - Increasing): Outputs the primary analog voltage. During bench characterization, this signal measured 1.18 V when the valve was at its minimum resting position with the engine off, scaling linearly to 4.26 V at the maximum mechanical opening (approximately 85% of the total cross-section).
    2. Pin 2 (Supply Voltage): Receives a stable 5 V reference signal from the ECU.
    3. Pin 3 (TPS Signal 2 - Decreasing): Outputs the redundant inverse voltage, starting at 3.90 V at the resting position and decreasing down to 0.785 V at maximum opening.
    4. Pin 4 (Ground): Serves as the common signal ground.
- **Actuation Circuit:** Pins 5 and 6: These terminals are dedicated to the internal DC motor, operating on a 12 V DC supply. In this test bench configuration, the data acquisition hardware does not directly drive the physical actuation of the butterfly valve; instead, the OEM Engine Control Unit (ECU) manages it entirely. The LabVIEW control system regulates engine throttle by generating simulated accelerator pedal analog signals and sending them to the ECU. The control unit processes these

requests and subsequently modulates the voltage across Pins 5 and 6 to dynamically adjust the valve's opening.



Figure 3.1.8-H5Ft OEM Throttle Valve

3.1.7 Exhaust Gas Pressure Measurement

For exhaust manifold pressure measurement, a relative pressure sensor manufactured by TC-Direct and shown in Figure 3.1.9 was connected via a dedicated pipe to a pressure tap drilled into the exhaust manifold. The operating range of this sensor spans from 0 to 2,5 bar (relative); this specific interval was selected because the maximum pressure of the exhaust gases at the turbine inlet typically reaches approximately 3 bar (absolute). Given that atmospheric pressure is roughly 1 bar, the maximum expected overpressure inside the exhaust manifold is around 2 bar (relative); therefore, a 2.5 bar relative sensor provides an adequate safety margin and prevents signal saturation under all engine operating conditions.



Figure 3.1.9-TC-Direct Pressure Sensor

These types of devices work differently with respect to the ones considered previously; specifically, the output is a current signal proportional to the measured pressure. This technology ensures more accurate measurement because the current value is not affected by voltage drops along the cable or electromagnetic noise induced by the engine test cell environment, which depend on the distance between the sensor and the DAQ board.

The sensor housing, made of stainless steel, encloses a ceramic sensing membrane positioned in direct contact with the exhaust gases. Piezoresistive elements are integrated onto the rear surface of this ceramic membrane to form a Wheatstone bridge circuit, which works together with an electronic signal conditioner acting as a voltage-to-current converter [9].

In the same way as in the previously described sensors, when exhaust gases exert pressure on the ceramic membrane, the resulting microscopic deflection induces mechanical strain on the resistors, altering their electrical resistance. This imbalance in the Wheatstone bridge generates a differential voltage proportional to the applied pressure. However, rather than transmitting this raw voltage directly, the internal electronics convert it into a standardized 4–20 mA current signal over a two-wire loop, where the minimum current of 4 mA corresponds to a pressure of 0 bar relative, while the maximum current of 20 mA corresponds to a pressure of 2.5 bar relative; any intermediate pressure value is translated into a perfectly linear current signal between the two thresholds.

The sensor has 2 electrical terminals: one is used to supply the electronics of the sensor with a voltage in the range of 10–30 V, and the other serves as ground to close the circuit. The sensor's terminals are connected to an external 12 V power supply. To convert the 4–20 mA current signal into a voltage signal readable by the NI-9205 DAQ board, a resistor is

placed in series within the circuit; the DAQ board then measures the voltage drop by connecting its input channels in parallel across this resistor.

For this application, a precision shunt resistor of 295 Ω was selected. This value converts the 4–20 mA current loop into a voltage signal readable by the DAQ module.

3.1.8 Fuel Flow Measurement

For fuel consumption monitoring, a Bürkert Type 8071 volumetric flowmeter was installed. This measurement system consists of a main flow sensor coupled with an integrated display unit showed in Figure 3.1.10 and Figure 3.1.11. The display not only provides real-time data visualization, but also serves as the control unit for parameter configuration and system settings.

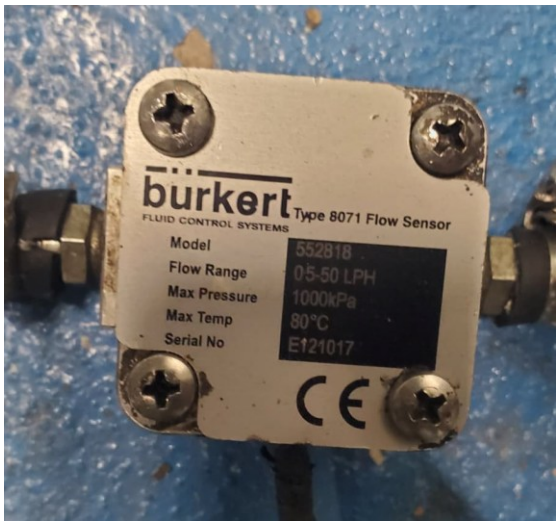


Figure 3.1.10-Bürkert 8071 Flow Meter

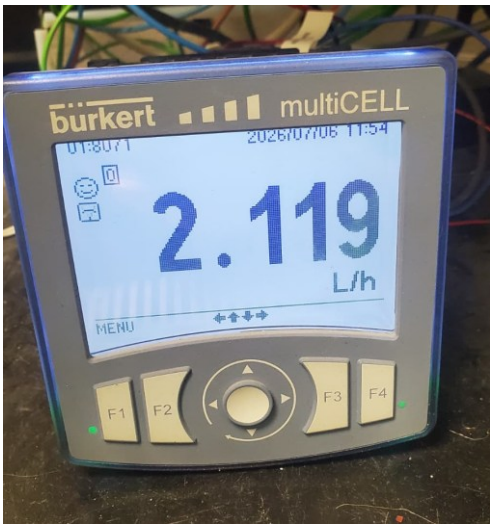


Figure 3.1.11-Bürkert 8071 Display

Regarding its physical installation within the fuel circuit, the sensor is positioned in series between the external low-pressure pump and the high-pressure injection pump installed on the engine. The device is designed to measure the volumetric fuel rate using an internal mechanism based on oval gears. As the fuel flows through the measuring chamber, it exerts pressure on the gears, forcing them to rotate. The rotational speed of the gears is directly proportional to the volume of fluid passing through the device [10]. The mechanical movement of these oval gears is detected by a magnetic Hall effect sensor. As the gears rotate, the Hall sensor reads the magnetic field variations and converts the mechanical rotation into an electric pulse signal, which is sent to the main display.

The flowmeter provides high accuracy across its measuring range (0.5 to 50 L/h), making it well suited to the fuel consumption typical of internal combustion engines.

To ensure high measurement precision under all conditions and for every fuel type, the flowmeter can be easily calibrated. The calibration process is performed directly through a dedicated built-in display function. After initiating the calibration mode, fuel was dispensed into a 1-liter calibrated graduated container. Once the test filling was complete, the actual measured volume collected in the container was manually entered into the display unit, allowing the system to automatically adjust its calibration factor (K-factor) to reflect the exact operating conditions (Figure 3.1.12).

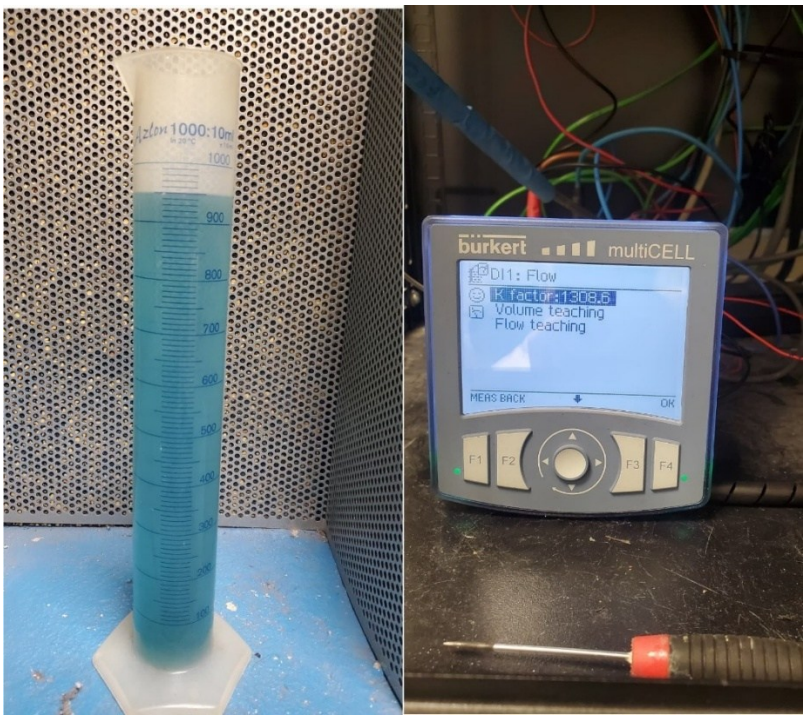


Figure 3.1.12-Fuel Flow Meter Calibration Procedure

The display then converts the value of measured flow rate into a standard 4–20 mA current signal. In the same way as the exhaust pressure sensor, a 495 Ω resistor is connected in series to the analog display output terminal, so that the NI-9205 board can measure the voltage drop across the resistor.

3.1.9 Coolant Flow Measurement

Regarding the coolant flow measurement, an Autosen AS010 volumetric flow meter was selected. This device was chosen as its operational specifications perfectly match the engine requirements. Specifically, its measuring range of 9 to 150 L/min accommodates the engine's maximum coolant flow rate under peak operating conditions, while its maximum fluid temperature rating of 125 °C provides an adequate safety margin above the engine's peak operating temperature (generally below 95 °C). Additionally, the sensor features an internal

diameter of 25 mm and 1¼" threaded connections, allowing for an easy mechanical integration with the existing coolant rubber hoses [11].

The Autosen AS010 operates based on the von Kármán vortex principle. When a non-streamlined obstruction (known as a bluff body) is placed inside the fluid stream, the fluid cannot remain attached to its downstream sides. This causes alternating vortices to detach continuously from one side of the body and then the other. The frequency at which these vortices are shed is directly proportional to the velocity of the flowing fluid [12]. Consequently, measuring the vortex shedding frequency allows the system to determine the volumetric flow rate. A key advantage of this physical principle is that the measurement depends solely on fluid velocity, making it independent of fluid properties such as density, viscosity, temperature, and pressure. As vortices alternately form on opposite sides of the bluff body, they create periodic pressure fluctuations across the obstruction. To capture these pressure variations, the flowmeter employs an integrated piezoelectric sensor. These pressure changes are transmitted to a piezoelectric crystal located inside the sensor assembly. The crystal converts the mechanical pressure oscillations into a frequency-based electrical signal [13]. Once generated, the raw frequency signal is processed by the flowmeter's integrated electronics. The signal is first amplified and filtered to reject background noise and mechanical vibrations. The internal transmitter then converts the shedding frequency into a standard 4–20 mA analog current output, which is directly proportional to the volumetric flow rate.

The sensor, shown in Figure 3.1.13, is powered through Pins 1 and 4 by the same 12 V power supply used for the exhaust pressure sensor and the fuel flow meter. Pin 4, in addition to providing ground to the sensor, also acts as a current signal output for the flow measurement. Similar to the previously described sensors, a 498 Ω shunt resistor is connected in series to the sensor output terminal, so that the DAQ board can measure the voltage drop across the resistor. The device also integrates a temperature sensor connected to pin number 3, which is not used for the purpose of this study.



Figure 3.1.13-Autosen AS010 Flow Meter

3.1.10 Air Mass Flow Measurement

Air mass flow measurement is performed using the traditional hot-film sensor adopted in automotive applications. The selected Mass Air Flow (MAF) sensor is the HFM 5 model 0 280 218 031 manufactured by Bosch and illustrated in Figure 3.1.14; it operates based on the principle of constant temperature thermal anemometry (utilizing hot-film technology).



Figure 3.1.14-Bosch HFM 5 MAF Sensor

The sensor directly measures the total air mass flow rate entering the engine cylinders, automatically compensating for ambient temperature, humidity, and atmospheric pressure variations without requiring separate barometric or air temperature calculations. The sensing element consists of a thin platinum film deposited on a silicon substrate, which acts as a

heated resistor, and an adjacent reference temperature sensor (Intake Air Temperature "IAT"). This sensor separates the thermal control from the actual flow measurement using two distinct circuits on a single chip shown in Figure 3.1.15. A dedicated closed-loop Wheatstone bridge continuously monitors the ambient intake air temperature and adjusts the electrical power supplied to a central heating resistor [14]. Its primary function is to maintain this heating element at a constant over-temperature (typically more than 100 °C) relative to the incoming air, ensuring a perfectly stable thermal reference regardless of environmental conditions. The actual air mass flow is evaluated by another Wheatstone bridge which includes two independent temperature-sensitive resistors positioned symmetrically upstream and downstream of the central heater [14].

Function diagram with connector-pin assignment.
1 Additional temperature sensor ϑ_u (not on version 4, Part number 0 280 218 008),
2 Supply voltage U_V, **3** Signal ground, **4** Reference voltage 5 V, **5** Measurement signal U_A.
ϑ Temperature-dependence of the resistor, R_H Heater resistor, U_K Constant voltage

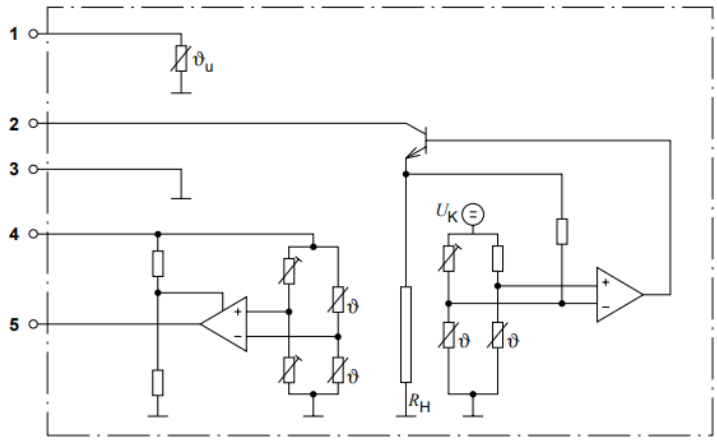


Figure 3.1.15-Function Diagram of the HFM 5 Sensor

In static conditions without airflow, the heater generates a symmetrical temperature profile. As air flows across the chip, it cools the upstream sensor and transports heat toward the downstream sensor by forced convection. This heat transfer mechanism is fundamentally described by King's Law:

$$Q = (A + B * \dot{m}^n) * (T_{element} - T_{air}) \quad (3.1)$$

In Equation (3.1):

- "Q" is the heat transfer rate,
- "$\dot{m}$" is the air mass flow rate,
- "A", "B", and "n" are empirical constants specific to the sensor's geometry [15].

The resulting forced convection creates a spatial temperature differential between the two sensors. An integrated hybrid circuit evaluates this thermal imbalance and converts it into a continuous analog output voltage, ranging from 0 to 5 V (approximately 1 V at idle and up

to 4.5 V at maximum engine load). This standardized voltage is strictly proportional to the air mass flow [14].

The Air mass flow meter has 5 electrical terminals:

- The first pin provides the output voltage signal of the auxiliary temperature sensor integrated in the device.
- The second pin delivers the main 12 V supply voltage to the sensor. This line provides the power required by the circuit to drive the central heating resistor and maintain its constant over-temperature.
- The third pin acts as a ground for the sensor power supply and provides a common reference for the output signals.
- The fourth pin delivers a stable 5 V reference voltage supplied directly by the Engine Control Unit. This line powers the precision internal electronics, specifically the measurement bridge and the operational amplifiers.
- The last pin carries the output voltage signals for the measurement of the air mass flow rate.

The second and third terminals were connected to the output of the 12 volt power supply, while the fifth terminal was connected to an input channel of the NI-9205 board. Since the acquisition mode was selected as “Differential”, the sensor’s output signal (Pin 5) was connected to the positive terminal of the differential channel pair, while a dedicated reference wire was connected between the sensor’s signal ground and the corresponding negative terminal of the pair. Pin 1 and 4 of the MAF sensor were left unconnected: pin 1 was omitted since the measurement of the air temperature is already performed by a thermocouple at the inlet of the MAF; while pin 4 was not connected because experimental testing confirmed that the internal electronics of the sensor provide internal regulation to power all the precision electronics (normally powered by the 5 V reference voltage) using the main 12 V supply voltage.

3.1.11 Grounding Architecture and Star-Point Configuration

To ensure electrical noise immunity, eliminate ground loops, and guarantee measurement precision across the overall instrumentation, a structured grounding strategy was implemented. The architecture relies on dedicated single-point (star-point) grounding nodes designed to isolate power returns, signal references, and protective earth paths before establishing an equipotential link.

DC Power and Industrial Sensor Star Point (Signal Return Node): A dedicated distribution bus serves as the common 0 V reference for all devices powered by the external 12 V DC laboratory power supply:

1. The negative return line of the external 12 V DC power supply.
2. The ground reference of the Mass Air Flow (Bosch HFM 5 MAF) sensor.
3. The return references of the current-loop industrial sensors (4–20 mA transducers).

The current return wires from the current industrial sensors were placed in series with precision shunt resistors. One terminal of the resistor is connected directly to the 0 V DC star point. From this same star point, a dedicated reference wire runs to the inverting input (AI-) of the NI-9205 differential channel. The opposite terminal of the resistor (where the sensor current enters) is wired directly to the non-inverting input (AI+) of the differential channel. This setup allows the acquisition module to read the voltage drop across the resistor.

Protective Earth Star Point (Safety Ground Node): A separate star configuration was established exclusively for chassis shielding and safety current dissipation:

1. The structural engine metal block.
2. The metallic chassis grounding lug of the NI cDAQ-9178 backplane.
3. The mains protective earth (PE) of the building electrical infrastructure.

Equipotential Bonding: To prevent electrostatic charge accumulation and ensure that the 12 V power supply shares the same zero-voltage reference as the building ground, the DC 0 V star point was connected to the Protective Earth star point with a dedicated copper wire. This deliberate single-point connection ensures a unified equipotential reference while preventing high-current ground return loops from circulating across measurement shields.

ECU Ground Isolation for RSE Measurements: The automotive Engine Control Unit (ECU) ground is maintained separate from the laboratory 12 V DC star point. The ECU negative reference wire is routed directly and exclusively to the “COM” terminal of the NI-9205 module. This allows the OEM sensors (MAP, high-pressure fuel rail, and electronic throttle position) to be sampled in “Referenced Single-Ended (RSE)” mode against the engine management system's exact reference potential, avoiding ground-potential offsets introduced by external auxiliary loads.

3.1.12 Engine Cooling System Optimization

To safely dissipate the heat rejected by the internal combustion engine during high-load steady-state testing, the test bench is equipped with a dual-circuit liquid cooling architecture.

However, during the initial commissioning phases, severe overcooling issues were identified, requiring a targeted hardware modification to the secondary cooling loop.

The cooling system operates using two distinct fluid loops. The primary closed-loop circuit circulates the engine coolant (a water-glycol mixture, or Paraflu) through the engine block and into a vertically mounted, large-scale tube-in-tube heat exchanger. The secondary open-loop circuit draws raw cooling water from a large underground reservoir (which acts as a centralized heat sink to cool both the eddy current dynamometer brake and the engine) and pumps it through the heat exchanger's internal tubes.

The thermal issue was experimentally discovered during preliminary test runs by monitoring the DAQ sensors and observing direct physical symptoms. Specifically, the temperature of the coolant returning to the engine remained constantly cold, while the primary liquid flowmeter installed on the engine loop consistently registered a flow rate of 0 L/min. These measurements confirmed that the engine's native thermostatic valve remained fully closed. Furthermore, a physical touch inspection along the heat exchanger's vertical body showed it took an excessively long time to warm from top to bottom, even under load. Under low-load operation or at engine idle, heat rejection from combustion was completely insufficient to overcome the thermal inertia and continuous chilling effect of the secondary pool water; under these conditions, the engine would practically never reach operating temperature.

To decouple the engine's warm-up phase from the massive heat sink, the cooling system was optimized by installing a mechanically actuated Danfoss AVTA thermostatic water valve (Figure 3.1.16; operating range 50–90 °C, rated for 130 °C max fluid temperature) on the secondary circuit.



Figure 3.1.16-Danfoss AVTA Thermostatic Valve

The valve is a self-acting, directly operated proportional regulator that operates entirely without electrical or pneumatic power supplies. A remote temperature bulb, connected via a metallic capillary tube, governs its operation and acts on an internal bellows actuator inside the valve body. The capillary sensing bulb is physically clamped to the primary circuit's return pipe, directly monitoring the temperature of the cooled Paraflu as it re-enters the engine block. As the primary engine coolant heats up, the thermostatic charge within the sensing bulb expands, transmitting a proportional hydrostatic pressure through the capillary against an adjustable internal counter-spring (mechanically calibrated to a setpoint of approximately 70 °C). When the returning coolant exceeds this temperature, the bellows displaces the internal valve spindle downward, opening the valve proportionally to the thermal load. During cold start-up or low-load idling, the valve remains completely sealed, immediately halting the secondary chilling flow and allowing the engine block to warm up rapidly.

To ensure system redundancy and operational flexibility, the regulation group was installed using a parallel three-way manifold configuration on the secondary discharge line, as it is illustrated in Figure 3.1.17:

- Regulated Branch: Houses the Danfoss AVTA valve along the main axis of the manifold to automatically control the secondary discharge flow.

- Manual Bypass Branch: A dedicated flexible bypass line was plumbed in parallel across the two T-junctions, governed by a quarter-turn manual ball valve (equipped with a red lever).

This dual-path hydraulic layout provides two practical operational advantages:

- Hardware Redundancy and Fault Tolerance: If the Danfoss valve experiences mechanical failure, becomes stuck, or requires maintenance, the operator can simply open the manual bypass valve. This allows continuous operation of the test bench without dismantling the entire piping assembly or halting testing activities.
- High-Load and Prolonged Testing: During heavy, prolonged engine test cycles requiring maximum thermal dissipation, the manual bypass can be fully opened to guarantee an uninterrupted, full-flow cooling loop through the heat exchanger.

This hardware intervention eliminated the excessive thermal inertia of the over-dimensioned heat exchanger, prevented overcooling under low-load conditions, enabled the native engine thermostat to open consistently, and established rapid and stable thermal equilibrium across the entire testing envelope.



Figure 3.1.17-Thermostatic Water Control Assembly with Danfoss AVTA Valve and Ball Valve Bypass

3.2 Software Environment and Performance Analytics

This paragraph presents the model developed to control and automate the engine test bench. LabVIEW was selected as the development platform primarily for its native integration with National Instruments DAQ hardware, its built-in libraries for acquisition and control, and its graphical dataflow architecture, which makes multi-task execution and parallel loop handling intuitive. Furthermore, LabVIEW allowed the design of a simple tab-based interface to keep all controls well organized.

The software structure is divided into three main parts:

- Acquisition: reads the voltage signals from all bench sensors (such as pressure, temperature, fuel flow, and airflow), applies sensor calibration curves to convert them into the actual measurements, and records all the acquired data into a proper log file.
- Control: manages the test bench operating conditions through dedicated loops and PID controllers, setting engine load and throttle position.
- Visualization: displays real-time bench parameters and defined targets on a custom user interface, computing instantaneous calculations from the acquired measurements.

In LabVIEW, the test bench software's core execution architecture is based on While Loops, the standard programming structure used to repeat operations continuously until a specific stop condition occurs. Using cyclical loops ensures that the software continuously samples the DAQ hardware, updates the user interface, executes control algorithms, and records both measured and computed data throughout the entire test bench run.

To manage tasks with different timing requirements without creating performance bottlenecks, the software architecture is divided into two independent, parallel While Loops:

- Main High-Speed Loop set with the clock at 20 ms (50 Hz): Handles all fast-changing input and output signals such as pressures, mass airflow, fuel consumption, engine speed, and torque; while running real-time control routines, parameter calculation, dashboard updates, and data recording. Operating at 50 Hz ensures rapid data acquisition and responsive dashboard updates while preventing overreactive or abrupt control actions on the test bench.
- Secondary Low-Speed Loop (10 Hz): Dedicated exclusively to thermal monitoring using thermocouples. In this loop, execution timing is not governed by a software wait function but is set directly by the hardware sampling rate configured in the DAQ Assistant. Decoupling this process avoids slowing down the main loop, as thermal

sensors have slower physical dynamics and their hardware acquisition requires extra conversion time.

3.2.1 Data Acquisition Architecture and Signal Processing

This subsection presents the core data acquisition architecture developed in the LabVIEW environment to monitor the engine test bench. It details how raw electrical signals are continuously acquired from the physical sensors through the National Instruments DAQ modules, specifically the NI-9205 and NI-9213. It also outlines the digital filtering strategies used to ensure signal integrity and describes the real-time data-recording framework, which logs the full set of acquired physical measurements and derived analytical quantities for subsequent post-processing.

Thermocouple Signal Acquisition: Unlike the traditional voltage inputs acquired by the NI-9205 board, temperature DAQ modules, such as the adopted NI-9213, operate at substantially lower acquisition rates. This lower sampling rate is due to the DAQ hardware, which uses high-resolution analog-to-digital conversion and Cold Junction Compensation (CJC) for microvolt-level signals [12]. Placing this slow hardware reading in the main software loop would have created a performance bottleneck, drastically reducing the execution frequency of the entire program.

To prevent this issue, temperature acquisition was decoupled into a dedicated parallel While Loop, shown in Figure 3.2.1, running at a suitable low sampling frequency. In this second loop, the DAQ Assistant block was added and configured in continuous acquisition mode to read 10 samples at 100 Hz. This configuration dictates the loop timing directly through the DAQ hardware buffer, updating the temperature values at an effective rate of 10 Hz (100 ms per iteration) without requiring an explicit software delay.

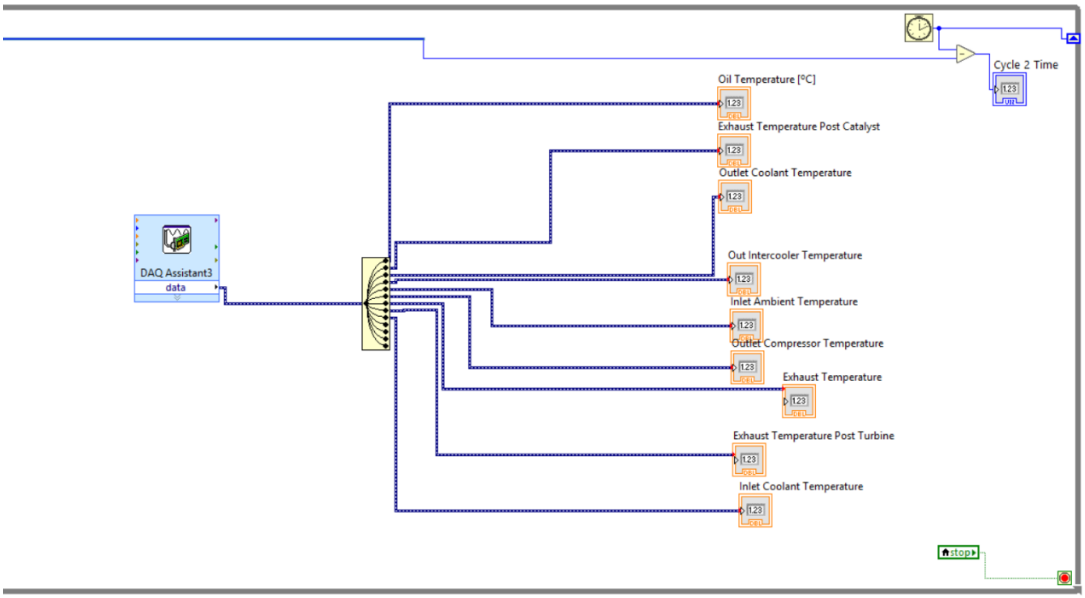


Figure 3.2.1-Temperature While Cycle

The DAQ Assistant block manages all thermal channels and, for each one, the sensor type and expected operating temperature range were individually specified, as shown in Figure 3.2.2, enabling LabVIEW to perform channel-specific conversion in the background. The data acquired in this While Cycle are then recalled in the main While Cycle as “Local Variables”.

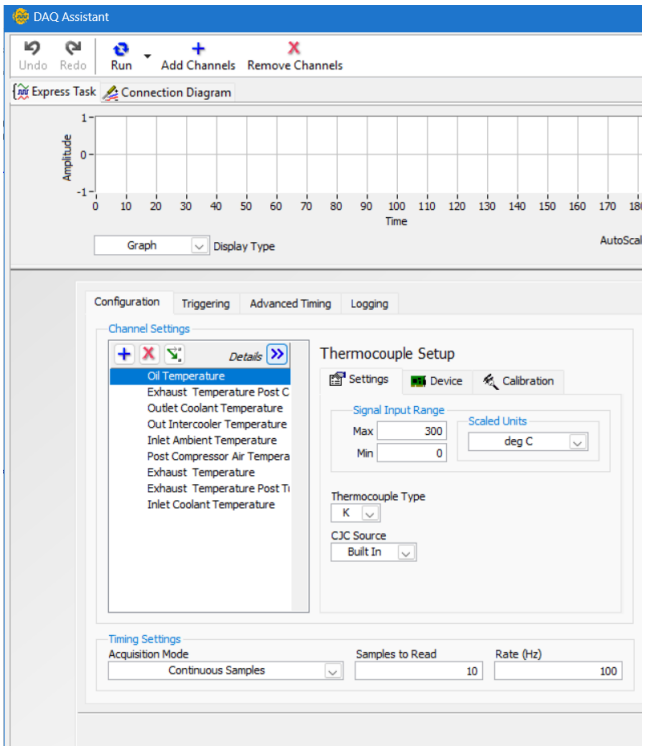


Figure 3.2.2-Temperature DAQ Assistant Configuration

High-speed While Loop: Within this loop, sensor data acquisition is centralized into a primary DAQ Assistant block configured to acquire all fast-response signals. This block handles the continuous acquisition of the main operating parameters of the engine and test bench, including intake, exhaust, and fuel rail pressures; intake mass airflow; throttle position; fuel and coolant flow rates; engine speed (RPM); and brake torque from the dynamometer load cell.

Inside this central module, illustrated by Figure 3.2.3, terminal configurations (Differential vs. RSE), voltage ranges, and custom scaling functions are assigned to each physical channel.

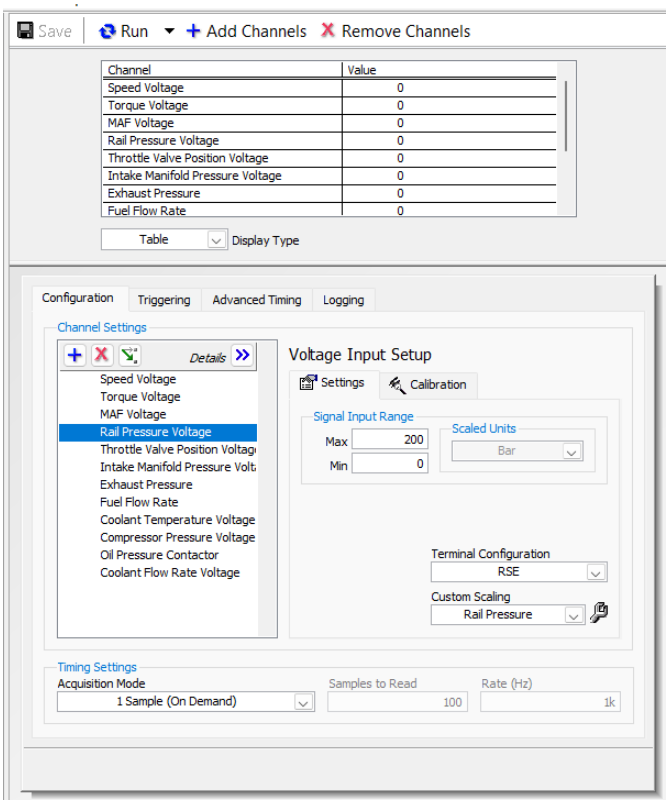


Figure 3.2.3-Input DAQ Assistant Block

Signal Filtering: To enhance signal integrity and eliminate high-frequency electromagnetic interference introduced by the engine test cell, a multi-stage digital filtering routine was implemented in LabVIEW:

- Median Filtering (Impulse Noise Rejection): All raw measurements first pass through a 3-point Median Filter ("Median PtByPt" block). This non-linear filter strips away isolated electrical spikes and impulsive noise without introducing phase distortion or dampening fast transient trends.
- Zero-Clamping and Noise Floor Thresholding: Following the median stage, a logical Select block applies a static lower threshold that clearly depends on the considered

measurement. If the acquired quantity falls below this threshold, the output is clamped directly to zero, effectively suppressing residual baseline drift and offset noise during engine idle or stationary phases.

- Moving Average Filtering (Smoothing): For sensitive channels requiring steady-state stability across thermodynamic balance equations, an additional Moving Average Filter ("Mean PtByPt" block) is applied downstream. This low-pass averaging attenuates residual stochastic noise, providing smooth curves on the front panel indicators.

Data Recording: To ensure structured and reliable data storage for post-processing, the acquisition chain organizes all live measurements before streaming them to disk using LabVIEW's native TDMS function blocks. Choosing a dedicated TDMS block over standard text or spreadsheet writers offers key practical advantages on the engine test bench:

- High Execution Speed without Test Delays: TDMS blocks stream binary data directly to disk with minimal computing effort, ensuring that real-time data logging never slows down or interferes with the continuous 50 Hz acquisition loop.
- Automatic Data Organization: Channel names, measurement units, and absolute timestamps are attached to each signal automatically by the block itself, eliminating the need to manually build text headers.
- Direct Export to Microsoft Excel: The resulting files can be opened immediately in Microsoft Excel using the NI TDM Excel Add-In.

Before routing the multi-channel acquisition data into the recording module, all calibrated sensor measurements (including pressures, fluid flows, temperatures, engine speed, and brake torque) along with computed performance metrics (such as power and efficiencies) are aggregated into a unified LabVIEW cluster.

- Bundle by Name: Collects individual scalar variables into a single composite data bus, explicitly mapping each parameter to its named cluster element.
- Unbundle by Name: Unpacks the cluster inside the logging routine to extract the required subsets of parameters.

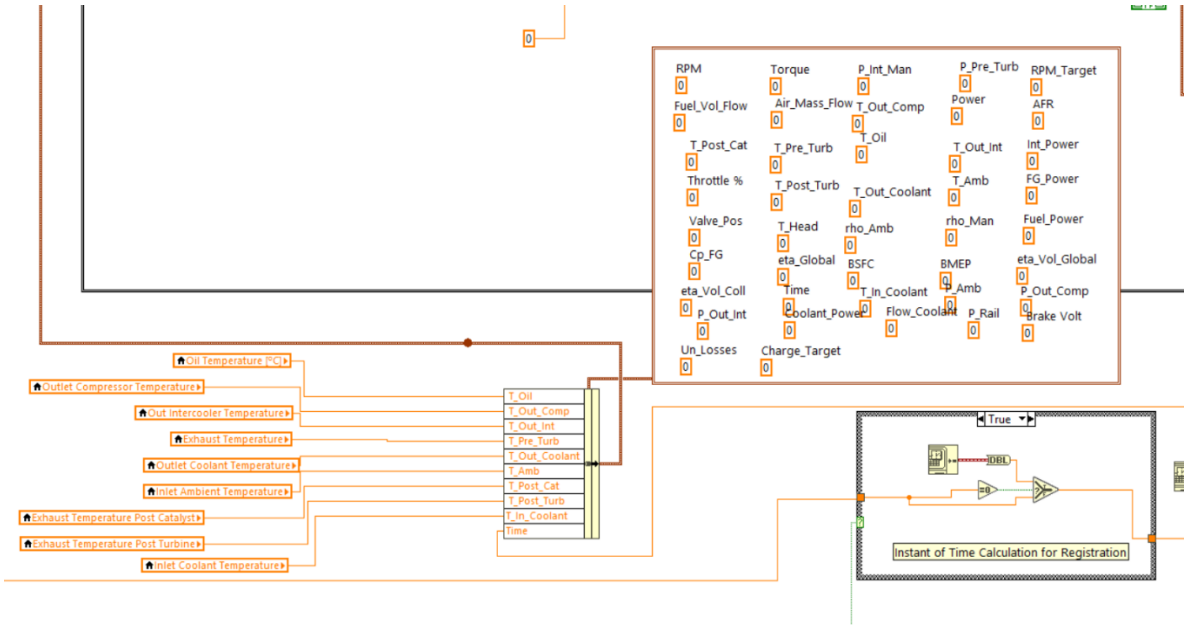


Figure 3.2.4-LabVIEW Block Diagram Detail Illustrating the Master Cluster Definition and Signal Aggregation

Figure 3.2.4 illustrates the definition and aggregation of the complete parameter dataset within the LabVIEW architecture. The large container on the right shows the master cluster definition, which contains all the experimental variables logged during bench testing. This comprehensive structure includes all measured engine operating conditions, calibrated sensor readings, thermodynamic fluid states, and derived performance metrics.

On the left side of the diagram, a subset of acquired data, specifically the thermocouple temperature readings together with the Time reference, is injected into the data cluster via a Bundle by Name node. Although the remaining engine parameters defined in the main cluster are packaged in other dedicated sections of the code, this section highlights how individual signal lines are mapped into their named cluster elements before being transmitted to the downstream TDMS recording module.

The TDMS recording routine implements a standard file-handling lifecycle divided into three main blocks:

- TDMS Open (Figure 3.2.5): Initiates a recording session upon operator request, creating a target file with a defined name and folder path.

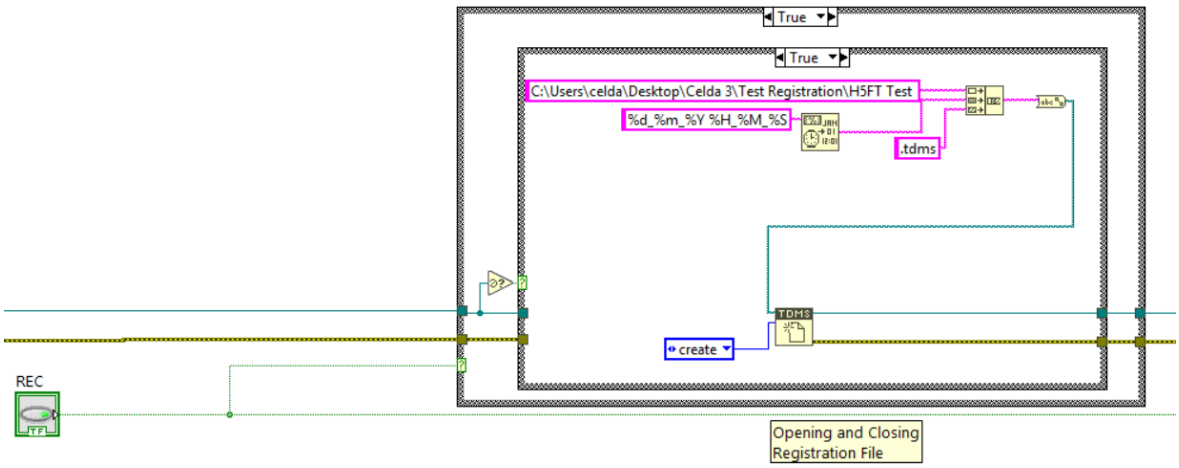


Figure 3.2.5-TDMS Open Block

- TDMS Write (Figure 3.2.6): Extracts the packed data from the cluster and writes them to the file. Although the main acquisition loop executes at 50 Hz, an internal timing Case Structure decimates the logging interval to write a frame every 100 ms (10 Hz). This maintains full fidelity over dynamic engine transients while preventing unnecessarily large file sizes during long testing sessions.

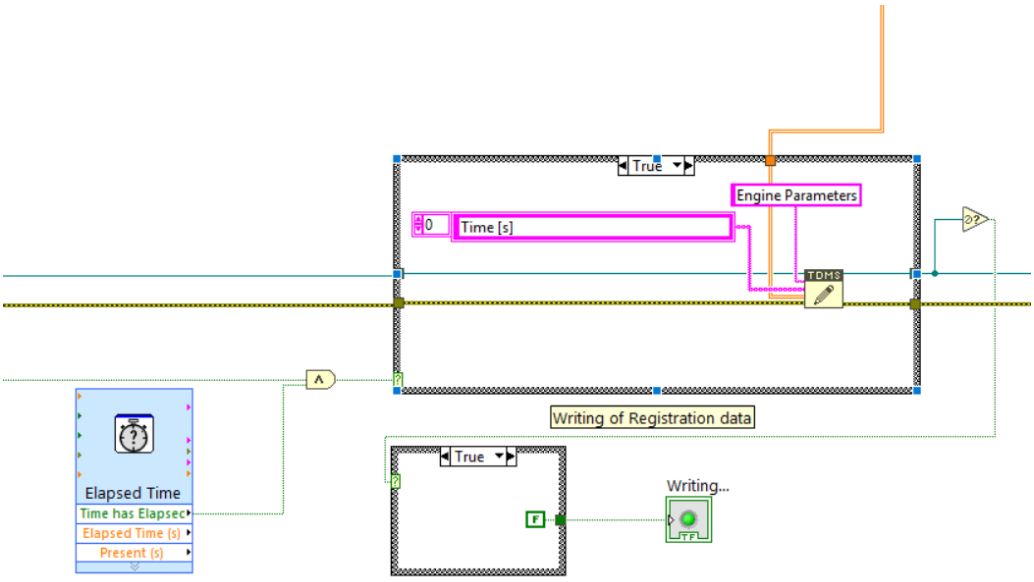


Figure 3.2.6-TDMS Write Block

- TDMS Close: Safely flushes internal buffers and terminates the file reference when recording is toggled off, protecting data integrity against unexpected system interruptions.
- Visual Indicator: A virtual LED on the Front Panel is tied directly to the logging Boolean state to give the operator real-time confirmation of active recording.

To ensure that each recorded dataset starts with a clean time base beginning strictly at 0.0 s, a dedicated elapsed time routine, shown in Figure 3.2.7, was implemented using a conditional Case Structure and a Shift Register. When the recording state is switched to True, the shift register initially supplies a value of 0. An "Equal to Zero" comparison node detects this initial state on the first logging iteration. Through a "Select" function, the cycle captures the current system timestamp via the "Get Date/Time In Seconds" function and latches it into the shift register as the reference start time 0. On subsequent iterations of the active logging session, the comparison evaluates to False, preserving the latched reference without overwriting it. At each cycle, the current instantaneous timestamp "t" is read and subtracted from the latched initial timestamp "t_0" via a subtraction node $t - t_0$. This differential calculation generates a continuously increasing elapsed time value (in seconds) that is injected directly into the master cluster as the "Time" channel. When the operator halts recording (switching the case to False), the shift register passes a reset value of 0 back to the loop boundary; as a result, whenever a new logging session is initiated, the time vector automatically resets and starts counting from zero again.

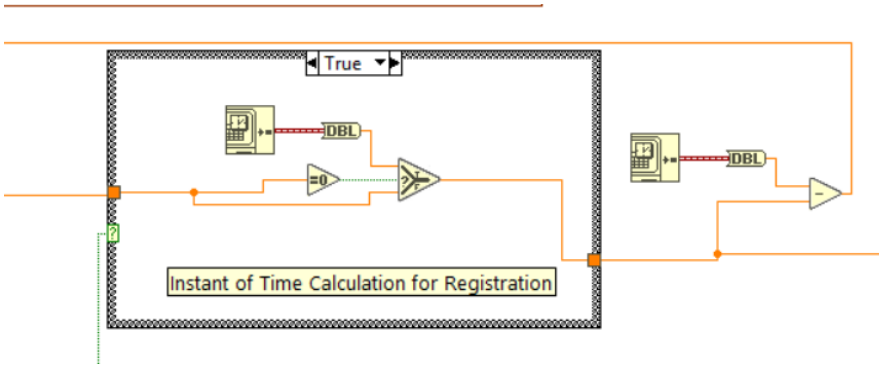


Figure 3.2.7-Elapsed Time Calculation Logic for Test Data Recording

Software Execution Benchmarking and Loop Timing Optimization: During preliminary experimental testing on the test bench, timing benchmarks revealed significant performance bottlenecks within the main While Cycle. To calculate the actual effective loop cycle period, a dedicated diagnostic sub-routine based on the "Tick Count" function and a shift register was implemented.

This real-time measurement revealed that when multiple analog input and output channels and scaling equations were bundled directly inside the high-level "DAQ Assistant Express" block, the loop execution time deteriorated substantially. Instead of maintaining the targeted deterministic loop cycle of 20 ms, the measured loop iteration period exhibited severe instability and jitter, fluctuating between 150 ms and 200 ms. This latency occurred

because Express VI blocks re-evaluate configurations and dynamic data types on each iteration, causing significant CPU bottlenecks when handling high channel counts.

To eliminate this bottleneck and restore deterministic execution, a different function was implemented:

- The channel routing, differential terminal modes, sampling rates, and custom voltage-to-physical linear scalings were exported from the DAQ Assistant block and configured directly as a Global DAQmx Task within NI Measurement & Automation Explorer (NI MAX).
- On the LabVIEW Block Diagram, the Express VI was replaced with direct, lightweight NI-DAQmx API nodes, passing the pre-configured MAX Task reference directly into a continuous DAQmx Read function.

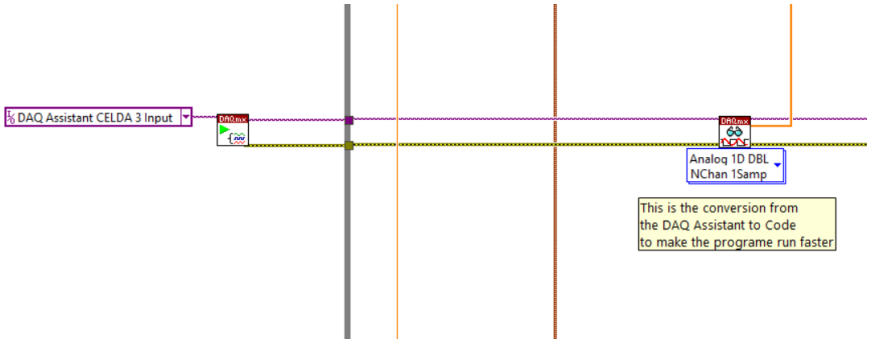


Figure 3.2.8-DAQmx Task Loop

As illustrated in Figure 3.2.8, the practical implementation of the optimized code physically separates the hardware initialization phase from the continuous data retrieval process. This is achieved by distributing the native DAQmx functions across the main While Loop boundary:

- Task Initialization (Outside the Loop): The elements on the left side of the loop boundary consist of the task reference control, saved in the NI-MAX application (labeled "DAQ Assistant CELDA 3 Input"), wired into the DAQmx Start Task VI (represented by the node with the green play arrow). Placing this block strictly outside the acquisition loop ensures that all computationally heavy operations are executed only once when the program launches.
- Continuous Data Retrieval (Inside the Loop): The node on the right side is the DAQmx Read VI, which is embedded inside the high-speed While Loop. As indicated by its polymorphic configuration label (Analog 1D DBL NChan 1Samp), this block is programmed to fetch a single synchronized data point from all active channels simultaneously, outputting the data as a one-dimensional array of Double-

precision floating-point numbers. Because the hardware task has already been fully initialized and started outside the loop, this read node simply polls the latest available values directly from the hardware buffer, executing almost instantaneously on each iteration without any configuration overhead.

By offloading channel allocation and memory buffering, and scaling directly to the hardware driver level prior to loop execution, CPU processing overhead was eliminated. The effective loop period calculated by the diagnostic routine confirmed that the main While Loop execution stabilized strictly at the targeted 20 ms, ensuring jitter-free data acquisition during engine testing.

3.2.2 Sensor Calibration and Signal Conversion

Once the DAQ hardware acquires raw analog signals, they must be converted into physical engineering units before they can be displayed on the real-time dashboard or fed into computational routines. This subsection details the specific electrical interfacing required for each sensor group (such as the integration of shunt resistors and terminal configurations (Differential or RSE)) alongside their experimental calibration procedures. The derivation of specific transfer functions, ranging from linear equations to higher-degree polynomials, is presented for each channel to accurately determine actual physical measurements, such as manifold pressures, fluid flows, and air mass flow.

ECU Sensors Signal Acquisition: Compressor outlet air pressure, intake manifold air pressure, fuel rail pressure, and the throttle valve position signals are integrated directly into the high-speed main While Loop.

Because the DAQ module reads raw analog voltage signals (0–5 V) from the devices, these electrical values must be converted into engineering units using dedicated transfer functions. To determine this relationship experimentally, we performed an on-bench calibration procedure with the engine running under various load and speed conditions. The diagnostic tool connected via OBD-II served as the primary reference standard, providing the true physical values (both pressure levels and throttle plate opening percentages) directly computed by the stock ECU.

LabVIEW recorded the raw voltage levels produced by the pressure transducers across the entire operating range. The coupled datasets were compared to extract the characteristic transfer functions. The relation between discrete values of pressure and voltage showed an essentially linear response, as shown in Figure 3.2.9 and Figure 3.2.10. Since the considered air pressure sensors belong to different models, their calculated pressure-voltage

relationships were slightly different. Specifically, the sensor at the intercooler outlet also integrates a temperature sensor, although it was not used for this study.

Similarly, the acquisition of the Electronic Throttle Body (ETB) was performed by reading only its primary increasing analog signal (Pin 1) to optimize channel usage on the NI-9205 module. Through the same OBD-II correlation methodology, the raw analog output was mapped to the ECU throttle position parameter, yielding a linear response spanning from 1.18 V at the idle resting position up to 4.26 V at the maximum opening (approximately 85% of the total cross-section) (Figure 3.2.11).

The resulting linear calibration equations for the pressure transducers, along with the percentage scaling for the throttle valve position, were then embedded directly into the DAQ Assistant custom scaling settings. This allows LabVIEW to automatically convert incoming raw voltages into accurate physical values during continuous execution.

The Referenced Single-Ended (RSE) configuration was chosen for all these ECU-linked sensors. Consequently, the acquisition board calculates the potential difference between the active input channel and the common reference pin “COM”. To avoid floating measurements and ground loops, this “COM” pin was directly tied to the ECU ground point through a dedicated reference cable, ensuring an extremely stable baseline for all the aforementioned low-voltage signals.

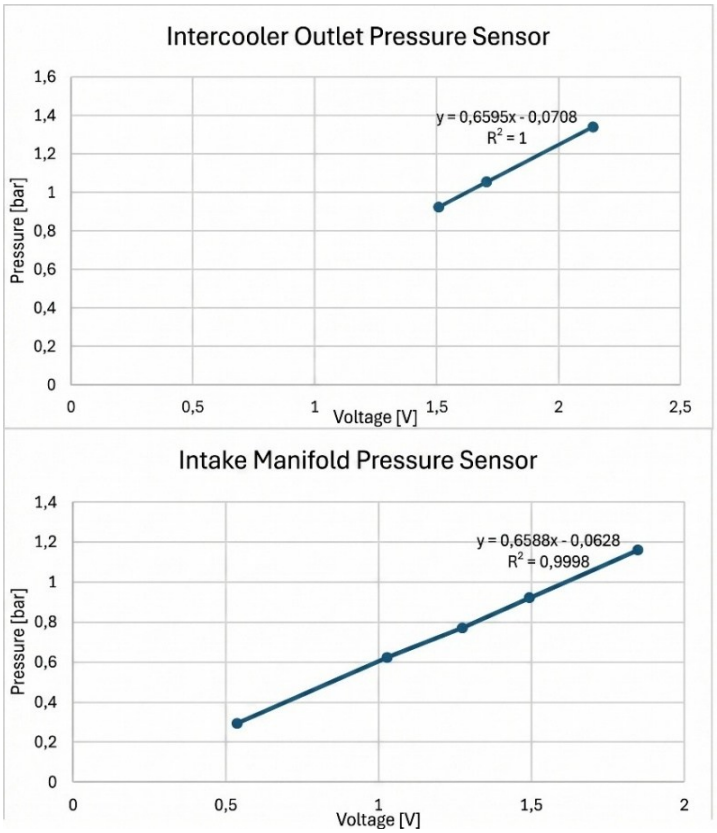


Figure 3.2.9-Air Pressure Calibration Curves

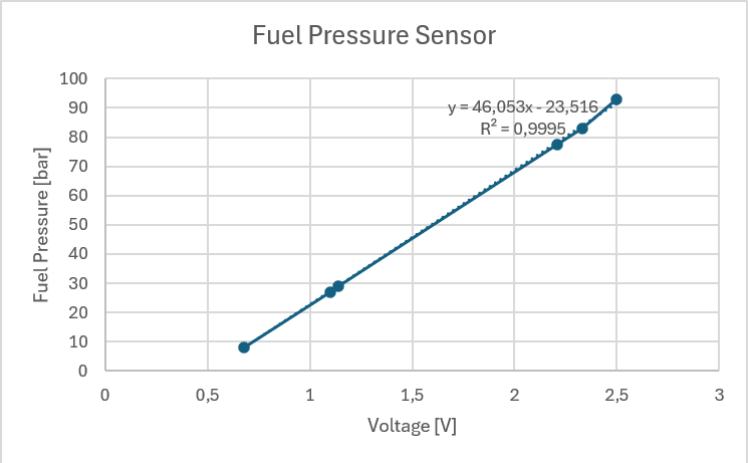


Figure 3.2.10-Fuel Pressure Sensor Calibration Curve

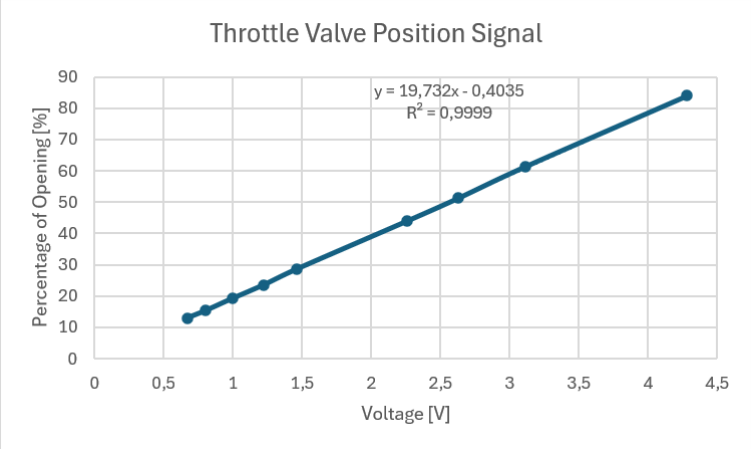


Figure 3.2.11-Throttle Valve Position Signal Calibration Curve

Air Mass Flow Signal: The relation between the air mass flow and the signal voltage of the MAF sensor was determined by two different experimental tests. This calibration methodology was necessary because the engine lacks a native MAF sensor; instead, the original ECU estimates intake air mass flow using a speed-density approach based on intake manifold absolute pressure and temperature.

- At partial loads, this approach can be inaccurate due to intake pulsation; therefore, in this operating region, the air mass flow rate was computed from the measured fuel flow rate under the assumption of stoichiometric combustion $\lambda = 1$) with a constant air-to-fuel ratio of 14.25.
- Conversely, at high loads, the ECU disables stoichiometric control in favor of mixture enrichment for engine thermal protection, making the constant AFR assumption inapplicable. However, the ECU's speed-density model remains sufficiently accurate under these higher airflow regimes; therefore, the air mass flow rate acquired via the

OBD interface was directly matched against the external MAF sensor's analog voltage signal to complete the calibration curve.

Finally, the curve built by the 28 data points relating air flow rate and voltage, was fitted using a sixth.-degree polynomial function as shown in Figure 3.2.12.

The NI-9205 acquisition board is able to read a voltage signal between two inputs of a channel or between an input channel and the "COM" port. To maximize signal integrity, the acquisition mode was set to "Differential". In this configuration, the NI-9205 couples two specific hardware channels (AI+ and AI-) to measure the voltage difference between them, rather than referencing the signal to the module's internal ground.

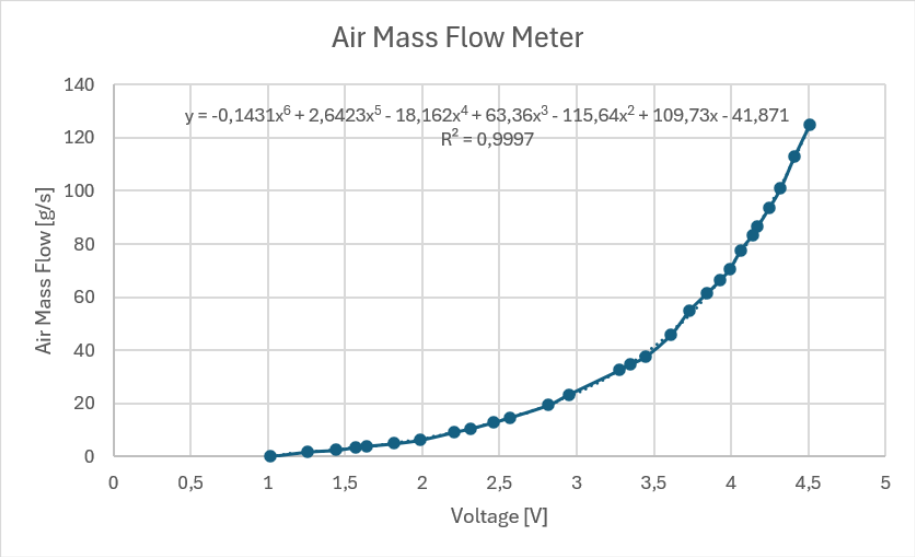


Figure 3.2.12-Air Mass Flow Meter Calibration Curve

Industrial-Grade Transmitters: The instrumentation setup includes industrial-grade transmitters to measure exhaust pressure and volumetric engine coolant flow rate. These transducers output a standard 4–20 mA current loop signal, which ensures high immunity against electromagnetic noise. However, as explained in paragraph 3.1, because the analog input module NI-9205 measures voltage, these current signals must be converted to a readable voltage range before acquisition. To achieve this, a precision shunt resistor was wired across each input channel. Applying Ohm's law: $\Delta V = R * I$, the incoming 4–20 mA current is translated into a proportional voltage signal readable by the NI-9205. Because these standard industrial sensors have a linear response, defining the transfer function in LabVIEW is straightforward. The minimum current 4 mA, corresponding to the minimum voltage ΔV_{min}, aligns with the lower bound of the sensor's physical measuring range y_{min}, while the maximum current 20 mA, corresponding to ΔV_{max}, defines the full-scale value y_{max}.

$$y = y_{min} + \frac{y_{max} - y_{min}}{V_{max} - V_{min}} * (V - V_{min}) \quad (3.2)$$

The continuous linear relation, illustrated by Equation (3.2), was programmed directly into the custom scaling interface of the DAQ Assistant, allowing instantaneous conversion from acquired voltage to physical units.

To prevent ground mixing and ground-loop offsets, both sensor channels are configured in "Differential" terminal mode on the NI-9205. The stock vehicle sensors and the engine ECU share a common ground connected to the DAQ ground reference "COM", whereas these external industrial transmitters are powered by a dedicated auxiliary 12 V power supply. Measuring the voltage drop differentially directly across each shunt resistor isolates the acquisition from potential differences between the engine control unit and the auxiliary power supply ground.

- For the exhaust pressure transmitter, a 295 Ω shunt resistor was adopted, yielding an acquired range from $1.177\ V$ $(295\ \Omega * 0.004\ A)$ to $5.886\ V$ $(295\ \Omega * 0.02\ A)$. This lower resistance value was chosen to comply with the transmitter's maximum allowable loop load impedance under the available loop supply voltage, ensuring sufficient voltage headroom across the sensor terminals and preventing signal saturation at peak currents (20 mA). Having these two defined operating points makes it straightforward to establish the exact linear calibration curve illustrated by Figure 3.2.13.

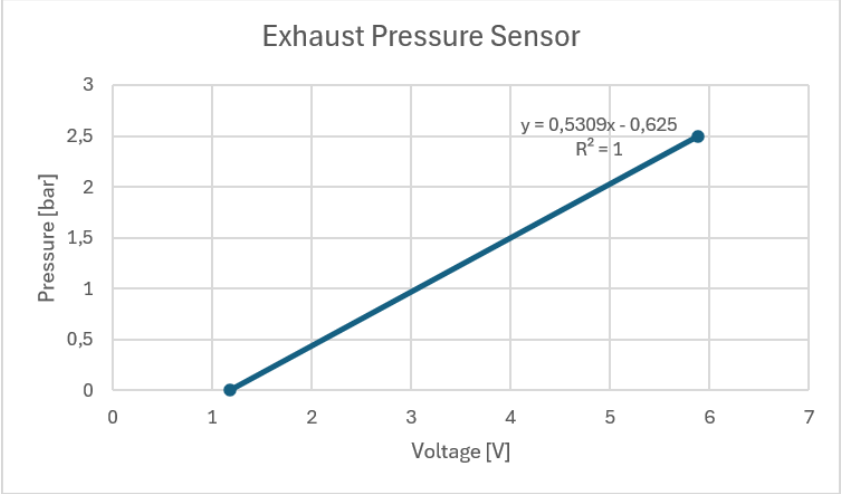


Figure 3.2.13-Exhaust Pressure Sensor Calibration Curve

- For the Coolant Flow Sensor a 498 Ω resistor was selected to maximize the dynamic range of the DAQ channel, converting the 4–20 mA current range into a voltage range from $1.992\ V$ $(498\ \Omega\ *\ 0.004\ \mathrm{A})$ to $9{,}960\ V$ $(498\ \Omega\ *\ 0.02\ \mathrm{A})$. This setup fully utilizes the native 0–10 V input range of the NI-9205, optimizing analog-to-digital quantization resolution. For this sensor, the lower voltage limit (1.992 V)

corresponds to 0 L/min, while the upper limit (9.960 V) corresponds to full-scale flow of 150 L/min. With these two boundary conditions clearly identified, the sensor's calibration curve can be derived directly as shown in Figure 3.2.14.

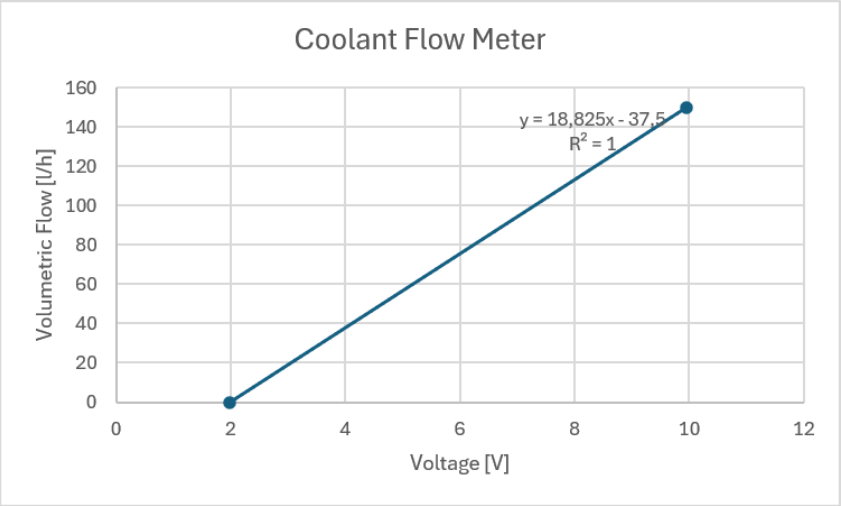


Figure 3.2.14-Coolant Flow Meter Calibration Curve

Fuel Flow Meter Signal Acquisition: The Bürkert Type 8071 industrial transmitter generates a 4–20 mA current loop output directly proportional to the volumetric fuel flow rate.

As with the other industrial transducers, the flowmeter is powered by the dedicated auxiliary 12 V power supply. To prevent mixing the auxiliary supply ground with the ECU ground, the signal is wired in "Differential mode" into the NI-9205 module.

A shunt resistor of 495 Ω was connected across the differential input terminals (AI+ and AI−). This resistance value was selected to map the nominal current loop into an approximate 1.97–9.81 V span, fully exploiting the native 0–10 V analog input range of the acquisition card and maximizing measurement resolution.

To ensure high accuracy and compensate for the actual component tolerances, an experimental fine-tuning procedure available through the instrument display was performed (Figure 3.2.15): a calibrated digital multimeter was inserted into the current loop to measure the exact minimum and maximum current boundaries (I_{min} at zero flow and I_{max} at full scale generated by the transmitter).

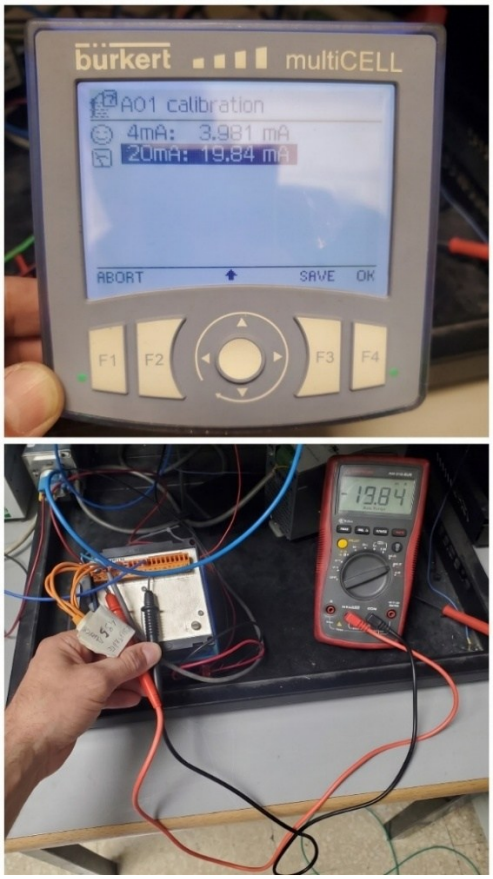


Figure 3.2.15-Fuel Flow Meter Fine Calibration

The measured zero-flow current boundary was $I_{min} = 3.981\ mA$ (instead of nominal 4.000 mA), corresponding to a measured lower voltage limit of 1.973 V, while the measured full-scale current boundary was $I_{max} = 19.84\ mA$ (instead of nominal 20.000 mA), corresponding to an upper voltage limit of 9.809 V. By mapping these verified voltage limits to the volumetric range calibrated in the hardware setup (from 0 L/h up to the maximum calibrated flow rate of 50 L/h), the linear transfer function shown in Figure 3.2.16 was accurately defined and embedded into the DAQ Assistant custom scaling settings.

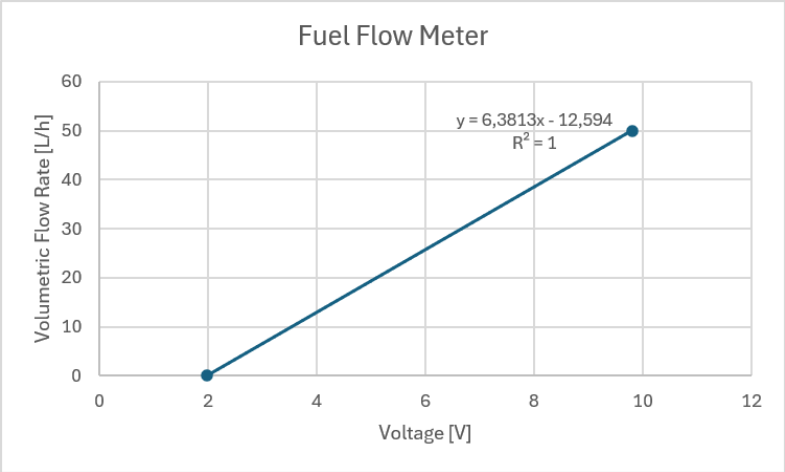


Figure 3.2.16-Fuel Flow Meter Calibration Curve

3.2.3 Test Bench Control

To accurately manage the engine test bench during both steady-state and transient operations, a closed-loop control strategy was implemented in LabVIEW. The core of this automation system relies on Proportional-Integral-Derivative (PID) algorithms to continuously regulate the two primary actuators: the dynamometer braking voltage and the electronic throttle position.

The fundamental principle of a PID controller is to continuously calculate an error value "e(t)" as the difference between a desired Setpoint "SP" and a measured Process Variable "PV":

$$e(t) = SP(t) - PV(t) \tag{3.3}$$

Based on this real-time error, the controller applies a correction based on proportional, integral, and derivative terms. The overall control effort "u(t)" is defined by the standard continuous-time PID Equation (3.4).

$$u(t) = K_c * \left[e(t) + K_i \int_o^t e(\tau) d\tau + K_d \frac{de(t)}{dt} \right] \tag{3.4}$$

Where:

- K_c (Proportional Gain): Reacts instantaneously and proportionally to the current error.
- K_i (Integral Gain): Accumulates past errors over time to eliminate steady-state offset.
- K_d (Derivative Gain): Predicts future error trends to dampen oscillations and improve stability.

To ensure mathematical stability and standardize the control logic across different physical variables, the LabVIEW PID blocks are engineered to operate entirely on a normalized 0–100 % scale. Both the input parameters (SP and PV) and the resulting control effort (u(t)) are expressed as percentages, bounded between 0 % and 100 %. This normalized architecture applies to both the engine speed control and engine charge control loops, as detailed below.

Engine Speed Control: The software architecture for dynamometer control was developed with two primary design objectives: the capability to reach a target engine speed in a reasonable time (rapid setpoint tracking) and the ability to maintain the target speed with minor fluctuations (steady-state stability of ±15 rpm). To achieve these goals, the first PID loop (Figure 3.2.17) regulates the engine speed by adjusting the control voltage supplied by the

Owon power supply to the eddy-current brake, thereby modulating the resulting electromagnetic braking load.

- Inputs (SP and PV): The operator inputs a desired target engine speed defined within a theoretical range of 0–6000 RPM. The software maps this user target to a 0–100 % scale. Simultaneously, the actual engine speed measured by the DAQ system (operating within a physical range of 0–6000 RPM) is also converted into a corresponding percentage. This normalized actual speed acts as the continuous Process Variable (PV).
- Output and Conversion: Based on the computed error, the PID algorithm outputs a control effort strictly bounded between 0 % and 100 %. To physically actuate the dynamometer, this percentage must be translated back into an electrical signal. The software scales the percentage-based output into a proportional command voltage from 0 V to 55 V, which directly drives the eddy current brake power supply.

The PID gain calibration for the dynamometer brake was performed through extensive experimental testing across a wide matrix of engine speeds and loads. Initially, classic heuristic tuning techniques such as the Ziegler-Nichols method, which involves increasing the proportional gain until the system reaches sustained oscillations to calculate the parameters, or the Cohen-Coon step-response method were evaluated. However, these traditional linear methods did not yield satisfactory results, often producing overly aggressive or unstable behavior due to the high inertia and severe non-linearities of the internal combustion engine. Consequently, an experimental tuning process was adopted. Through iterative tests under various operating conditions, an optimal set of static gains was identified. Although not perfectly suited to every point on the engine map, this experimentally tuned configuration provided the most robust and stable compromise for general bench testing. The optimal values of the gains are shown in Figure 3.2.24.

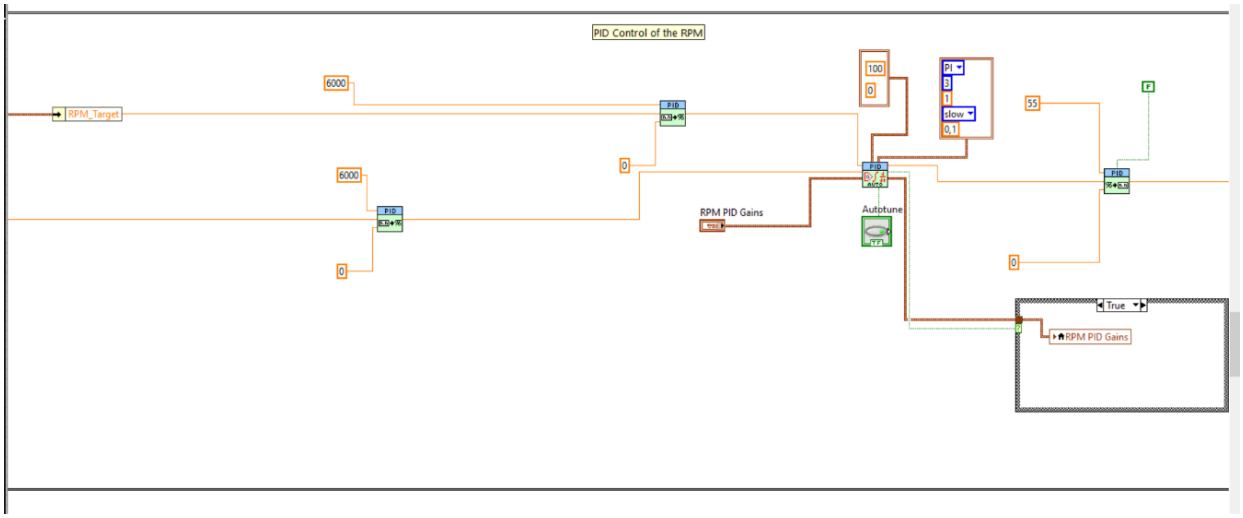


Figure 3.2.17-PID Speed Control Loop

Charge Control: The second PID loop (Figure 3.2.18) regulates electronically the throttle to achieve a specific target "Charge" (defined as a percentage of the maximum torque available at any given engine speed). A crucial architectural prerequisite for this loop is preventing dynamic cross-talk and conflict with the primary engine speed controller. Because maintaining a highly stable rotational speed is paramount, the charge controller is deliberately tuned with a less aggressive response profile. By intentionally slowing down the throttle control effort relative to the dynamometer brake loop, the two controllers operate on decoupled timescales, ensuring that rapid throttle modulations do not destabilize the engine speed.

- Setpoint (Target Charge): The controller continuously reads the instantaneous RPM and feeds it into an embedded formula node containing the engine's full-load torque curve. This formula calculates the theoretical maximum torque available at that specific RPM. The target torque is then determined by multiplying this maximum value by the operator's desired "Charge Percentage".
- Process Variable (Filtered Feedback): The feedback signal is the actual instantaneous torque measured by the load cell. Because raw torque signals exhibit severe oscillations, particularly higher torque fluctuations at low engine speeds due to discrete, low-frequency cylinder combustion pulses, filtering the feedback signal is strictly necessary. The raw measurement is passed through a Moving Average Filter with a window size of 42 samples to mitigate these fluctuations. The filtered torque is then normalized against the maximum torque to generate a stable 0–100 % actual charge value (PV).
- Direct Actuator Output: Unlike the brake controller, the throttle controller does not require any unit conversion at its exit. The PID loop outputs a direct control effort

scaled from 0 % to 100 %, which perfectly corresponds to the native command signal required by the ECU.

Much like the dynamometer control loop, the PID parameters for the electronic throttle were determined experimentally through extensive bench testing. During this empirical calibration, the Proportional gain (K_c) and Derivative time (T_d) were found to be stable across the map and were fixed at 0.00018 and 0.008 min, respectively. However, it was observed that a single, static Integral time (T_i) could not maintain stability across the entire engine operating envelope. To solve this, an RPM-dependent Gain-Scheduling strategy was implemented specifically for the Integral time:

- Low-Speed Regime (< 1500 RPM): A fixed, higher integral time of $T_i = 6 \times 10^{-5}$ min is applied. Because the integral control effort is inversely proportional to the integral time, this higher parameter effectively reduces the controller's aggressiveness. This is deliberately chosen to prevent severe overshoots and hunting when airflow velocities are low and combustion torque ripples are most pronounced.
- High-Speed Regime (> 2200 RPM): A lower, fixed integral time of $T_i = 2 \times 10^{-5}$ min is applied. This increases the integral action, ensuring rapid throttle response and efficiently eliminating steady-state errors when engine fluid dynamics are faster and inherently more stable.
- Transitional Regime (1500–2200 RPM): To prevent discontinuous jumps in the control effort when crossing the operational boundaries, an embedded formula node computes a continuous linear interpolation of the integral time between the low-speed and high-speed values. The software dictates the transition according to the mathematical relationship (3.5).

$$T_i = X_2 + (X_3 - X_2) \cdot \frac{X_1 - 1500}{700} \tag{3.5}$$

Where X_1 is the instantaneous engine speed (RPM) acting as the independent variable, X_2 represents the low-speed integral boundary (6×10^{-5} min), X_3 represents the high-speed integral boundary (2×10^{-5} min), and the denominator 700 defines the RPM width of the transition window ($2200 - 1500$ RPM).

This adaptive, experimentally derived calibration ensures smooth, stable throttle actuation across the engine's operating range, preventing oscillatory feedback loops while preserving steady-state speed integrity.

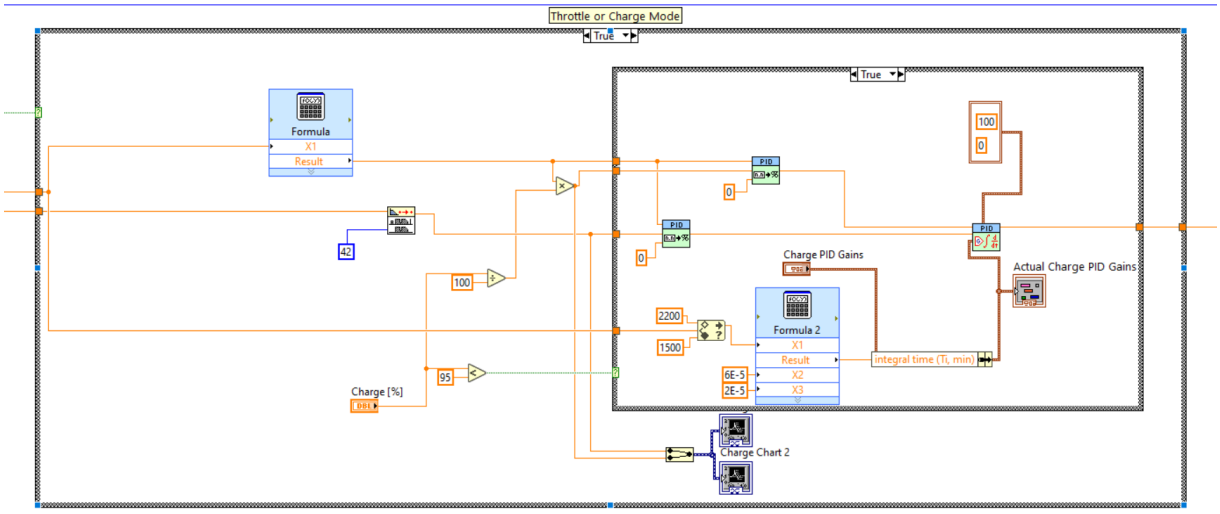


Figure 3.2.18-PID Charge Control Loop

To ensure the physical integrity of the engine and the test rig during testing, a dedicated fail-safe control loop was integrated into the system architecture. As illustrated in the block diagram in Figure 3.2.19, this safety loop continuously monitors the engine speed (RPM) and the dynamometer brake status, overriding the primary virtual accelerator outputs to force an instantaneous throttle cut-off (Throttle = 0%) under two critical fault conditions:

- Absolute Engine Overspeed (Mechanical Limit): The upper logical path acts as a rev-limiter. If the engine speed exceeds the absolute safety threshold of 5500 RPM, a true Boolean signal is generated. This condition triggers the safety shutdown regardless of the dynamometer's operational state, protecting the engine's internal mechanical components from excessive rotational speed.
- Unloaded Overspeed (Loss of Load Protection): The lower logical path is specifically designed to handle sudden load losses. If the dynamometer brake is deactivated (Brake ON/OFF = False), the engine becomes mechanically unloaded. Under an unloaded condition, even a minor throttle opening could cause the engine to accelerate rapidly in fractions of a second. To prevent this "runaway" scenario, the logic utilizes an inverted Boolean signal and an “AND” gate: if the brake is OFF and the engine speed exceeds a much lower, conservative threshold of 2500 RPM, the safety shutdown is immediately triggered.

If either of these two scenarios occurs (processed through the logical “OR” gate), the system forces the Case Structure into its True state. In this state, the virtual accelerator demand is hardcoded to 0%, safely returning the engine to a stable idle state and preventing any dangerous over-revving.

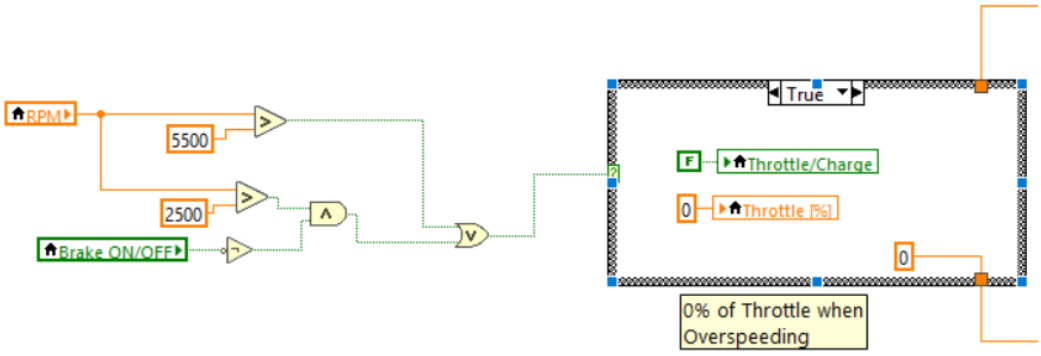


Figure 3.2.19-Safety Implementation in the Test Bench Control System

3.2.4 Real-Time Data Visualization and Thermodynamic Performance Computation

To effectively operate the engine test bench, a comprehensive Graphical User Interface (GUI), referred to as the Front Panel in LabVIEW, was developed. The primary objective of Software Visualization architecture is to provide the operator with intuitive, real-time control over the engine actuators while simultaneously displaying high-frequency data in a clear format.

Given the extensive number of acquired sensor channels, computed metrics, and control variables, displaying all information on a single screen would result in severe visual clutter and compromise the operator's situational awareness. To solve this, the interface is organized using a Tab Control structure, dividing the bench operations into dedicated, task-specific screens.

The default screen, illustrated in Figure 3.2.20, is the General Overview Tab, which serves as the primary operational dashboard during engine testing. It is logically divided into two distinct functional areas:

- Left Side (Control Panel): This section is dedicated to the direct management of the test bench. It features vertical slider controls for setting the target engine speed and the target throttle or charge percentage. It also houses critical safety and operational controls, including a highly visible Emergency Stop button, warning indicators (such as Low Oil Pressure), and the recording toggle switch (REC) to initiate TDMS data logging. Furthermore, the core mechanical outputs (Engine Speed, Torque, and Brake Power) are displayed here via large numerical indicators for immediate reference.
- Right Side (System Overview): The right half of the screen features a dynamic synoptic diagram (P&ID style) of the complete engine and test bench layout. This

graphical overview maps the physical architecture of the system, including: the engine block, turbocharger, intercooler, and coolant heat exchanger. Real-time numerical indicators for temperatures, pressures, and flow rates are superimposed directly on their corresponding physical locations within the fluid circuits, allowing the operator to instantly assess the engine's thermodynamic state.

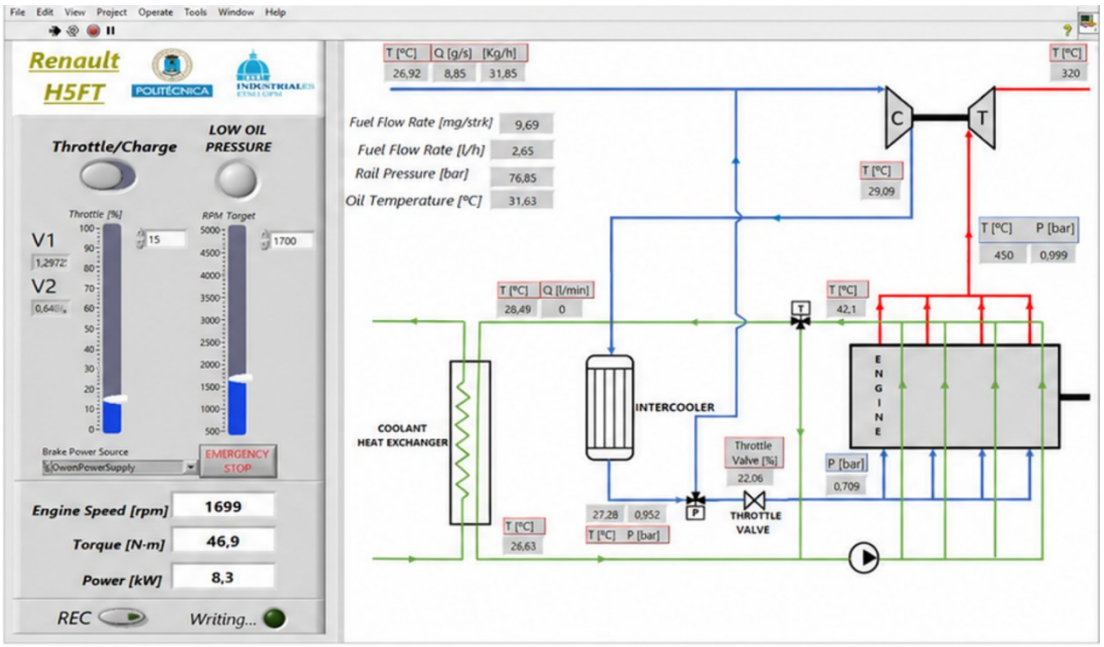


Figure 3.2.20-Main System Overview Tab

To keep the Main Tab streamlined, deeper analysis and system configuration are routed to secondary tabs, which the operator can navigate at any time:

- **Real-Time Graphs Tab:** This tab provides a fundamental visual history of the engine's mechanical output over time. It features three primary waveform charts: Engine Speed (RPM), Brake Torque, and Brake Power. Crucially, the RPM and Torque charts are configured as dual-plot graphs. They simultaneously display the actual measured value (the Process Variable) alongside the desired target value (the Setpoint). For the torque chart, this target curve is dynamically computed based on the operator's charge percentage command relative to the engine's maximum torque capacity. Superimposing these curves allows the operator to visually evaluate the PID controllers' tracking performance, immediately identifying overshoots, steady-state errors, or oscillatory behavior during transient maneuvers.
- **Energy Balance Tab:** This tab, shown in Figure 3.2.21, provides a comprehensive thermodynamic overview of the engine's energy distribution. It visually illustrates how the total chemical energy introduced by the fuel is partitioned throughout the system. The layout features:

1. A 3D Pie Chart that displays the instantaneous percentage breakdown of the energy flow at the current operating point;
2. A Stacked Area Chart (Fraction of Fuel Power vs. Time) that illustrates the continuous time-history of the energy distribution. It visually stacks the fractions of Mechanical Power, Flue Gases Power, Coolant Power, and Unaccounted Losses;
3. Three individual lower strip charts dedicated to tracking the absolute thermal power rejected to the Intercooler, the Coolant circuit, and the Flue Gases over time.

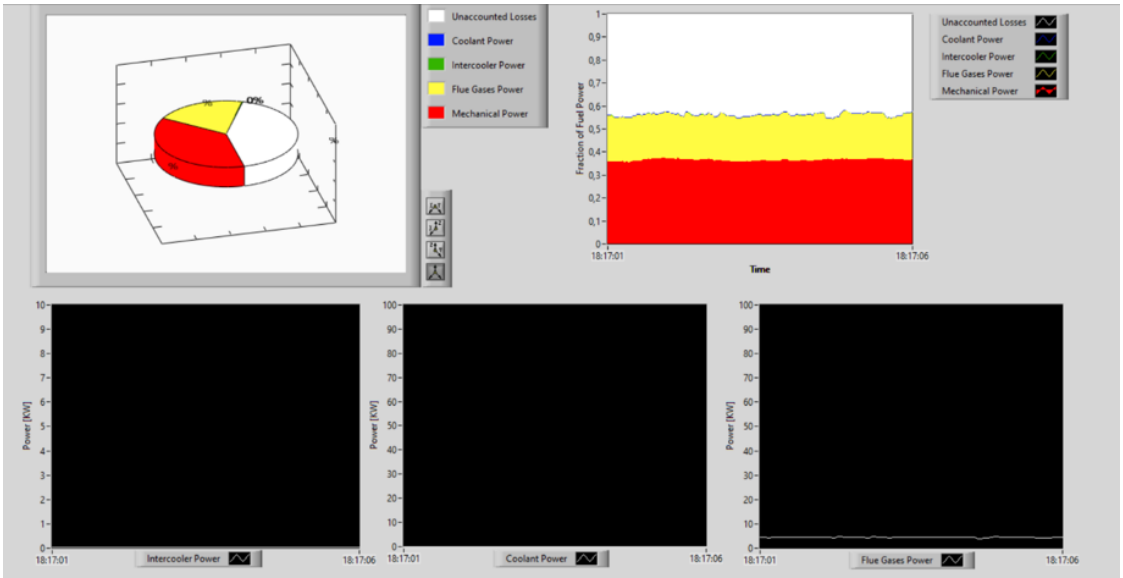


Figure 3.2.21-Energy Balance Tab

- **Performance Parameters Tab:** It is dedicated to the continuous graphical monitoring of derived thermodynamic and performance metrics. It contains four separate time-based strip charts shown in Figure 3.2.22:
    1. BSFC [g/kWh]: Tracks the Brake Specific Fuel Consumption, providing a real-time visualization of the engine's fuel economy.
    2. BMEP [bar]: Monitors the Brake Mean Effective Pressure, normalizing the torque output independent of engine displacement and speed.
    3. Volumetric Efficiency: A dual-plot chart that simultaneously tracks both the "Global" volumetric efficiency and the "Collector" (manifold) volumetric efficiency.
    4. Global Efficiency: Displays the overall thermal efficiency of the engine as a continuous fraction.

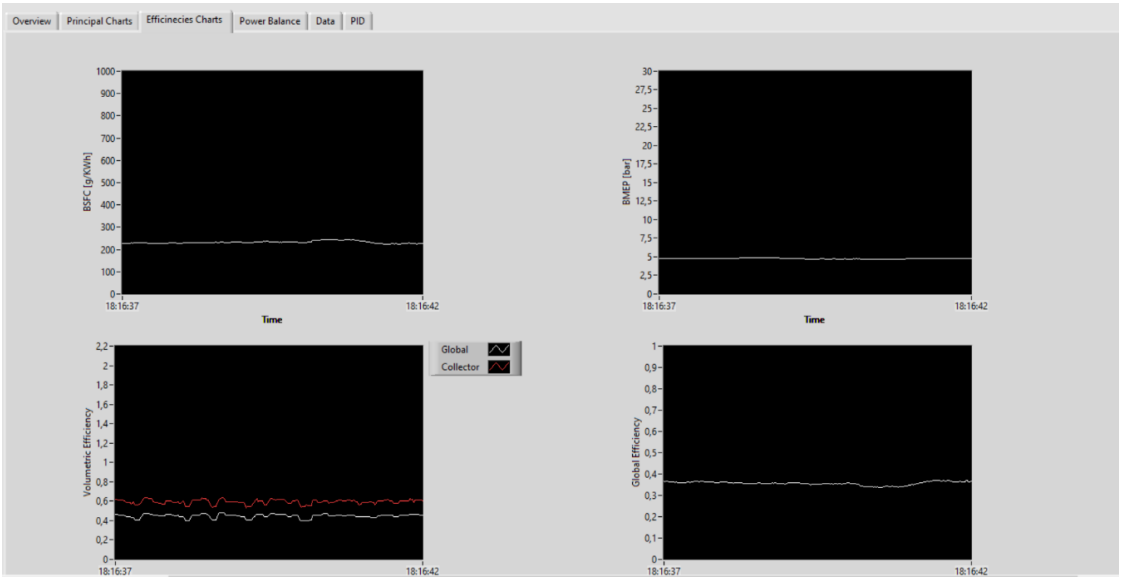


Figure 3.2.22-Performance Parameters Tab

- **Data Tab:** The tab (Figure 3.2.23) acts as a centralized numerical dashboard, aggregating all calculated thermodynamic properties and performance metrics into a clean, easily readable format without the distraction of moving graphs. The indicators are logically grouped into three horizontal sections:
    1. Fluid Properties and Combustion: Displays the Intake Air Density, Intake Manifold Air Density, the measured Air-to-Fuel Ratio (AFR), and the computed specific heat capacity of the flue gases;
    2. Efficiencies and Output: Provides instantaneous digital readouts for Global Efficiency, Global and Collector Volumetric Efficiencies, BSFC, and BMEP.
    3. Power Breakdown: Shows the absolute instantaneous values (in kW) for Fuel Power (the total input energy rate), Flue Gases Power, Intercooler Power, and Coolant Power.

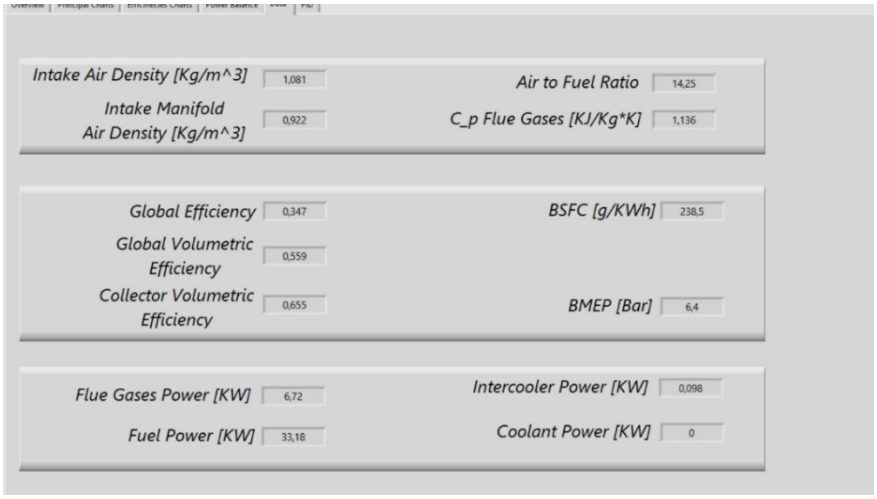


Figure 3.2.23-Global Data Tab

- **PID Settings Tab:** A crucial configuration interface that allows the operator to manually adjust the Proportional, Integral, and Derivative gains for both the dynamometer voltage control and the electronic throttle actuator, enabling on-the-fly tuning during bench calibration (Figure 3.2.24).

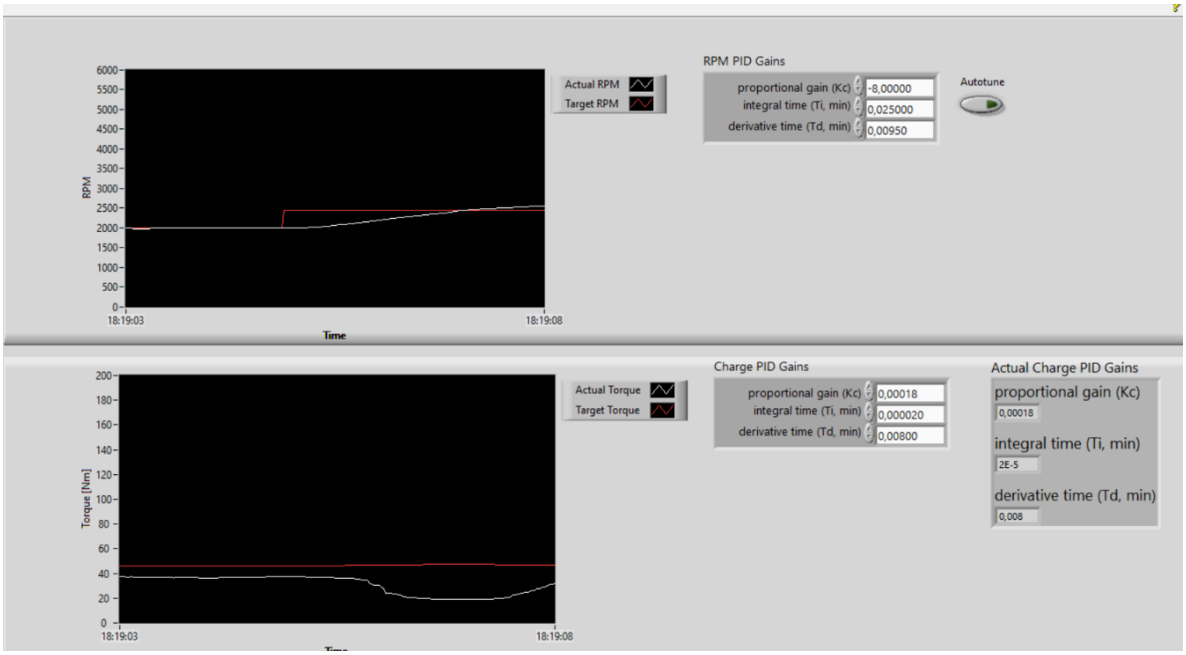


Figure 3.2.24-PID Control Tab

To populate the Energy Balance and Performance Parameters tabs, the software dynamically calculates the individual thermal power streams.

Input Fuel Power: The total available chemical power entering the system is determined by multiplying the fuel mass flow rate by the Lower Heating Value of the fuel (LHV). The Lower Heating Value of the fuel was set to a constant value of 43.5 MJ/kg. This parameter is in accordance with standard automotive engineering references, which report a typical lower heating value ranging between 43.0 and 44.0 MJ/kg for commercial unleaded gasoline complying with the EN 228 standard [16]. Equation (3.6) illustrates how the input fuel power is calculated.

$$\dot{Q}_{\text{fuel}} = \left(\frac{\dot{V}_{\text{fuel}} \cdot 745}{3600}\right) \cdot 43.5 \tag{3.6}$$

Where:

- $\dot{Q}_{\text{fuel}}$ is the total input fuel chemical power in kW.
- $\dot{V}_{\text{fuel}}$ is the measured volumetric fuel flow rate in L/h.
- ρ_{fuel} is the fuel density, set to 745 g/L. This nominal value complies with the European standard EN 228 for commercial unleaded automotive gasoline (which defines

an allowable density range of 720.0–775.0 kg/m^3 at 15°C) and is in agreement with standard automotive engineering reference literature [16].

Intercooler Heat Rejection: The rate of heat extracted from the turbocharged intake air by the intercooler is calculated (Equation (3.7)) using the intake air mass flow and the temperature drop across the heat exchanger.

$$\dot{Q}_{\text{int}} = \left(\frac{\dot{m}_{\text{air}}}{1000}\right) \cdot c_{p,\text{air}} \cdot \left(T_{\text{out,comp}} - T_{\text{out,int}}\right) \tag{3.7}$$

Where:

- $\dot{Q}_{\text{int}}$ is the thermal power rejected by the intercooler in kW.
- $\dot{m}_{\text{air}}$ is the intake air mass flow rate in g/s (scaled by 1000 to convert it to kg/s).
- $c_{p,\text{air}}$ is the specific heat capacity of dry air at constant pressure, taken as a standard constant 1.005 kJ/(kg*K).
- $T_{\text{out,comp}}$ is the air temperature at the compressor outlet [°C].
- $T_{\text{out,int}}$ is the cooled air temperature at the intercooler outlet [°C].

Dynamic Specific Heat and Flue Gases Power: Because exhaust gases operate across extreme thermal gradients (200–850 °C), the specific heat capacity cannot be assumed constant. The LabVIEW block diagram dynamically computes at each loop cycle using the 3rd-degree polynomial equation (3.8) based on the absolute exhaust gas temperature:

$$c_{p,\text{fg}} = a + bT + cT^2 + dT^3 \tag{3.8}$$

Where the calibrated coefficients applied in the software are $a = 999.4$, $b = 0.0163$, $c = 0.000211$, and $d = -4.96 \cdot 10^{-8}$.

The specific coefficients applied were derived through regression of standard thermodynamic tables for gasoline combustion products at typical equivalence ratios [16].

Once the specific heat capacity is determined, the thermal power expelled through the exhaust system is computed by combining the intake air and fuel mass flow rates and evaluating the thermal gradient against the ambient temperature (Equation (3.9)).

$$\dot{Q}_{\text{fg}} = \left(\frac{\dot{m}_{\text{air}} + \dot{m}_{\text{fuel}}}{1000}\right) \cdot c_{p,\text{fg}} \cdot \left(T_{\text{pre_turb}} - T_{\text{amb}}\right) \tag{3.9}$$

Where:

- $\dot{Q}_{\text{fg}}$ is the sensible thermal power carried away by the flue gases in [kW].
- $\dot{m}_{\text{air}}$ is the intake air mass flow rate in [g/s].
- $\dot{m}_{\text{fuel}}$ is the fuel mass flow rate in [g/s], computed from the volumetric sensor.
- 1000 converts the total exhaust mass flow ($\dot{m}_{\text{air}} + \dot{m}_{\text{fuel}}$) from g/s to kg/s.

- $c_{p,\mathrm{fg}}$ $[\mathrm{kJ}/(\mathrm{kg}\cdot\mathrm{K})]$ is the instantaneous dynamic specific heat capacity calculated above.
- $T_{\mathrm{pre_turb}}$ is the measured exhaust gas temperature upstream of the turbocharger turbine [°C].
- T_{amb} is the reference ambient test cell temperature [°C].

Coolant Power and Unaccounted Losses: The thermal power rejected to the engine block coolant circuit is evaluated using the coolant flow rate, its specific heat capacity, and the temperature gradient between the inlet and outlet of the engine (Equation (3.10)).

$$\dot{Q}_{\mathrm{coolant}} = \dot{m}_{\mathrm{coolant}} \cdot c_{p,\mathrm{coolant}} \cdot \left(T_{\mathrm{out,coolant}} - T_{\mathrm{in,coolant}}\right) \tag{3.10}$$

Where:

- $\dot{Q}_{\mathrm{coolant}}$ is the thermal power rejected to the engine coolant circuit [kW].
- $\dot{m}_{\mathrm{coolant}}$ is the mass flow rate of the coolant mixture [kg/s], derived from the volumetric flowmeter $\dot{V}_{\mathrm{coolant}}$ and the mixture density.
- $c_{p,\mathrm{coolant}}$ is the specific heat capacity of the water-glycol coolant solution [kJ/(kg · K)], set in the software to 3.6 kJ/(kg · K).
- $T_{\mathrm{out,coolant}}$ is the hot coolant temperature leaving the engine block [°C].
- $T_{\mathrm{in,coolant}}$ is the cold coolant temperature returning from the heat exchanger to the engine inlet [°C].

Finally, to complete the thermodynamic balance and close the pie chart visualization arrays, the software computes the Unaccounted Losses, which consist of unmeasured radiant heat transfer and mechanical friction, and it is given by the difference between the power provided by the fuel and the sum of the fractions of the power described in Equation (3.11).

$$\dot{Q}_{\mathrm{losses}} = \dot{Q}_{\mathrm{fuel}} - \left(P_{\mathrm{mech}} + \dot{Q}_{\mathrm{coolant}} + \dot{Q}_{\mathrm{fg}}\right) \tag{3.11}$$

Mechanical Power (P_{mech}): The instantaneous mechanical work delivered to the dynamometer shaft is computed from the rotational speed and the measured load, as it is shown in Equation (3.12).

$$P_{\mathrm{mech}} = \frac{2\pi \cdot N \cdot \tau}{60000} \tag{3.12}$$

Where:

- P_{mech} is the brake mechanical power [kW].
- N is the engine rotational speed [RPM].
- τ is the brake torque measured at the dynamometer load cell [N · m].

- $2\pi/60$ converts the rotational speed from revolutions per minute (RPM) to angular velocity (rad/s).
- 1000 (combined as the 60000 divisor) converts the resulting power from Watts [W] to kiloWatts [kW].

Fuel Mass Flow and BSFC: The fuel delivery system measures the instantaneous consumption as a volumetric flow rate. To evaluate fuel economy, the software computes the mass flow rate and normalizes it against the generated mechanical power (Equation (3.13)).

$$BSFC = \frac{\dot{V}_{\text{fuel}} \cdot \rho_{\text{fuel}}}{P_{\text{mech}}} \tag{3.13}$$

Where:

- $BSFC$ is the Brake Specific Fuel Consumption [g/kWh].
- $\dot{V}_{\text{fuel}}$ is the volumetric fuel flow rate [L/h].
- ρ_{fuel} is the nominal gasoline density, set in the LabVIEW block diagram to 745 g/L (or 0.745 kg/L).
- P_{mech} is the instantaneous brake power [kW]

Volumetric Efficiencies: The volumetric efficiency quantifies the breathing efficiency of the internal combustion engine relative to its theoretical displacement volume. The software evaluates two distinct volumetric metrics: the Global Volumetric Efficiency (referenced to ambient intake air density ρ_{amb}) and the Collector Volumetric Efficiency (referenced to intake manifold air density ρ_{man}) through Equation (3.14).

$$\eta_{\text{vol}} = \frac{\dot{m}_{\text{air}}/1000}{\rho \cdot V_d \cdot \left(\frac{N}{120}\right)} \tag{3.14}$$

Where:

- η_{vol} is the volumetric efficiency [dimensionless fraction, $0 - 1$].
- $\dot{m}_{\text{air}}$ is the measured intake air mass flow rate [g/s] (divided by 1000 to obtain [kg/s]).
- ρ is the reference air density $\left[\text{kg/m}^3\right]$, taking either the ambient density ρ_{amb} (for global efficiency) or the manifold density ρ_{man} (for collector efficiency).
- V_d is the total engine displacement volume, equal to 0.001197 m^3 (1197 cm^3).
- N is the engine rotational speed [RPM].

- 120 is the 4-stroke cycle conversion factor: $120 = 2 \cdot 60$, where 2 accounts for the two crankshaft revolutions required per intake stroke in a four-stroke cycle, and 60 converts minutes to seconds to match the mass flow rate time base.

Both reference densities (ρ_{amb} or ρ_{man}) are continuously computed in real time using the ideal gas law shown in Equation (3.15).

$$\rho = \frac{p \cdot 100}{R_a \cdot (T + 273.15)} \tag{3.15}$$

Where:

- ρ is the calculated air density [kg/m^3] (ρ_{amb} or ρ_{man}).
- p is the measured absolute pressure [bar]. The multiplication factor of 100 converts the pressure measurement from bar to kPa.
- T is the measured temperature [˚C]. The addition of 273.15 converts the reading to Kelvin.
- R_a is the specific gas constant for dry air, programmed as 0.28705 kJ/(kg · K).

Depending on the targeted efficiency calculation, the inputs are routed accordingly: for the ambient density, p and T correspond to the ambient room pressure and temperature; for the intake manifold density, the inputs are drawn from the manifold absolute pressure sensor and the intercooler outlet temperature sensor.

Global Efficiency (η_{global}): The overall thermal efficiency reflects the first-law thermodynamic performance, defined as the ratio of useful mechanical output to the total chemical energy introduced into the combustion chambers (Equation (3.16)).

$$\eta_{\text{global}} = \frac{P_{\text{mech}}}{\dot{Q}_{\text{fuel}}} \tag{3.16}$$

Where:

- η_{global} is the overall thermal efficiency [dimensionless fraction].
- P_{mech} is the instantaneous brake mechanical power delivered to the dynamometer [kW].
- $\dot{Q}_{\text{fuel}}$ is the total input fuel thermal power [kW].

4 Tests and Results

This chapter presents the experimental validation of the automated dynamometer test bench and the subsequent thermodynamic characterization of the engine. The testing campaign is divided into two primary phases. The first phase focuses on the dynamic performance of the newly implemented control system, evaluating the setpoint tracking and disturbance rejection capabilities of both the dynamometer brake and the charge controllers. The second phase leverages this stable testing environment to conduct a comprehensive macro-parameter analysis of the powertrain. This includes mapping full-load performance, evaluating the global energy balance, analyzing volumetric-efficiency dynamics, and determining Brake Specific Fuel Consumption (BSFC) across the engine's operational envelope.

4.1 Dynamometer Brake Control Tests

To comprehensively evaluate the robustness, stability, and dynamic response of the brake loop control system, two complementary experimental campaigns were conducted on the test bench:

- **Setpoint Tracking Performance (Constant Throttle, Variable RPM):** The engine load was maintained at fixed throttle positions while commanding step variations in the target rotational speed. This test assesses the tracking capability of the control algorithm, quantifying transient metrics such as raising time, settling time, and the tolerance band under varying operating conditions.
- **Load Disturbance Rejection (Constant RPM, Variable Throttle):** The target rotational speed was held constant while introducing step and ramp variations in the throttle demand. This configuration tests the controller’s disturbance-rejection capacity, evaluating its ability to counteract abrupt variations in engine indicated torque by modulating the dynamometer excitation voltage without allowing consistent speed drift or persistent deviations.

4.1.1 Engine Speed Step Response Tests

In the first test series, the accelerator command was locked at fixed values (20%, 40%, and 60% throttle), and successive 800 RPM step increments and decrements were introduced between 1800 RPM, 2600 RPM, and 3400 RPM. The settling time was recorded as the

elapsed time from the command initiation until the engine speed entered and remained within a strict stability band of ±15 RPM around the target value.

Table 4.1 reports the settling times measured across the complete matrix of step transitions and engine loads.

Transition (RPM)	Settling Time @ 20% Throttle	Settling Time @ 40% Throttle	Settling Time @ 60% Throttle
1800 to 2600	5.00 s	5.60 s	5.30 s
2600 to 3400	6.80 s	4.70 s	3.50 s
3400 to 2600	4.70 s	5.00 s	3.60 s
2600 to 1800	5.15 s	6.10 s	5.30 s

Table 4.1-Measured Settling Times across Dynamic Engine Speed Transitions at Various Throttle Positions

To visually illustrate the system's dynamic behavior and highlight the operational extremes, four representative test cases were selected from the experimental matrix. The measured response times show robust closed-loop stability across most of the speed envelope, with settling times generally ranging from 3.5 s to 6.8 s. These figures represent a highly satisfactory dynamic performance considering the combined mechanical inertia of the engine-dynamometer assembly and the electromagnetic latency of the brake.

The dynamic response depends heavily on the available engine torque, which is directly dictated by throttle position.

- In the Worst-Case Scenario (Figure 4.1.1), the transition from 2600 to 3400 RPM at 20% throttle yielded the longest settling time (6.80 s). At such a low load, the engine struggles to overcome the mechanical inertia required to accelerate, resulting in a sluggish, prolonged climb to the target setpoint.

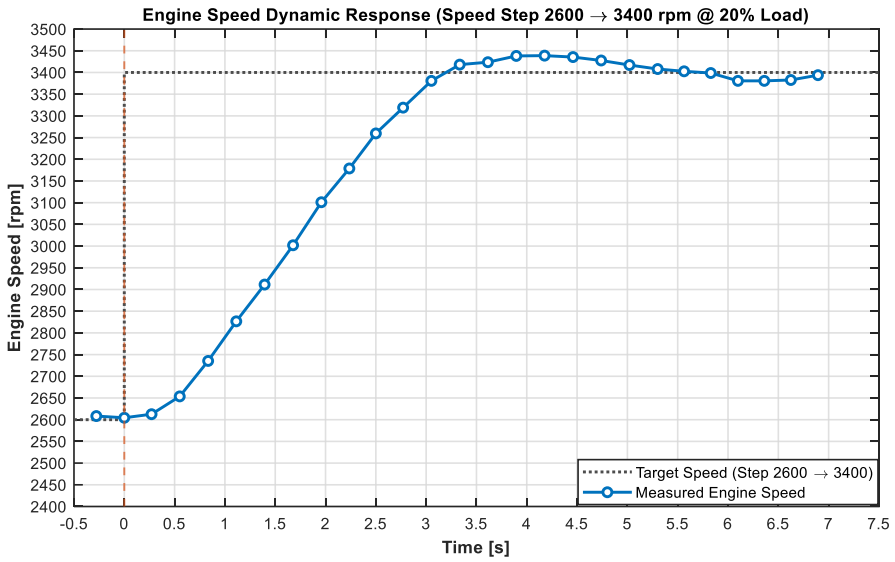


Figure 4.1.1-Engine Speed Step Response: Transition from 2600 to 3400 RPM at 20% Throttle (Longest Settling Time)

- In the Best-Case Scenario (Figure 4.1.2): Conversely, the exact same speed transition (2600 to 3400 RPM) executed at 60% throttle produced the fastest settling time (3.50 s). At this higher load, the increased thermodynamic torque allows the engine to rapidly overpower the dynamometer's resistance, bringing the system to dynamic equilibrium almost twice as fast.

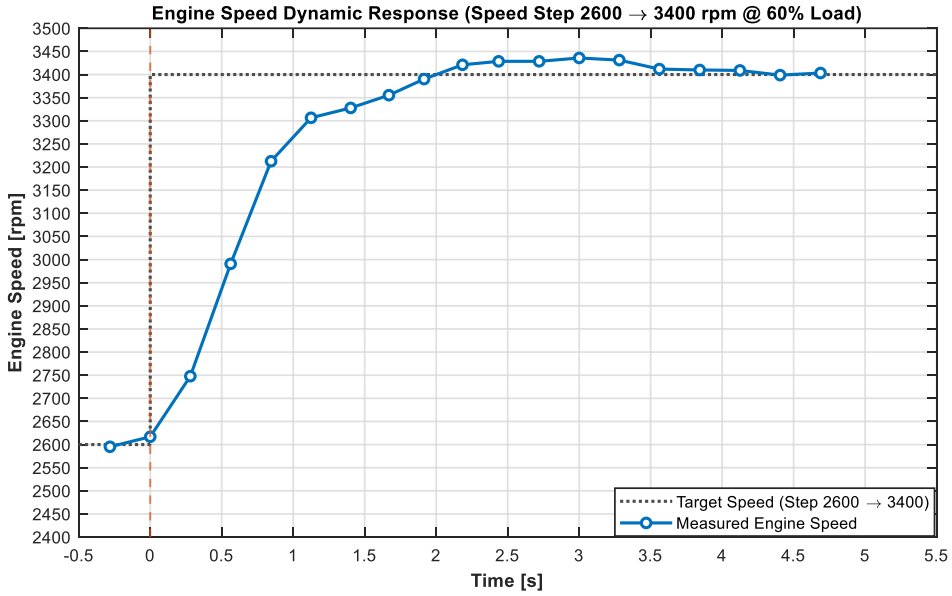


Figure 4.1.2-Engine Speed Step Response: Transition from 2600 to 3400 RPM at 60% Throttle (Shortest Settling Time)

- While the absolute settling times are generally acceptable, a closer inspection of the mid-load transitions reveals a specific non-linearity in the system's response. Figure 4.1.3 depicts the step-up (1800 to 2600 RPM) and step-down (3400 to 2600 RPM)

transitions at a constant 40% throttle. Although these transitions settle within 5.60 s and 5.00 s respectively, the speed trajectories exhibit noticeable micro-oscillations as they converge upon the target. Rather than locking smoothly into the setpoint, the engine speed shakes marginally around the threshold before fully stabilizing within the ±15 RPM tolerance band. This localized instability, which appears specific at 2600 RPM operating region at 40% throttle, is likely attributable to the intrinsic non-linearities of the internal combustion engine which momentarily challenge the fixed proportional and derivative gains of the PID controller. Despite this slight jitter, the controller successfully prevents runaway oscillations and ultimately secures the set-point.

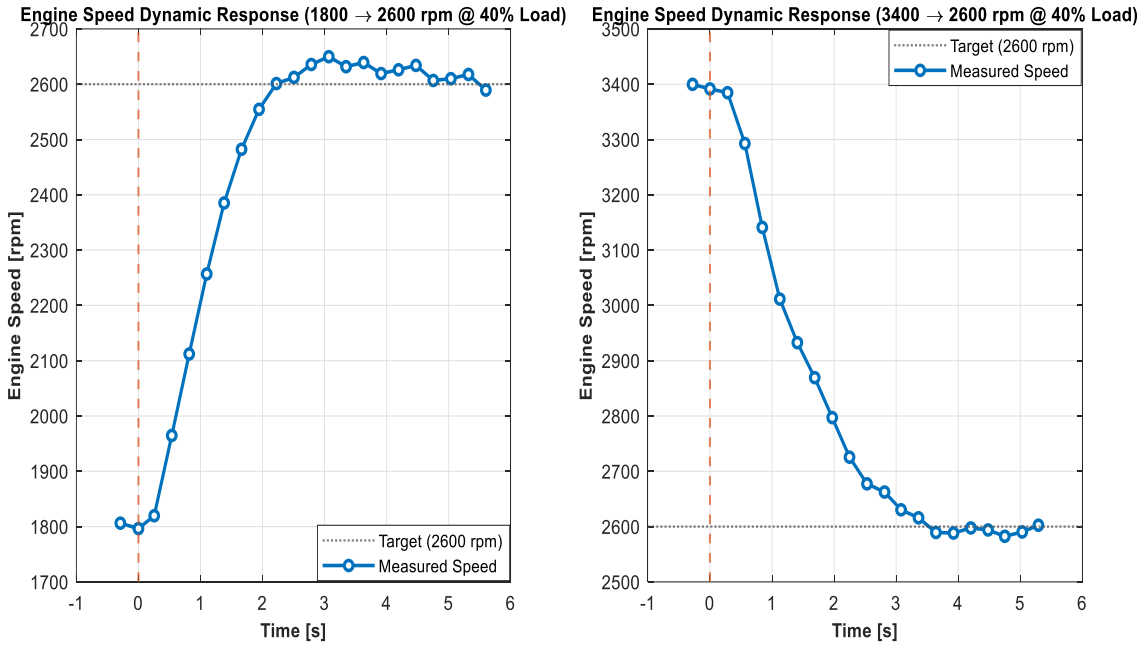


Figure 4.1.3-Engine Speed Step Responses at 40% Throttle: Acceleration from 1800 to 2600 RPM (Left) and Deceleration from 3400 to 2600 RPM (Right)

4.1.2 Load Disturbance Rejection Tests

The second phase of the dynamic validation assessed the PID controller's disturbance rejection capabilities. In these tests, the target engine speed was held constant (at 1800, 2600, and 3400 RPM) while sudden step changes in the accelerator throttle were introduced (20% to 40%, 40% to 60%, and their respective step-downs).

This scenario is particularly challenging for the control system: as the throttle instantly increases the engine's torque output, the PID controller must rapidly detect the positive speed error and increase the dynamometer excitation voltage to absorb the excess mechanical

power and force the engine back to the target setpoint. The settling time was again recorded based on a ±15 RPM error band.

Table 4.2 summarizes the measured settling times for the load disturbance tests.

Throttle Transition	Settling Time @ 1800 RPM	Settling Time @ 2600 RPM	Settling Time @ 3400 RPM
20% to 40%	6.90 s	5.00 s	4.70 s
40% to 60%	4.80 s	6.40 s	2.80 s
60% to 40%	5.10 s	3.90 s	3.40 s
40% to 20%	5.30 s	4.60 s	5.30 s

Table 4.2-Measured Settling Times for Throttle Step Changes

The system successfully rejects torque disturbances across the testing matrix, continually returning to the target setpoint. However, the transient waveforms reveal varying degrees of controller effort depending on the specific engine operating point. To illustrate these dynamics, four characteristic responses are analyzed in detail:

- The Worst-Case Scenario (Figure 4.1.4): The transition from 20% to 40% throttle at 1800 RPM produced the longest stabilization time (6.90 s). At this low speed and low throttle state, the sudden torque increase causes a significant initial speed spike (reaching approximately 1960 RPM). Because the baseline rotational momentum is low, the controller requires more time to build sufficient electromagnetic braking force in the stator coils to clamp the acceleration and draw the speed back down to the 1800 RPM target.

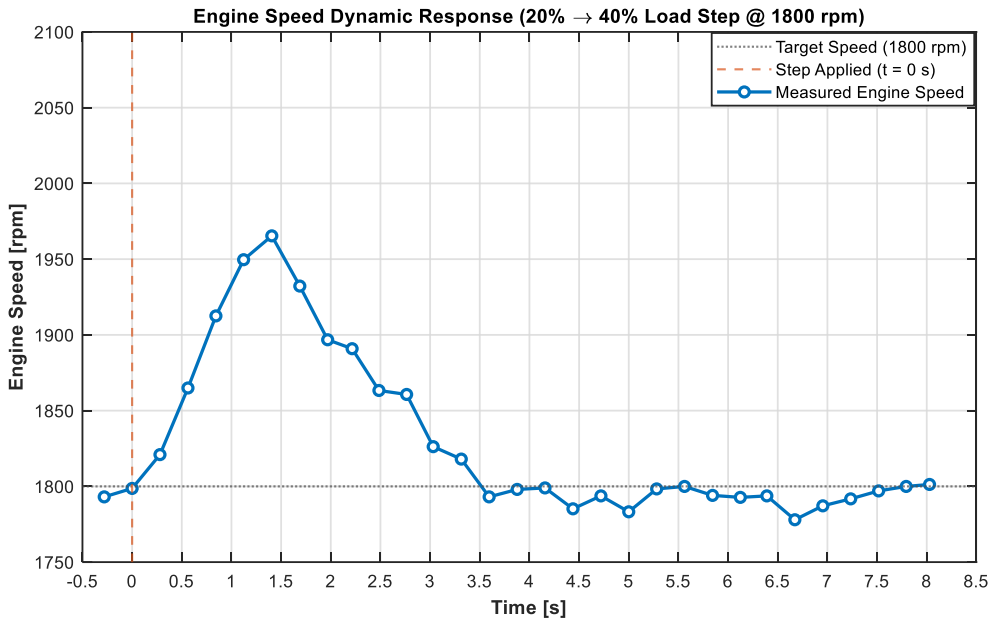


Figure 4.1.4-Load Disturbance Response: Throttle Step from 20% to 40% at 1800 RPM (Longest Settling Time)

- The Best-Case Scenario (Figure 4.1.5): Conversely, the step from 40% to 60% throttle at 3400 RPM yielded the fastest recovery (2.80 s). At high engine speeds, the eddy-current dynamometer operates in a highly efficient absorption range. Although the peak is higher than in the previous case, the PID controller quickly counteracts the torque increase, clamping the initial spike efficiently.

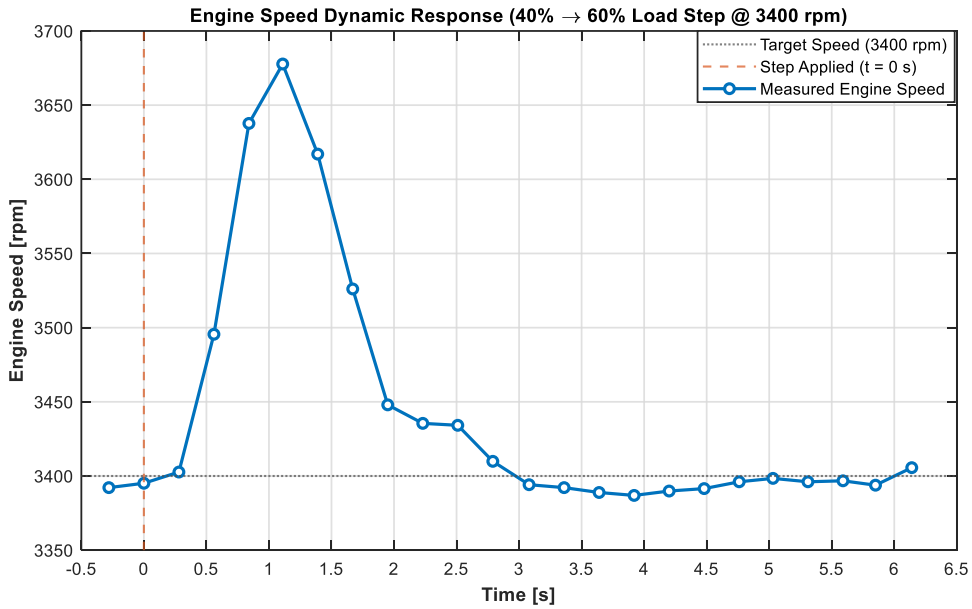


Figure 4.1.5-Load Disturbance Response: Throttle Step from 40% to 60% at 3400 RPM (Fastest Settling Time)

- Dual-Peak Response (Figure 4.1.6): The transition from 40% to 60% throttle at 1800 RPM (settling in 4.80 s) exhibits an unusual dual-peak trajectory. After the initial load step, the speed rises, dips slightly, and then peaks a second time (higher than the first) before finally decaying toward the setpoint. This two-stage transient is most likely attributable to turbocharger dynamics and the inherent boost-pressure latency. The initial peak corresponds to the instantaneous increase in airflow upon throttle opening, which the controller begins to counteract; however, once the turbocharger overcomes its lag and fully spools up, it delivers another stronger torque spike. Coupled with the electromagnetic time constant of the dynamometer windings, this sudden torque excess momentarily outpaces the brake's resistive response, causing the second speed overshoot before the PID integral action accumulates sufficient effort to restore equilibrium.

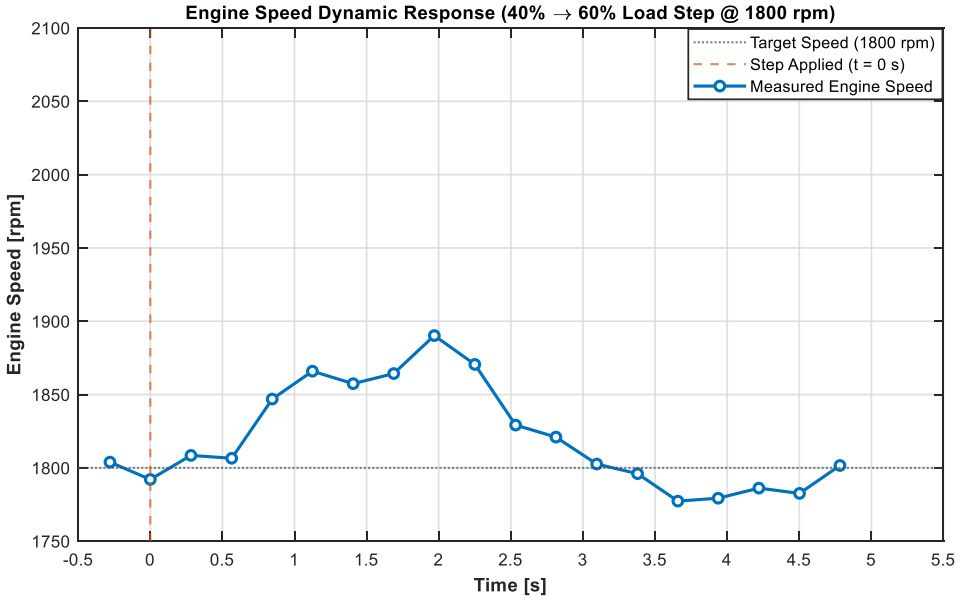


Figure 4.1.6-Load Disturbance Response: Throttle Step from 40% to 60% at 1800 RPM Exhibiting Dual-Peak Transient Behavior

- Late-Stage Instability (Figure 4.1.7): The step from 40% to 60% throttle at 2600 RPM took 6.40 s to settle due to localized instability at the end of the transient. Following a massive initial spike (reaching nearly 2850 RPM), the speed exhibits "shaking" or under-damped micro-oscillations around the 2600 RPM mark. This indicates that the fixed proportional and derivative gains of the PID are slightly aggressive for the steep torque gradient present at this specific mid-range operating point, causing the system to overcorrect marginally before finally locking into the tolerance band.

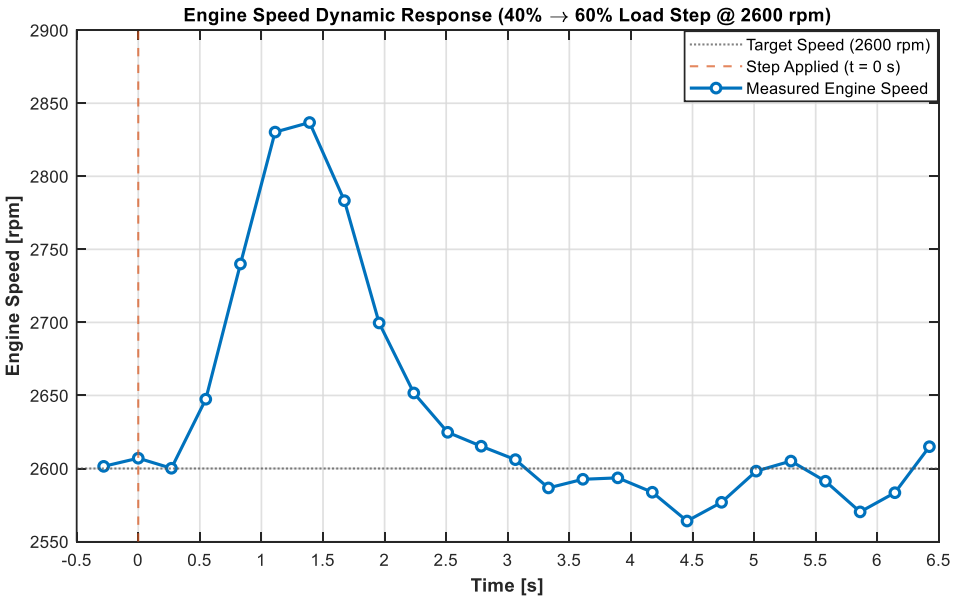


Figure 4.1.7-Load Disturbance Response: Throttle Step from 40% to 60% at 2600 RPM Showing Convergence Oscillations

4.2 Charge Control Tests

In order to investigate the dynamic tracking performance and stability margins of the secondary PID controller, an experimental validation campaign was conducted on the engine test bench. Here, the controller modulates the virtual accelerator input fed to the ECU to achieve the commanded charge level, while the primary dynamometer loop keeps engine speed fixed. The target engine speed was clamped at predefined intervals of 500 RPM, spanning from 1500 RPM up to a maximum of 4500 RPM. At each of these steady-state speed plateaus, step changes in the target charge were commanded by sequentially incrementing and decrementing the load between 25%, 50%, and 75% thresholds.

As detailed in the test bench design chapter, this controller employs an RPM-dependent Gain-Scheduling strategy for the integral time to handle the engine's non-linear torque response across the speed range. The effects of this adaptive tuning are clearly visible in the transient responses over the operating map.

To illustrate the controller's behavior, three distinct operational scenarios are presented:

- Low-Speed Regime (1500 RPM | 25% to 50% Charge): At low engine speeds (Figure 4.2.1), the system exhibits its most challenging dynamic behavior. As shown in the first graph, the transition takes much longer to settle (around 14 seconds), and the measured torque (blue line) shows a period of high-frequency oscillation, or "shaking," before stabilizing. This behavior is a direct consequence of the inherent

instability of the engine speed in this low-RPM regime. As the graph shows, rotational speed is not perfectly constant; these localized RPM fluctuations, likely driven by discrete cylinder combustion pulses at such low speeds, propagate directly into significant torque variations. Because the integral time in this regime (< 1500 RPM) was deliberately tuned to be less aggressive to prevent runaway instability caused by these speed-induced torque ripples, the controller inherently sacrifices some tracking speed. The initial "shaking" reflects the controller carefully modulating the accelerator signal to navigate this unstable zone before securely locking onto the 50% target.

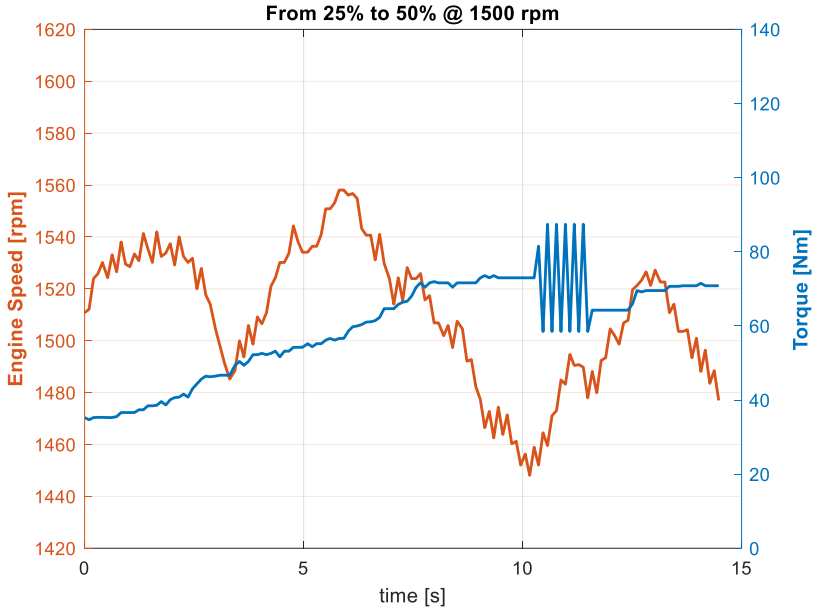


Figure 4.2.1-Charge Control Transient Responses: Target Torque Step Tracking at 1500 RPM

- Mid-Speed Regime (2500 RPM | 50% to 75% Charge): The second graph (Figure 4.2.2) demonstrates the system's optimal performance window. Operating at 2500 RPM, the controller is fully within the high-speed gain schedule (> 2200 RPM), where a more aggressive integral action is permitted. The torque responds rapidly and cleanly to the throttle step, converging smoothly to the 75% target with minimal delay and practically no localized oscillations.

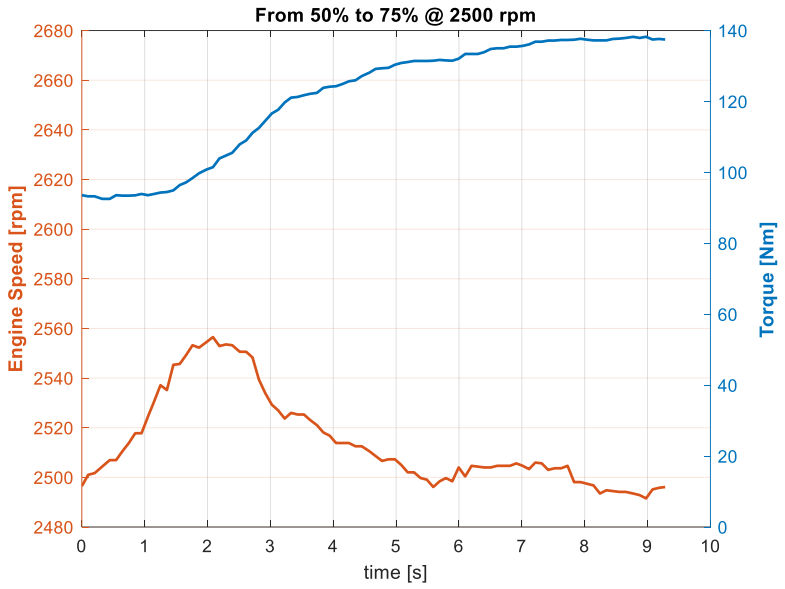


Figure 4.2.2-Charge Control Transient Responses: Target Torque Step Tracking at 2500 RPM

- High-Speed Regime (3500 RPM | 50% to 75% Charge): The third graph (Figure 4.2.3) shows the response at an elevated engine speed. While still using the high-speed integral parameters, the system takes longer to reach the target than in the mid-speed test. This slower convergence is not an indicator of control instability, but rather stems from the engine's inherent performance characteristics at elevated speeds. At 3500 RPM, a 25% step in target torque represents a substantially larger absolute power differential than the same percentage step at lower speeds. Consequently, the engine's thermodynamic system inherently requires more time to develop this additional load. Nevertheless, the system reaches the 75% charge target stably, without the shaking observed in the low-speed regime.

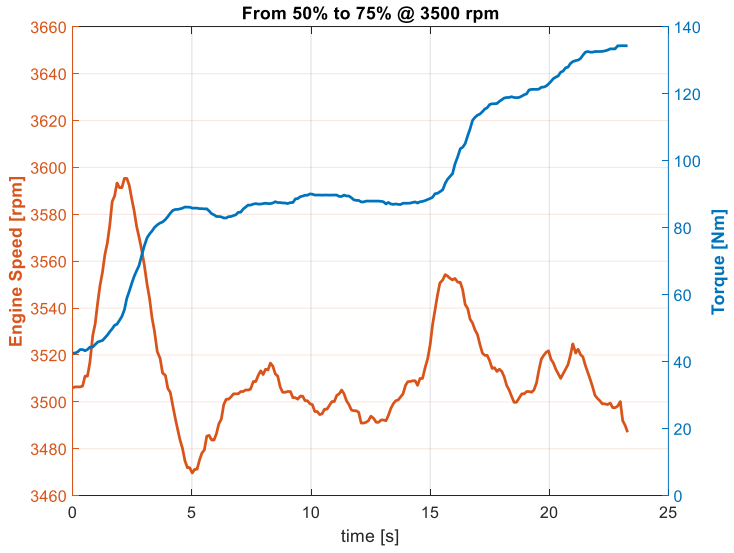


Figure 4.2.3-Charge Control Transient Responses: Target Torque Step Tracking at 3500 RPM

Overall, the step-response tests confirm that the decoupled control strategy and the RPM-dependent gain scheduling are effective. The charge controller successfully modulates the throttle to hit torque targets across the entire map. While low-speed transitions inherently suffer from minor transient jitters, the scheduled PID gains prevent this from escalating into continuous oscillation, ensuring the engine speed controller (dynamometer) remains undisturbed.

4.3 Engine Performance Map

Another fundamental phase of the experimental campaign was dedicated to characterizing the engine's full-load performance by mapping the maximum torque output across its operational speed range. The steady-state data acquisition was performed at discrete speed intervals, starting from 1500 RPM up to a maximum of 4500 RPM, utilizing precise increments of 250 RPM.

To ensure absolute reliability in the torque estimations and mitigate the impact of instantaneous mechanical transients, a strict, sequential testing procedure was enforced at each 250 RPM step. First, the engine speed was clamped at the targeted plateau by the primary dynamometer PID loop. Next, the virtual accelerator demand was progressively and smoothly increased until reaching 100%. The system was then left unmodified for a brief period to fully stabilize under this maximum load. Only after stabilization was confirmed, a continuous 15-second data acquisition window was initiated. The definitive torque value for that specific RPM was subsequently computed as the mathematical average of the data collected during these 15 seconds.

However, a critical thermal limitation emerged during this procedure at higher rotational speeds. For tests exceeding 3500 RPM, maintaining a 100% load for the full 15-second window caused significant overheating of the air at the intake manifold. If the air temperature at the intercooler outlet exceeded a hardware protection threshold of around 60 °C, the Engine Control Unit would proactively intervene, cutting power to protect the powertrain. To circumvent this constraint and prevent the ECU's thermal derating from corrupting the performance data, the averaging strategy was dynamically adapted for the 3500–4500 RPM range: data extraction still commenced immediately after torque and speed stabilization, but was aborted exactly before the intercooler outlet temperature reached the 55 °C limit, yielding a slightly narrower averaging window.

The resulting full-load torque profile is illustrated in Figure 4.3.1. The plotted data points represent the experimentally averaged torque at each 250 RPM increment.

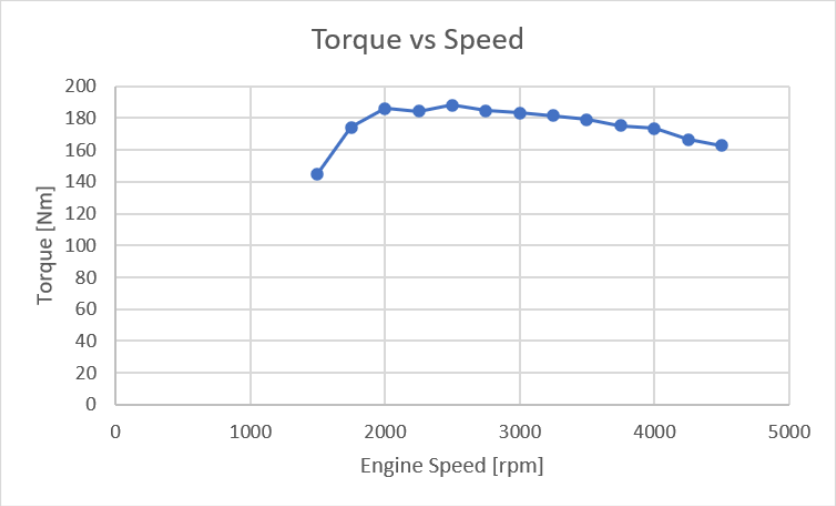


Figure 4.3.1-Full Load Engine Performance Map (Torque vs. Engine Speed)

As depicted in the graph, the engine demonstrates a remarkably robust and broad mid-range power delivery. The maximum experimental torque recorded during the campaign was 188 Nm, achieved at 2500 RPM. This empirical result is highly consistent with the engine's official nominal specifications, which declare a peak torque of 190 Nm. Although the nominal data indicates this peak should occur at 2000 RPM rather than 2500 RPM, this shift does not indicate anomalous engine behavior. Instead, it can be attributed primarily to minor measurement variability. As observed in the plot, the engine's torque delivery is almost flat and constant between 2000 RPM and 3000 RPM; the measured torque at 2000 RPM is already extremely high and nearly identical to the absolute peak. Furthermore, a minor localized downward dip is visible at 2250 RPM. This negligible fluctuation confirms that across such a broad and flat torque plateau, the exact singular point of "maximum" torque is highly susceptible to minor environmental or measurement artifacts. Following this extended plateau, the torque output exhibits the expected gradual decline as the engine speed increases toward 4500 RPM, due to engine efficiency limits and the thermal constraints previously discussed.

Following the steady-state torque assessment, the corresponding engine power was analytically derived for each of the tested 250 RPM increments. The resulting full-load power curve is presented in Figure 4.3.2.

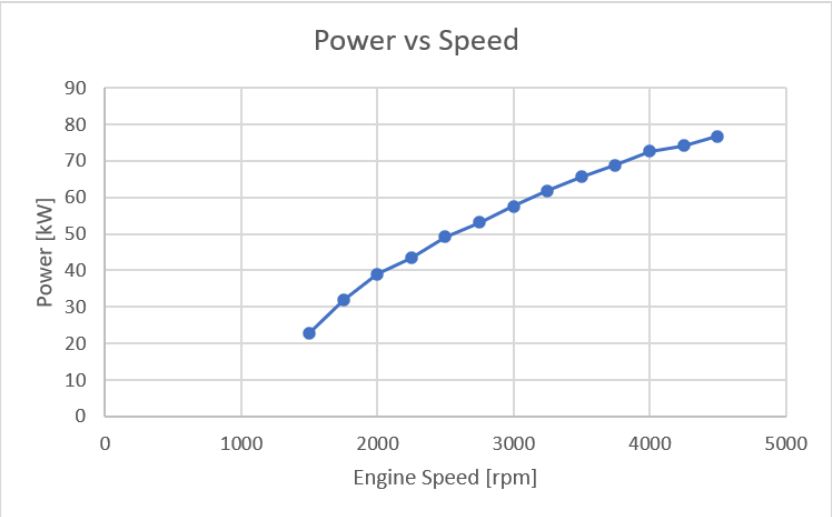


Figure 4.3.2-Full Load Engine Power Profile

As illustrated in the graph, power output climbs progressively with engine speed, reaching a maximum recorded value of approximately 77 kW at 4500 RPM. According to the manufacturer's nominal specifications, the engine is rated for a peak power of 88 kW at 4900 RPM [4]. However, the experimental campaign was deliberately halted at 4500 RPM, meaning the theoretical peak and the subsequent curve drop-off could not be empirically validated. This truncation of the testing matrix was enforced strictly for safety and equipment preservation due to thermal bottlenecks. Operating at these elevated rotational speeds and loads caused the post-intercooler air temperatures to surge rapidly.

This performance deficit strongly suggests that the Engine Control Unit (ECU) was already actively intervening to protect the powertrain. Because the intake air temperature was approaching the critical 60 °C hardware threshold, it is highly probable that the ECU initiated to cut power by retarding ignition timing or limiting boost pressure to compensate for the excessively hot intake charge. Consequently, the measurements reflect this ECU-initiated power cut, which limited engine output before reaching the nominal point.

4.4 Energy Balance Evaluation

To fully characterize the thermodynamic efficiency of the internal combustion engine, a complete Energy Balance was computed across the testing matrix. The total chemical energy introduced by the injected fuel was partitioned into four primary pathways: Mechanical Power (brake power), Flue Gases Power (exhaust heat), Coolant Power (heat rejected to the water loop), and Unaccounted Losses (radiation, unmeasured chemical energy, and mechanical friction).

The experimental distribution of these energy fractions is illustrated in Figure 4.4.1.

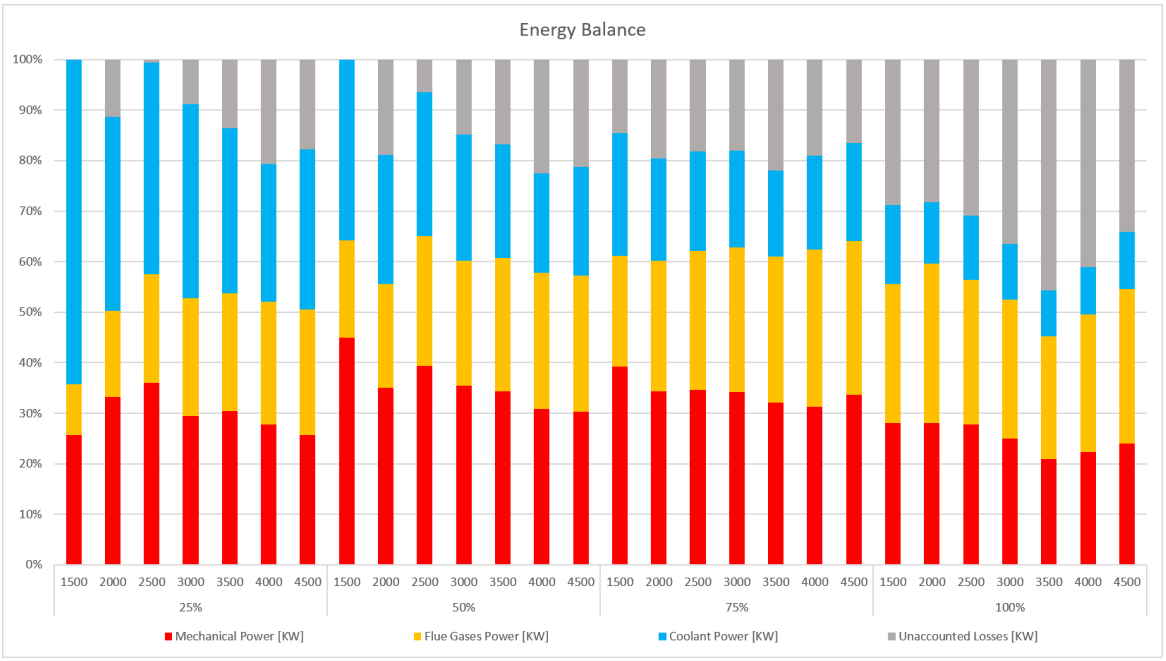


Figure 4.4.1-Experimental Engine Energy Balance across varying speeds and loads

An initial analysis of the Mechanical Power fraction (represented by the red bars) reveals a fundamental characteristic of the engine's operation: the highest Global Efficiency is consistently achieved between 50% and 75% load plateau, rather than at full load (100%). This empirical observation aligns perfectly with advanced internal combustion theory. At this load interval, the engine operates with relatively low pumping losses while still maintaining a stoichiometric air-fuel mixture ($\lambda \cong 1$), optimizing the conversion of fuel into mechanical work. While the energy distribution at lower loads (25% and 50%) generally aligns with expected theoretical behavior for a turbocharged engine, significant deviations appear at higher loads (100%), particularly at elevated engine speeds. In these severe operational regimes, the "Unaccounted Losses" fraction (represented by the grey bars) expands disproportionately, exceeding 30% of the total energy balance, while the Coolant Power appears artificially constrained. Far from being a random experimental error, this discrepancy provides deep insight into the physical limits of the test bench setup and the engine's transient thermodynamic behavior. The anomalous distribution at high loads can be attributed to three distinct converging factors:

- ECU Thermal Protection Strategies and 100% Load Efficiency Drop: The drop in relative mechanical efficiency at 100% load is a direct consequence of the ECU's protective mapping. To safely deliver maximum torque and manage the soaring temperatures previously discussed, the ECU abandons stoichiometry and actively

enriches the air-fuel mixture ($\lambda < 1$). The excess fuel is injected not to burn and produce power, but to evaporate and cool the combustion chamber. This excess unburnt fuel leaves the cylinder as latent chemical energy. Because the bench's exhaust energy calculations primarily rely on thermal enthalpy, this chemical energy escapes standard measurement, simultaneously deflating the apparent efficiency and heavily inflating the "Unaccounted Losses" at Wide Open Throttle.

- Thermal Inertia and Transient Testing Constraints: A fundamental limitation of the high-load testing was the inability to maintain the operational point long enough to reach true thermal equilibrium. Because the ECU would intervene if temperatures exceeded safety limits, Wide Open Throttle tests at elevated RPMs were strictly limited to short data acquisition windows (approximately 15 seconds). The physical mass of the engine block (cast iron and aluminum alloys [4]) possesses massive thermal inertia, acting as a thermal capacitor. During a short, violent step in heat generation, a significant portion of the thermal energy is temporarily absorbed into heating the metal mass of the block itself, rather than being immediately transferred to the coolant fluid. Because the engine does not have the minutes required to achieve steady-state heat rejection to the water jacket, the instantaneous energy balance fails to close accurately, further compounding the grey bar in the graph.
- Low-Load Fuel Measurement Uncertainty: Conversely, the energy balance at the 25% load and 1500 rpm introduces a distinct empirical challenge related to hardware sensitivity. At such minimal load request, the absolute mass flow rate of the injected fuel is exceptionally low. Consequently, the sensor's measurement error has a larger relative impact on these low readings. This small error slightly distorts the calculated balance between mechanical power and thermal losses at low loads.

Ultimately, the inaccurate energy-balance representation at extreme operating points illustrates the severe constraints of real-world engine testing. The graph effectively captures the exact moments where physical hardware limitations, electronic safety limits (ECU fuel enrichment), and thermodynamic realities (transient thermal inertia) combine to prevent a theoretical steady-state measurement.

4.5 Volumetric Efficiency Analysis

To comprehensively evaluate the breathing characteristics of the H5Ft engine, the volumetric efficiency was calculated using two different reference densities: the charge air density

upstream of the throttle body (pre-throttle) and the intake manifold air density (collector). Comparing these two metrics allows for the decoupling of the throttling pressure losses from the actual in-engine fluid dynamics.

It must be noted that the manifold air density was computed using the manifold absolute pressure (MAP) combined with the temperature recorded immediately downstream of the intercooler, prior to the throttle body. From a thermodynamic perspective, the expansion of the air across the partially closed butterfly valve is treated as an adiabatic isenthalpic throttling process. Because the enthalpy remains constant and no external work is performed, the static temperature drop across the valve is negligible. Therefore, using the pre-throttle temperature sensor provides a highly accurate and thermodynamically sound calculation of collector density.

Pre-Throttle Volumetric Efficiency: Figure 4.5.1 illustrates the volumetric efficiency calculated using the pre-throttle air density.

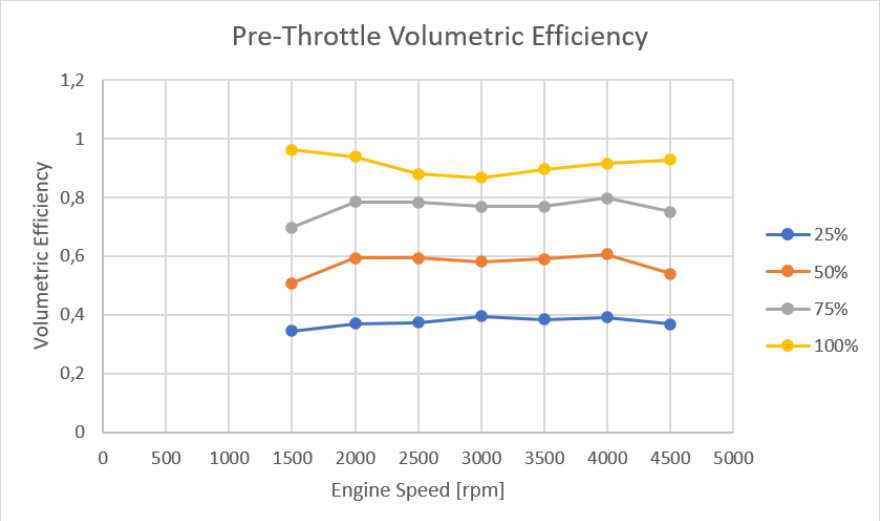


Figure 4.5.1-Pre-throttle Volumetric Efficiency

The most prominent feature of this graph is the severe stratification of the curves according to the engine load. At 25% and 50% loads, the apparent efficiency drops to roughly 40% and 60%, respectively. Because the reference density is taken upstream (where pressure is relatively high) but the actual mass flow is restricted by the throttle plate, this metric inherently captures the engine's pumping losses.

Beyond this general stratification, the curves at partial loads (25%, 50%, and 75%) remain remarkably stable across a wide mid-range band (2000–4000 RPM). Aside from minor fluctuations attributable to measurement noise, the efficiency remains constant in this region, decaying only at the extreme low and high engine speeds (1500 and 4500 RPM). This behavior reflects the natural acoustic tuning of the intake manifold geometry and the fluid's

kinetic limits. At low speeds (1500 RPM), the air moves too slowly to help fill the cylinder properly. Conversely, at high speeds (4500 RPM), the absolute time window for valve opening becomes exceedingly short; pulling air through the restricted throttle body in milliseconds heavily chokes the flow.

Observing the volumetric efficiency at 100% load, the curve exhibits an "inverted" profile compared to partial loads. This specific behavior can be fundamentally tied to the turbocharger's operational dynamics and the varying pressure differentials across the engine.

At the lower end of the speed range (1500 and 2000 RPM), the efficiency peaks near 1.0. In this region, the engine operates with a positive pumping differential. This theoretical condition is directly supported by the experimental test recordings, which explicitly show that the exhaust manifold pressure remains lower than the intake boost pressure at these specific speed points. Thanks to the immense thermal energy (enthalpy) of the exhaust gases, the turbine can generate significant intake boost without inducing excessive backpressure. This empirically observed favorable pressure gradient during the valve overlap period promotes a strong scavenging effect. Fresh pressurized air "washes" the residual gases out of the cylinder, with a fraction flowing directly into the exhaust tract. This dynamic artificially inflates the measured intake air mass at the flowmeter, driving the calculated efficiency upward.

As the engine reaches higher speed, the turbocharger compressor delivers maximum boost, causing the pre-throttle air density to rise. However, driving the turbine to sustain this maximum flow generates a localized peak in exhaust backpressure, which now exceeds the intake pressure. This high backpressure acts as a severe fluid dynamic bottleneck, counteracting the scavenging effect and trapping residual gases. The mathematical consequence of a surging reference density (denominator) coupled with a bottlenecked actual mass flow (numerator) is highly likely to cause the localized drop observed in the calculated efficiency.

As engine speed increases further (4000–4500 RPM), the ECU begins to regulate intake boost by opening the wastegate. However, experimental data from the exhaust manifold pressure sensor show that exhaust backpressure remains extremely high in this region (exceeding 3 bar) because the massive exhaust mass flow rate is forced through the turbine housing. Despite this severe negative pressure differential ($P_{exh} > P_{intake}$), the volumetric efficiency recovers at the upper end of the operational map, probably due to two primary factors: VVT management and fluid inertia. At high engine speeds, the ECU prevents simultaneous valve opening so that the high exhaust backpressure is isolated and cannot blow back into the intake tract. Concurrently, the extremely high velocity of the incoming fresh

air column creates a strong inertial "ram effect". This kinetic energy forcefully packs the cylinder during the intake stroke, overriding the static pumping restrictions and driving the volumetric efficiency upward.

Consequently, the mid-range represents the natural sweet spot where acoustic waves synchronize with valve timings and pressure differential to optimize filling despite the throttle restriction.

Manifold Volumetric Efficiency: To isolate the breathing capacity of the cylinders and valves from the throttle's restriction, the efficiency was recalculated using the manifold density, as shown in Figure 4.5.2.

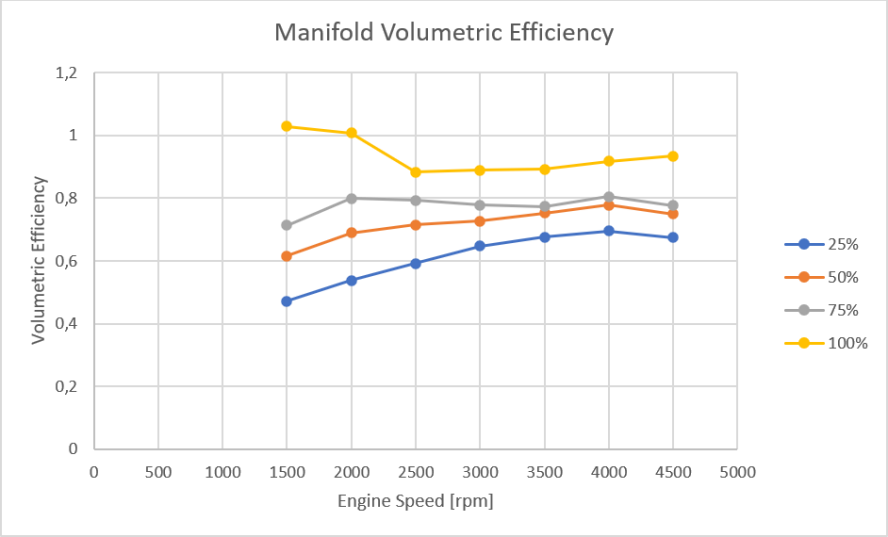


Figure 4.5.2-Manifold Volumetric Efficiency

Theoretically, calculating the efficiency based on collector conditions mathematically neutralizes the throttle's restriction, meaning the curves should overlap. However, the graph still exhibits a clear load dependency. This behavior highlights the complex in-cylinder fluid dynamics governed by the Variable Valve Timing (VVT) system:

- Low-Load Internal EGR and Speed Dependency (25% Load): At lower loads, the nearly closed throttle creates a significant vacuum in the intake manifold, while exhaust backpressure remains comparatively high. During the valve overlap period, the ECU intentionally adjusts the VVT to increase this overlap. The pressure differential causes hot exhaust gases to flow back into the cylinder (or intake port). This "internal EGR" strategy reduces pumping work and lowers combustion temperatures [17]. However, because these residual exhaust gases partially occupy the cylinder volume, the fresh air mass measured by the flowmeter decreases, resulting in mathematically lower volumetric efficiencies. Crucially, as observed in the 25% load curve, this effect is highly dependent on engine speed. At low speeds (1500–2000 RPM), the

absolute time duration (in milliseconds) of the valve overlap period is significantly longer. This extended temporal window allows a maximum mass of exhaust gas to backflow into the cylinder. As engine speed increases, the physical time available for this backflow decreases; less exhaust gas is trapped, and more fresh air can be drawn in, which explains the steady upward slope of the efficiency curve from 0.45 at 1500 RPM to roughly 0.70 at 4000 RPM.

- Mid-to-High Partial Loads (50% and 75% Load): When observing the 50% and 75% load curves, it is evident that they exhibit a very similar, relatively flat profile and are grouped closer together. Because this specific metric utilizes the collector density (downstream of the throttle), the aerodynamic pumping losses caused by the partially closed butterfly valve are mathematically neutralized. At these higher partial loads, the intake manifold vacuum is less severe compared to the 25% condition, which inherently reduces the aggressive internal EGR backflow. Consequently, without the throttling restriction skewing the mathematical calculation, these converging curves accurately reflect the engine's "true" geometric and acoustic breathing capacity, demonstrating consistent in-cylinder fluid dynamics across the mid-to-high load range.
- At 100% load, the aerodynamic restriction of the butterfly valve is virtually eliminated. Consequently, the pressure drop across the throttle body approaches zero, making collector and pre-throttle volumetric efficiency directly comparable. Under these conditions, the two metrics effectively converge, sharing a nearly identical operational profile across the engine speed range. Analyzing this full-load profile, a distinct peak occurs at low engine speeds (1500–2000 RPM). In the collector efficiency evaluation (Figure 4.5.2), the value slightly exceeds the theoretical geometric limit. While the engine does operate with a favorable positive pumping differential in this region, aiding cylinder filling and pushing the true efficiency very close to 1.0, as confirmed by the pre-throttle graph, the specific overshoot above 1.0 in the collector calculation is highly likely an artifact of measurement uncertainty. The intake mass flow meter's inherent compounding tolerances, combined with slight calibration offsets between the MAP and pre-throttle sensors, can easily account for this deviation, so it is more accurately attributed to instrumental tolerance than to a massive scavenging effect.

  Moving into the mid-range (2500–3500 RPM), both efficiency curves exhibit a synchronized depression. Because the throttle is fully open, this localized dip is

universally driven by the turbocharger's exhaust backpressure. As previously established, generating maximum boost at peak torque requires substantial exhaust enthalpy, creating a high-pressure bottleneck in the exhaust manifold. This backpressure temporarily restricts the actual fresh air mass flow, causing the efficiency to dip. Finally, as the engine speed approaches 4000–4500 RPM, the wastegate opens to regulate boost, alleviating the exhaust restriction and allowing both efficiency metrics to recover simultaneously.

4.6 Brake Specific Fuel Consumption (BSFC) and Global Efficiency Analysis

To further evaluate the engine's operational efficiency and validate the findings from the energy balance, an analysis of the Brake Specific Fuel Consumption (BSFC) and the Global Thermal Efficiency was conducted. BSFC represents the mass of fuel consumed per unit of mechanical energy produced [g/kWh], while global efficiency evaluates the percentage of the fuel's chemical energy converted into useful work. Together, they are critical metrics for identifying the engine's optimal operating window. The complete BSFC mapping across the tested speed and load matrix is illustrated in Figure 4.6.1, and the corresponding twin map for global efficiency is presented in Figure 4.6.2.

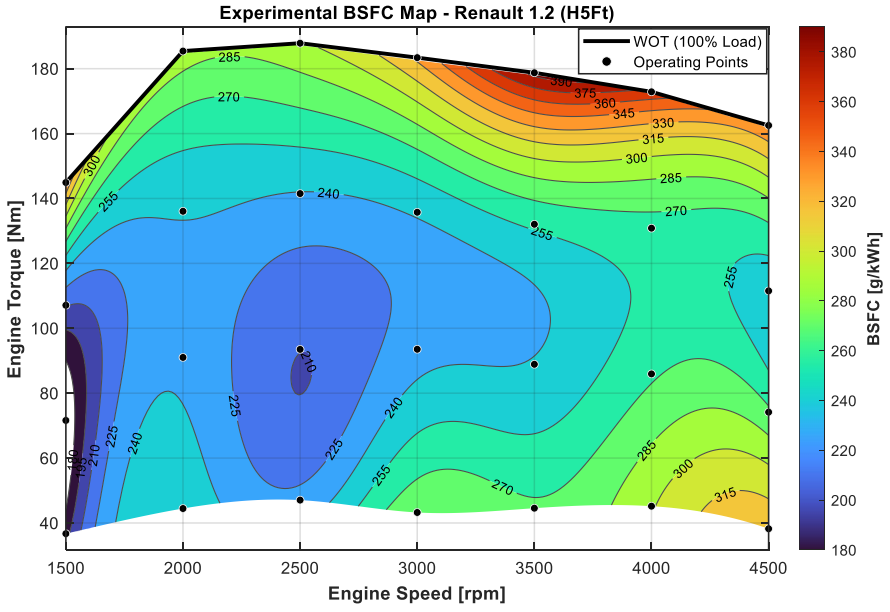


Figure 4.6.1-Experimental BSFC Map correlating Specific Fuel Consumption with Engine Speed and Torque

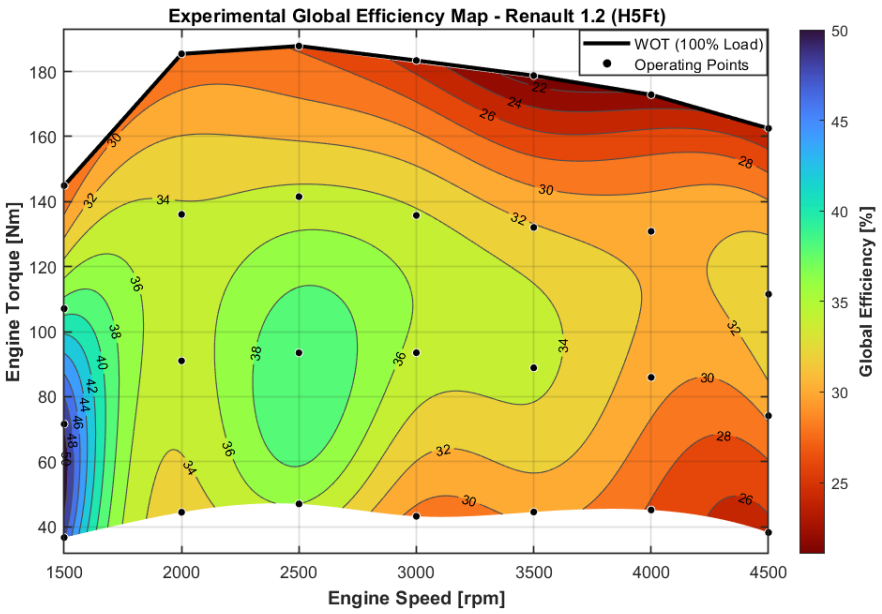


Figure 4.6.2-Experimental Global Efficiency Map correlating Engine Efficiency with Engine Speed and Torque

Low-Load Measurement Artifacts: As previously discussed in the energy balance analysis, the exceptionally low BSFC values recorded at the bottom-left of the map (low loads and low engine speeds, notably around 1500 RPM) must be interpreted as measurement artifacts rather than actual physical phenomena. In this operating regime, the fuel mass flow rate is extremely low. Consequently, the test bench's fuel consumption sensor operates near its lower detection threshold, slightly underestimating the injected fuel. This instrumental limitation artificially depresses specific consumption calculations and, conversely, artificially inflates the computed global efficiency, failing to reflect the thermodynamic reality of heavily throttled operation, where pumping losses are expected to dominate.

Optimal Operating Range: Once these low-load anomalies are accounted for, the optimal operating window emerges across the intermediate-to-high load region, spanning from 50% to 75% load. While the absolute minimum BSFC is recorded between 50% and 65% load, the entire 50-75% band maintains relatively high global efficiency over a wide range of speeds, staying consistently above 34% up to approximately 3500 RPM. This plateau, in particular, represents an ideal thermodynamic balance: the throttle plate is open enough to minimize parasitic pumping losses, yet the overall thermal load remains below the threshold that would require ECU fuel enrichment. As a result, the engine sustains stoichiometric combustion, maximizing fuel conversion efficiency while delivering substantial mechanical power.

Full-Load Inefficiency and ECU Enrichment Strategies: Conversely, the maps explicitly demonstrate that the lowest thermodynamic performance occurs at 100% load across the entire engine speed range. In this regime, BSFC peaks at nearly 395 g/kWh, driving global efficiency below 22% around 3500 RPM. At Wide Open Throttle, intake charge temperatures rise sharply. To prevent destructive engine knocking and to manage exhaust gas temperatures, the ECU proactively alters combustion parameters. The primary defense mechanism is heavily enriching the mixture ($\lambda < 1$). This excess fuel is injected to exploit its latent heat of vaporization, cooling the combustion chamber; however, because it does not fully combust, it fails to generate proportional mechanical torque. Furthermore, the ECU often retards the ignition timing to suppress detonation, which inherently reduces the effective mechanical work extracted per cycle. Despite this overall degradation at full load, it is noteworthy that along the 100% load boundary, the BSFC drops to a relative minimum and global efficiency simultaneously reaches a localized peak between 2000 and 2500 RPM. This improvement coincides with the engine's maximum torque delivery, representing an optimal combustion window where mechanical energy extraction is maximized before thermal limits force harsher ECU restrictions at higher speeds.

5 Conclusion

This thesis presented the comprehensive development, automation, and validation of an engine dynamometer test bench, followed by a detailed experimental characterization of the 1.2 Renault H5Ft powertrain. The foundational work encompassed the complete hardware and software integration of the test cell, including the physical installation and meticulous calibration of the Data Acquisition Systems and the sensor network required for precise experimental measurement. Built on this solid physical setup, a dual-loop control system governing engine speed and charge was implemented and tuned, transforming the raw hardware into a highly reliable testing platform capable of capturing complex fluid dynamic and thermodynamic phenomena.

5.1 Summary of Key Findings

The experimental campaign validated both the successful commissioning of the test bench and the operational characteristics of the engine:

- Hardware Commissioning and Control Stability: Following the initial hardware implementation and calibration, the implemented Proportional-Integral-Derivative (PID) control loops demonstrated excellent setpoint tracking and disturbance rejection. The primary engine speed controller successfully managed mechanical inertia and torque transients, while the charge controller's RPM-dependent gain scheduling effectively navigated the engine's non-linear torque response, preventing runaway oscillations at low speeds and ensuring global stability across the map, although some residual transient jitter and settling delays still persist at specific low-speed boundaries.
- Energy Balance and Specific Fuel Consumption (BSFC): Utilizing the newly automated setup, the analysis identified the engine's highest global efficiency and optimal fuel consumption within the 50% to 75% load plateau. Conversely, the test bench accurately captured the powertrain's physical limits at 100% load, where extreme intake temperatures forced the ECU into proactive fuel enrichment and power-cut strategies, severely penalizing the BSFC and generating significant unaccounted thermal losses. Furthermore, the assessment highlighted critical measurement artifacts at minimum loads and low engine speeds (e.g., 25% load at 1500 RPM); in this

regime, the fuel mass flow falls near the sensor's lower detection threshold, leading to an underestimation of the injected fuel and artificially depressed BSFC values.

- Volumetric Efficiency and Breathing Dynamics: The wide and precise sensor network enabled the decoupling of aerodynamic throttling restrictions from true in-cylinder dynamics. The experimental data empirically validated the presence of internal Exhaust Gas Recirculation (EGR) driven by Variable Valve Timing (VVT) at partial loads, while highlighting the complex fluid dynamic interplay between turbocharger backpressure, fluid inertia, and wastegate regulation at full load.

5.2 Future Work and Test Bench Upgrades

With the baseline physical architecture and macro-parameter mapping fully established, the test bench is now primed for indicated cycle diagnostics, predictive modeling, and system optimization. The planned future upgrades include:

- Cooling System Enhancement: The experimental campaign highlighted severe thermal bottlenecks at high rotational speeds, where post-compressor air temperatures approached safety thresholds, triggering proactive ECU power cuts. Upgrading the current test cell infrastructure with a high-capacity air-to-water intercooler will mitigate these thermal constraints, preventing engine knock (detonation) and allowing for sustained, steady-state data acquisition at Wide Open Throttle up to the engine's nominal peak power.
- Charge Control Algorithm Optimization: While the RPM-dependent gain scheduling strategy successfully stabilized the system, there remains a margin for refining the secondary PID charge controller. Future software calibrations should focus on further damping the transient micro-oscillations (jitter) observed at specific low-speed/low-load boundaries, while simultaneously minimizing the overall settling time to reach the commanded torque target, thereby enhancing the system's dynamic responsiveness.
- Engine Virtualization (1D Modeling): The extensive steady-state and transient datasets acquired during this experimental campaign will serve as the empirical foundation to calibrate and validate a 1D virtual engine model (e.g., utilizing AVL simulation software). This digital twin will allow researchers to virtually predict engine behavior and optimize calibrations, drastically reducing physical testing time and thermal stress on the hardware.

- In-Cylinder Combustion Analysis: To transition the bench from macroscopic dynamometer mapping to highly detailed indicated cycle analysis, the mechanical setup will be upgraded with a high-resolution crankshaft encoder and an in-cylinder pressure sensor. This instrumentation will enable the precise calculation of the Indicated Mean Effective Pressure (IMEP) and the direct evaluation of pumping work.
- Emission Analysis Implementation: The integration of continuous exhaust gas analyzers into the test cell will complete the powertrain characterization, providing valuable insight into the engine's environmental impact across the entire operational envelope.

6 References

[1] IEA, "Greenhouse Gas Emissions from Energy Data Explorer," [Online]. Available: https://www.iea.org/data-and-statistics/data-tools/greenhouse-gas-emissions-from-energy-data-explorer.

[2] IEA, [Online]. Available: https://www.iea.org/energy-system/transport.

[3] European Union, "Vehicle emissions and battery durability (Euro 7): technical requirements and certification rules," [Online]. Available: https://eur-lex.europa.eu/EN/legal-content/summary/vehicle-emissions-and-battery-durability-euro-7-technical-requirements-and-certification-rules.html.

[4] RENAULT POWERTRAIN, "H5Ft TCE 115,TCE 120,TCE 130 1.2 Turbo GDI - Gasoline Euro 5," [Online]. Available: https://it.scribd.com/document/437486931/Brochure-1200-Turbo-GDI-V1-MAJ-2014.

[5] R. E. Bavarin, "50 kW Eddy Current brake," 2006.

[6] A. N. García, "DISEÑO DEL SISTEMA DE CONTROL DE UN MOTOR DE COMBUSTIÓN," Madrid, 2025.

[7] D. Palumbo. [Online]. Available: https://blog.wika.com/it/knowhow/i-tipi-di-termocoppie-e-le-loro-differenze/.

[8] FAE, "MANIFOLD ABSOLUTE PRESSURE SENSORS (MAP)," [Online]. Available: https://it.scribd.com/document/407353550/familia-15-47-pdf.

[9] TC-Direct, [Online]. Available: https://www.tcdirect.co.uk/product-2-355-2/Industrial-Pressure-and-Vacuum-Transmitters.

[10] Fine Controls LTD, [Online]. Available: https://www.finecontrols.co.uk/files/pdf-manuals/burkert-pdfs/8071m.

[11] Autosen, "AS010 Caudalímetro," [Online]. Available: https://autosen.com/es/Sensores-de-proceso/Sensores-de-flujo-y-caudalimetros/Caudalimetros-Vortex/Caudalimetro-Vortex-G1-1-4A-AS010.

[12] Farnell, [Online]. Available: https://www.farnell.com/datasheets/3611388.pdf.

[13] B. G. Liptak, "INSTRUMENT ENGINEERS' HANDBOOK - Process Measurement and Analysis VOLUME I," [Online]. Available: https://skoge.folk.ntnu.no/puublications_others/books/Liptak-2003-Instrument%20Engineers%20Handbook,%20Volume%201%20Process%20Measurement%20and%20Analysis,%20Fourth%20Edition.pdf.

[14] Robert Bosch GmbH, "Hot-film air-mass meter, Type HFM 5," [Online]. Available: https://members.rennlist.com/jandreas/Bosch%20HFM5%20Sensors.pdf.

[15] Middle East Technical University (METU), "Hot-Wire Anemometry," [Online]. Available: https://ocw.metu.edu.tr/pluginfile.php/1871/mod_resource/content/0/AE547/AE547_9_Hotwire-son.pdf.

[16] J. B. Heywood, Internal Combustion Engine Fundamentals, McGraw-Hill Education.

[17] M. S. B. Eihab A. Raouf, "Analyzing the S.I. Engine's Changeable Exhaust Valve Timing and Exhaust Gas," *International Journal of Heat and Technology,* vol. 43, no. 1, 2025.